UNIVERSITY OF CALGARY

Multicomponent seismic applications in coalbed methane development, Red Deer, Alberta

by

Sarah Elizabeth Richardson

A THESIS
SUBMITTED TO THE FACULTY OF GRADUATE STUDIES
IN PARTIAL FULFILLMENT OF THE REQUIREMENTS FOR
THE DEGREE OF MASTER OF SCIENCE

DEPARTMENT OF GEOLOGY AND GEOPHYSICS

CALGARY, ALBERTA

NOVEMBER, 2003

UNIVERSITY OF CALGARY

FACULTY OF GRADUATE STUDIES

The undersigned certify that they have read, and recommend to the Faculty of Graduate Studies for acceptance, a thesis entitled "Multicomponent seismic applications in coalbed methane development, Red Deer, Alberta" submitted by Sarah Elizabeth Richardson in partial fulfillment of the requirements for the degree of Master of Science.

Supervisor, Dr. Don C. Lawton, Dept. of Geology and Geophysics

Dr. Gary F. Margrave, Dept. of Geology and Geophysics

Dr. Cindy Riediger, Dept. of Geology and Geophysics

Dr. Robert R. Stewart, Dept. of Geology and Geophysics

Dr. S.A. (Raj) Mehta, Dept. of Chemical and Petroleum Engineering

Date:______________________________

ABSTRACT

Vertical seismic profiles obtained of Ardley coal zone strata near Red Deer, Alberta demonstrate the effectiveness of multicomponent seismic applications in coalbed methane development. Zero-offset surveys show that a broad-band mini-P vibratory source is ideal for imaging the coal zone, providing a measure of vertical continuity of the coal zone as well as delineating intra-coal events. The extraction of Vp/Vs from P-wave and S-wave seismic data yields a high Vp/Vs value in the near surface (~5), decreasing to approximately 2.5 at 300 m depth. Reflectivity values extracted from walkaway surveys demonstrate that converted-wave data better resolve the upper coal contact than compressional-wave data, as they are less affected by tuning. Numerical modelling demonstrates "proof of concept" that time-lapse seismic imaging will be able to monitor changes in the reservoir resulting from dewatering, allowing producers to optimize enhanced coalbed methane production throughout reservoir life.

ACKNOWLEDGEMENTS

I would like to thank Dr. Don Lawton, my supervisor, for his support and guidance, and for continually challenging me to improve my work. His patience and understanding inspired me to keep working despite all the difficulties of the past two and a half years.

I also give thanks to the following people who have provided help in various ways over the course of my studies:

- Dr. Gary Margrave, Dr. Rob Stewart, and Dr. Larry Lines for valuable discussions on VSPs, Vp/Vs, and seismic processing;
- Mr. Henry Bland, Mr. Kevin Hall, Mr. Eric Gallant, and Mr. Malcolm Bertram for computer hardware and software support, and for assistance with fieldwork;
- Dr. Chuck Ursenbach for his assistance with the CREWES Zoeppritz reflectivity explorer;
- Ms. Louise Forgues for attending to all manner of administrative issues;
- Dr. Helen Isaac for helping me deal with the multitude of quirks and problems arising from ProMAX;
- Mr. Richard Bale for his assistance and advice in data processing;
- Mr. Andrew Beaton, from the Alberta Research Council, for valuable conversations regarding coal geology, and for helping me obtain coal samples for physical testing;
- Mr. Mike Jones, and Ms. Larissa Bezouchko of Schlumberger Canada, for allowing me to be involved in their processing of the seismic data;

- Suncor, Inc. and the Alberta Research Council, for providing access to the field site and well data;
- Mr. Bob Runnalls of Imperial Oil Resources, for allowing me to continue working on such a flexible schedule during my studies;
- Mr. Rory Moir and Mr. Terry Buchanan, also of Imperial Oil Resources, for being outstanding mentors and teaching me more about well log interpretation than I ever thought possible;
- The CREWES "lunch bunch" regulars– Richard Bale, Brian Russell, Jon Downton, Andrew Royle, Ian Watson, and Larry Lines, for fascinating conversations about geophysics and countless other topics;
- All my friends, particularly Carrie Armeneau, Joanne Archer, Lisa McCluskey, Helen Degeling, Sarah Travis, and Kimberley Motz for their support and laughter;
- Ms. Rachel Newrick, for geophysical discussions, constant support, smiles, and for being my personal angel on two wheels – I will never ride faster than she can fly;
- My parents, for their continued support and for inspiring me to strive for excellence in everything;
- My husband, Clifford Trend, for his unending patience, encouragement, love, support, and faith in my abilities.

Financial support from the Alberta Ingenuity Fund, the Society of Exploration Geophysicists, the Province of Alberta, the Canadian Society for Coal and Organic Petrology, the Alberta Energy Research Institute, the Natural Sciences and Engineering Research Council, and the CREWES Project at the University of Calgary is also gratefully acknowledged.

DEDICATION

for Clifford

TABLE OF CONTENTS

LIST OF TABLES

LIST OF FIGURES

GLOSSARY

1.5-dimension	modelling that allows for velocity variation in the vertical direction only, involving a 1-D model and source-receiver offsets (Sheriff, 2002)
cleats	two sets of naturally occurring fractures perpendicular to each other within a coal seam, typically on a cm scale (Fay, 1920)
CBM	coalbed methane, natural gas produced from underground coal seams
cyclothem	a series of beds deposited during a sedimentary cycle of the type that prevailed during the Pennsylvanian Period; nonmarine sediments, often including bituminous coal, commonly occur in the lower half of a cyclothem, marine sediments in the upper half (Bates & Jackson, 1984)
desorption pressure	pressure at which methane adsorbed in coal matrix is able to form a free gas phase within the coal reservoir
dewatering	production of water from coal zone, often necessary prior to methane production
ECBM	enhanced coalbed methane – methane production aided by the injection of another gas, typically nitrogen or carbon dioxide
geological sequestration	long-term storage of greenhouse gases in underground reservoirs, such as depleted oil and gas reservoirs, or coal zones
harmonic	a frequency that is a simple multiple of a fundamental frequency (Sheriff, 2002)
limit of detection	the minimum thickness for a bed to give a reflection that stands out above the background (Sheriff, 2002)
limit of resolution	for discrete seismic reflectors, the minimum separation so that one can determine that more than one interface is involved (Sheriff, 2002)

SEG standard polarity	a positive amplitude (peak) on a P-P section indicates a P-wave impedance increase, whereas a positive amplitude on a P-S section indicates an increase in S-wave impedance (Thigpen et al., 1975)
time-lapse seismic imaging	repeating a seismic survey to determine the changes that have occurred in the interval, such as may be caused by hydrocarbon production (Sheriff, 2002)
walkaway VSP	a vertical seismic profile performed by moving source points to progressively larger offsets while keeping geophones fixed (Sheriff, 2002)
VSP	vertical seismic profile; measurements of the response of a geophone at various depths in a borehole to sources on the surface (Sheriff, 2002)

Chapter 1 Introduction

1.1 Coalbed Methane in Alberta

Coalbed methane (CBM) is an almost pure form of natural gas found in subsurface coals. It has the potential to contribute significantly to Canada's future energy supply (CAPP, 2003), but is still in the early stages of development in Alberta. CBM production is found worldwide, including large developments in the USA, where it accounted for 7% of the nation's daily production in 2000 (Avery, 2001), and has grown to provide nearly 20% of daily natural gas production in 2002 (van der Meer, 2002). American coalbed gas-in-place resources are estimated at nearly 750 trillion cubic feet (TCF), of which approximately 95 TCF is estimated to be recoverable (Gas Technology Institute, 2001).

Alberta is the most promising CBM development site in Canada, with an estimated 412 TCF in place (Gas Technology Institute, 2001). The first commercial production of CBM in Alberta was announced in February 2002 (Avery, 2002), although currently fewer than 100 CBM wells in Alberta are producing, split between two commercial projects (CAPP, 2003). Canadian coalbed methane is an emerging energy source with many technical challenges to overcome before large-scale production is realized, although with only 43 TCF of established remaining reserves of conventional natural gas within the province of Alberta (Alberta Energy and Utilities Board, 2002), the drive to develop this untapped resource is high.

1.2 Coalbed methane reservoir geology

Unlike conventional reservoirs, most coalbed gases are not stored in the macroporosity of a coal seam, but are contained sorbed onto the surface of micropores, considered part of the matrix (Figure 1.1). The average microporosity of coal is less than 1% by volume (Langenberg, 1990). Micropore storage is much more efficient than conventional reservoir macropore storage, and a coal seam may hold up to twenty times the volume of gas found in a conventional reservoir of similar size, temperature, and pressure (Rice, 1993). The exact quantity of sorbed gas is controlled by the confining pressure and surface area of the micropore system.

The macroporosity of coal seams is the cleat system – two sets of naturally occurring fractures perpendicular to each other within a coal seam, typically on a cm scale (Fay, 1920). Cleats develop as a result of shrinkage during devolatization, normal to the plane of bedding within coal strata (Dawson et al., 2000). Face cleats are more continuous, and control the flow of gas to a wellbore, whereas butt cleats are less continuous cleats that are associated with the diffusion of gas from the coal to the face cleats (Figure 1.1). Larger-scale post-depositional fractures may also exist within a coal seam, and are controlled by local tectonic processes. Permeability is controlled primarily by the cleat system, however, and is generally low, less than 10 mD (Langenberg, 1990). Small quantities of methane may be stored as free gas or dissolved in water found in cleats.

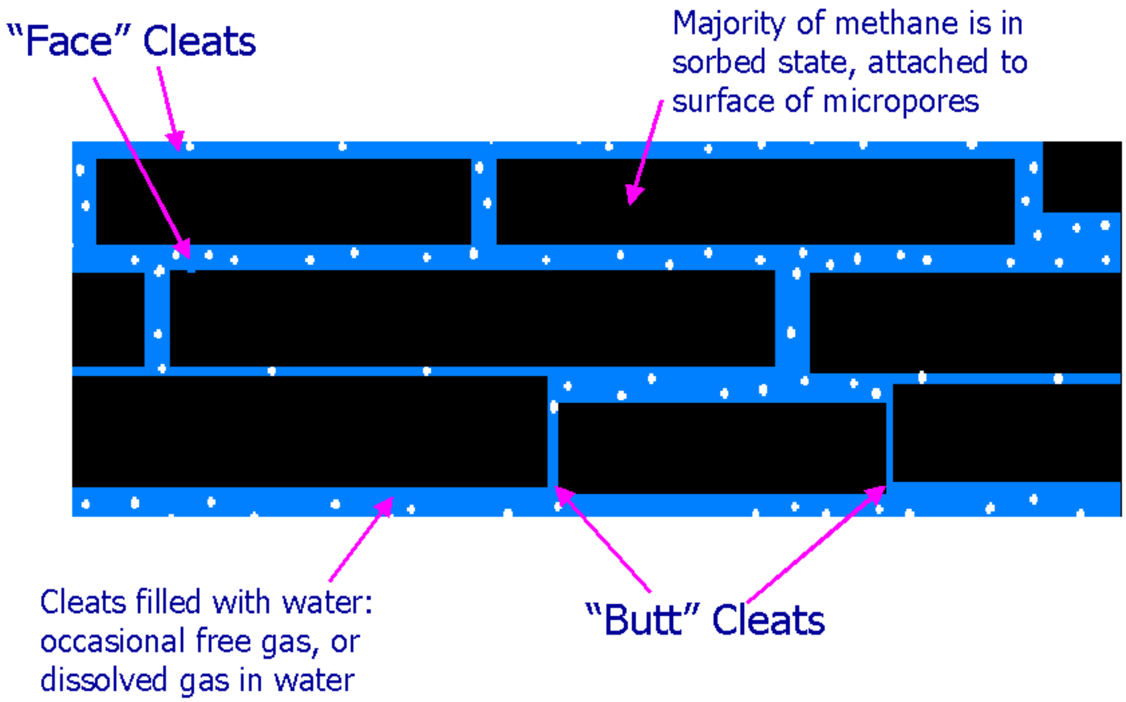

Figure 1.1 Plan view (looking down on bedding plane) of typical coal reservoir showing cleats. Methane is in a sorbed state, attached to the surface of micropores within the coal, and may also be present dissolved in the water filling the cleat system.

1.2.1 Geological factors affecting CBM development

The degree of cleating within a coal seam is the single most important geological factor affecting CBM development, as hydraulic communication is necessary throughout the reservoir for successful production (Saulsberry et al., 1996). Several other geological criteria must also be met, however. Coal rank must be sufficiently high for thermogenic gas generation, that is, at least sub-bituminous, with higher rank coals producing greater quantities of methane (Dawson et al., 2000). Moderately high rank coals (sub-bituminous to low-volatile bituminous) have a higher cleat density than high-ranking anthracites, rendering them the most desirable coals for production (Dawson et al., 2000).

Poor quality coals with high ash or shale content have reduced internal surface area, thus reducing gas storage capacity. Composition affects not only quality, but also permeability, with vitrinite-rich coal being more heavily cleated than dull coal such as inertinite (Dawson et al., 2000).

Individual coal seams less than 1 m thick are considered too thin to yield economic rates of gas, unless they are within a coal zone greater than 1.5 m thick (Dawson et al., 2000). Seams must be at depths greater than 200 m to reach sufficient pressure for methane production, but less than 2000 m to reduce the risk of overburden pressure sealing off fracture systems (Rice, 1993).

1.3 Coalbed methane production

For coal seam methane to desorb and flow, pressure exerted by cleat water must be reduced to equal that exerted by adsorbed gas. This "desorption pressure" represents the point at which a free gas phase may exist within the reservoir. Water is produced ("dewatering") and pressure lowered until gas desorbs from the matrix into the adjacent cleat system (Metcalfe et al., 1991).

Relative permeability curves for coals in the Warrior Basin, Alabama, show the dramatic increase in the relative permeability of gas with a reduction in water saturation (Figure 1.2). As water saturation decreases, more volume is available within the cleat system for gas to travel, increasing the relative permeability of gas. Gas fills this portion of the cleats, water saturation decreases, and relative permeability for water continues to decrease until a state of 100% permeability to gas is reached and the coal is finished dewatering.

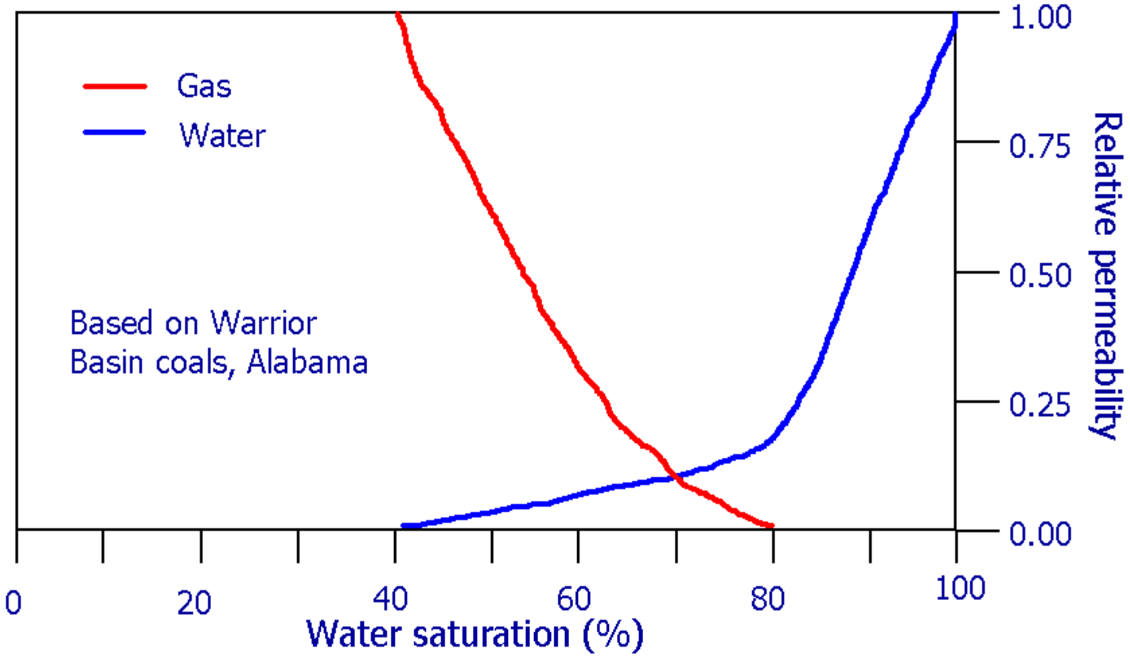

Figure 1.2 Graph of relative permeability of gas and water vs. water saturation within coal seams of the Warrior Basin, Alabama. As water saturation decreases, gas production improves as the relative permeability to gas improves substantially (Nikols et al., 1990).

Two key issues present themselves in CBM production. Often, dewatering a coal seam reduces reservoir pressure to such a degree that economic flow rates of methane are not possible. Operators must also face the issue of long dewatering periods during which little or no methane is produced, increasing pay-out time for initial investment (Hitchon et al., 1999). Enhanced coalbed methane production offers a solution to both issues.

1.3.1 Enhanced coalbed methane production (ECBM)

The total quantity of gas that may be adsorbed by any coal seam is dependent not only on system pressure, but also on the composition and microporosity of the coal. For pure gases at the same pressure and temperature, the ratio of adsorption for carbon dioxide, methane, and nitrogen is

4:2:1 (Bachu, 2000). Injection of a lower adsorbing gas, such as nitrogen, reduces the partial pressure of methane while maintaining reservoir pressure, allowing methane to flow (Seidle et al., 1997). Injection of higher-adsorbing gas such as carbon dioxide results in the preferential adsorption of CO_2, and physical displacement of methane out of the reservoir into the cleat system (Bachu, 2000).

Comparative production using Warrior Basin coals and various injection gases demonstrates that cumulative methane production with injection is more than double that without injection (Figure 1.3), with a greater quantity of methane produced much earlier in the field's life (Gunter et al., 1997). When water is present, it is co-produced; its production is also enhanced.

As methane is released from a coal reservoir, the matrix shrinks, improving permeability by causing cleats to open. As another gas (such as CO_2) is adsorbed onto the coal, however, the coal matrix swells, causing cleats to close (Fokker & van der Meer, 2002). As such, it is essential to find a balance between gas production and injection to maintain optimum permeability.

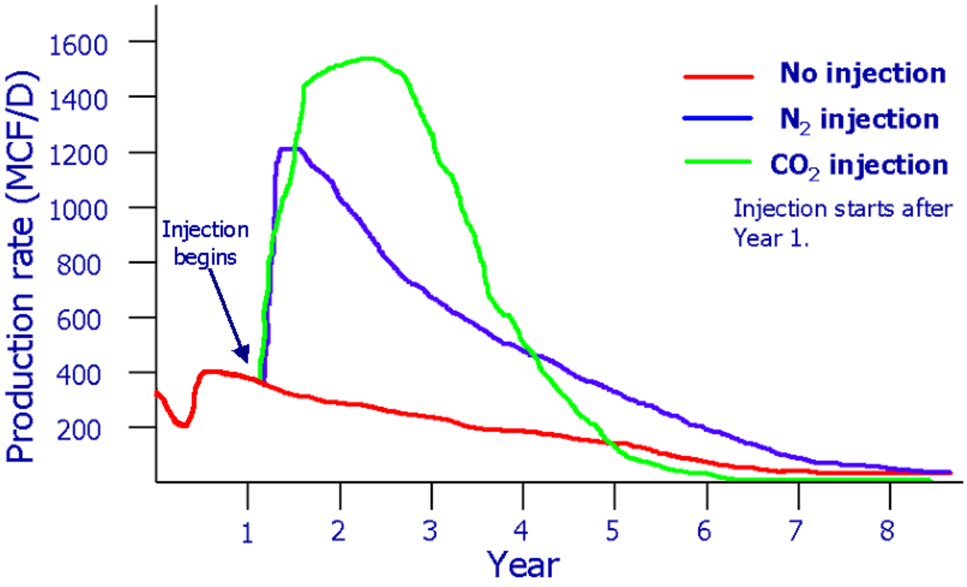

Figure 1.3 Graph illustrating difference in methane production rate with gas injection. The red line represents production with no injection whatsoever, whereas the blue line represents injection of N_2, and the green line represents the injection of carbon dioxide. Assumptions are injection pressure of 2000 psi, reservoir pressure of 1500 psi, permeability of 10 mD, porosity of 0.5%, thickness of 10 feet and drainage area of 46 acres (slightly more than one Alberta LSD). Coal is assumed to be 100% gas-saturated. Injection and production wells are arranged in a five spot pattern (Gunter et al., 1997).

Injection of carbon dioxide into CBM reservoirs not only enhances production of methane, but also serves as an effective greenhouse gas sequestration technique, reducing emissions into the atmosphere (Wawerski & Rudnicki, 1998). Carbon dioxide emissions alone are known to account for approximately 50% of the increase of the greenhouse effect (van der Meer, 2002). Accompanied by methane production or not, any suggested CO_2 removal strategy will need to provide a system of quantifying the amount of CO_2 initially sequestered, and of monitoring the reservoir over time, ensuring no leakage back to the atmosphere (Chadwick et al., 2000).

1.4 Coal seismology

Coal has low seismic velocity and low density with respect to its bounding strata, thus, although coal seams are extremely thin with respect to seismic wavelength, their exceptionally large acoustic impedance contrast with surrounding rocks results in distinct reflections (Gochioco, 1991). Limits of resolution for coal beds are approximately $\lambda/8$, and their limit of detection is less than that for other strata, often approximately $\lambda/40$ (Gochioco, 1992).

1.4.1 Seismic studies of coalbed methane strata

Historically, coal seismology has been used as a tool in effective mine planning. Many of these techniques may be applied to coalbed methane exploration and development. Coal mining seismic surveys are key in determining coal structure and location, as well as the presence of faulting – which can be economically disastrous if encountered unexpectedly in a mining operation. Ziolkowski (1982) conducted a great deal of research into in-seam seismic methods with coal, demonstrating that in-situ methods are an ideal complementary technique for identifying faults and structures too small to be resolved from surface.

Coal seams are often very thin, resulting in the need for high-bandwidth data to properly image seams. A study by Knapp (1990) of the vertical resolution of cyclothems determined that frequencies greater than 500 Hz are needed to resolve individual cyclothem beds. Lower-frequency data may be phase filtered, however, such that each bed has a single wavelet associated with it, that is, peaks and troughs for alternating layers.

Fault identification has been a great advantage of seismic data in areas of coal production. Faults are not only of great importance in mine design, but may also interfere with coal bed methane production if the throw is greater than seam thickness (Gochioco & Cotton, 1989). Seismic data of the Carbondale Formation (within an unidentified U.S. mine) allows the identification of faults with displacement of the same magnitude as the seam thickness (Gochioco & Cotton, 1989). Surveys conducted near Harco, Illinois, allowed the identification of eight previously undetected faults, as well as the proper location of a sandstone-filled incision (Henson, Jr & Sexton, 1991). This study demonstrated the effectiveness of combined seismic and borehole data, as the incision had been incorrectly mapped using borehole data alone. A second study within the Illinois basin (Gochioco, 2000) demonstrates the increased effectiveness in using 3D seismic data compared to 2D seismic lines. Misinterpretations are more likely to occur when geologic anomalies are small relative to the spatial resolution of a 2D survey.

Seismic surveys of coalfields are not only useful for interpreting bed thickness or overall field geometry and structure. Seismic data may allow for identification of facies changes, which in turn may be used to determine depositional environments of coals (Lawton, 1985). Knowledge of the depositional setting is useful in predicting coal type and lateral continuity – both important factors in CBM prospecting. A case study of the Highvale-Whitewood coalfield in the plains of Alberta demonstrates that a seismic survey was useful in examining field structure, determining coal thickness, and identifying surrounding strata (Lyatsky & Lawton, 1988). The study also demonstrates that the character of coal reflections is not always related strictly to geological variations within the coal, but is dependent on the influence of the overlying and underlying sediments.

High-resolution reflection seismology has been effectively used to evaluate the Wyodak coal at a prospective CBM site, identifying structures and estimating their related fracture densities (Greaves, 1984). Lyons (2001) has demonstrated the effectiveness of seismic surveys in illustrating previously unknown structure and fracture trends in the Ferron coalbed methane field of the San Juan Basin.

Development of the Cedar Hill CBM field of the San Juan basin relied on the assumption of a homogeneous field. Multi-component 3D seismic data has since shown the field to be both compartmentalized, and heterogeneous (Shuck et al., 1996). Converted-wave data are useful for mapping structure and identification of overpressured zones. This Cedar Hill survey has also been examined in conjunction with amplitude-vs.-offset (AVO) analysis (Ramos & Davis, 1997). Areas with large AVO intercepts indicate low-velocity coals, possibly related to zones of stress relief. Large AVO gradients are indicative of large Poisson’s ratio contrasts, and therefore, are indicative of high fracture densities. The integration of multi-component 3D seismic and AVO analysis is a useful approach to characterizing fractured reservoirs.

Numerical modelling conducted on a model of thin coalbed strata found at Willow Creek, Alberta (Richardson et al., 2001) tested the viability of imaging thin (<1.5 m) coal seams using reflection seismology (Figure 1.4). This coal zone was shown to be mappable using seismic reflection techniques, although it is unlikely that individual thin seams may be resolved using bandwidths typically attained in field seismic data.

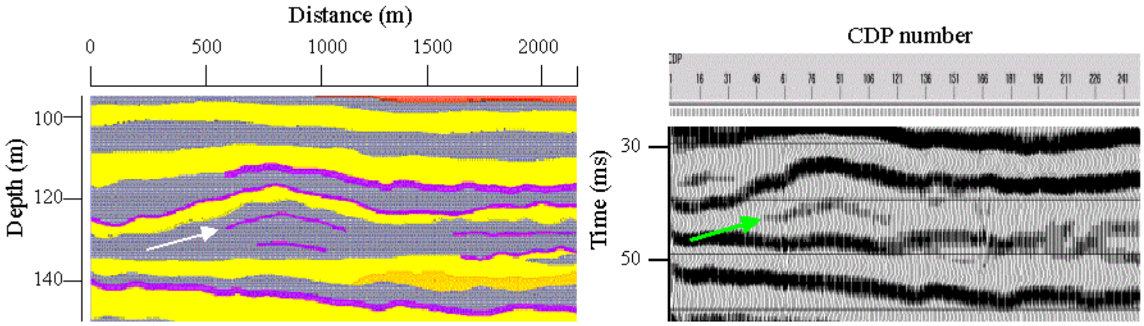

Figure 1.4 Portion of Willow Creek numerical model and its seismic response. In the model on the left, thin purple beds represent coal seams; yellow and grey represent sandstone and shale, respectively. Seismic modelling used normal-incidence ray-tracing and convolution with a 100 Hz Ricker wavelet. The small discontinuous coal seam (less than 1.5 m thick) highlighted by the arrow is well imaged, as are other more continuous events.

1.4.2 Time-lapse seismology and coalbed methane production

Time-lapse reservoir monitoring involves the comparison of seismic images taken of the same strata at different time intervals. No published data have discussed the use of time-lapse monitoring of CBM fields, but the technique has been successfully applied to the Sleipner field of Norway, and at Weyburn, Saskatchewan, to monitor geological sequestration of carbon dioxide (Eiken & Brevik, 2000; Li, 2003).

Carbon dioxide injection and the removal of water, the necessary steps in enhanced CBM recovery, affect the bulk density and seismic velocity within a geological formation. These changes in density and velocity in turn affect the amplitude and travel times of reflected seismic waves (Gunter et al., 1997). It is believed that time-lapse reservoir monitoring of an ECBM project will show amplitude variations and velocity push-down effects, allowing imaging of dewatered zones and, potentially, tracking injected CO_2.

1.5 Study Outline

This thesis makes use of vertical seismic profiles and surface seismic data collected at a coalbed methane test well site near Red Deer, Alberta. At this locale, Suncor Energy Inc., industry partners, and the Alberta Research Council are evaluating the Upper Cretaceous Ardley coal zone for its CBM potential, as well as testing enhanced coalbed methane recovery with carbon dioxide injection. Zero-offset VSP, walkaway VSP, and surface seismic data were acquired using both compressional and shear sources. Survey parameters and the geology of the study area are outlined in chapter two.

Zero-offset VSP data are examined in chapter three, allowing a detailed study of the Vp/Vs character of the shallow strata at this site. Processing flows used in ProMAX VSP processing software and commercial processing flows from Schlumberger Canada are outlined. The results of these processing flows are compared to each other, and to synthetic seismograms, to determine the optimal source for examining these coal seams. All seismic data throughout this work are presented using SEG standard polarity conventions (Thigpen et al., 1975).

Chapter four summarizes coal imaging using the walkaway VSP and surface seismic data. Processing flows for each, again from both ProMAX VSP and Schlumberger Canada are outlined, and P-P and P-S reflectivities of the coal zone are analyzed.

Seismic and well log data collected in this study are used in 1.5-D and 2-D numerical modelling to test the viability of time-lapse seismic imaging of ECBM production. One-dimensional synthetic seismograms are created using SYNTH, a Matlab module, whereas two-dimensional ray tracing makes use of GX2 software. Chapter five details the results of this numerical modelling.

Conclusions and recommendations of this study are summarized in chapter six.

Chapter 2 Study Area & Surveys

2.1 Red Deer Study Site

Vertical seismic profile and surface seismic data were acquired at the Cygnet 9-34-38-28W4 lease, located northwest of Red Deer, Alberta (Figure 2.1). Suncor Energy Inc., industry partners, and the Alberta Research Council are evaluating this site for enhanced coalbed methane recovery. Methane production and carbon dioxide sequestration are both being tested for viability within the Upper Cretaceous Ardley coal zone (Figure 2.2), one of Alberta's most prospective CBM targets. Within Alberta, Ardley coal seams are up to 4 m thick, are laterally continuous over tens of kilometers and may show up to 24 m net coal in a single wellbore (Beaton, 2003).

Within Alberta, the Ardley coal zone has an estimated original gas in place of 53 TCF, of which an estimated 20% is recoverable using current technology (Beaton, 2003). Test wells of the Ardley coal in the Pembina area have demonstrated gas contents ranging from 1.5 to 4.4 cc/g, and permeability between 4 and 10 mD (Hughes et al., 1999). At the test site, the Ardley coal zone is of sub-bituminous 'A' rank, and average gas saturations in the Red Deer region range from 2 to 5 cc/g of coal (equivalent to 3-4 BCF per section) (Beaton, 2003).

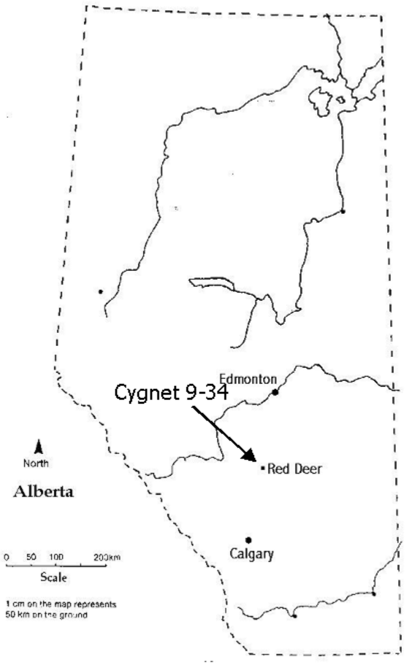

Figure 2.1 Map of Alberta, showing location of Cygnet 9-34-38-28W4 wellbore and VSP data acquisition (Natural Resources Canada, 2002).

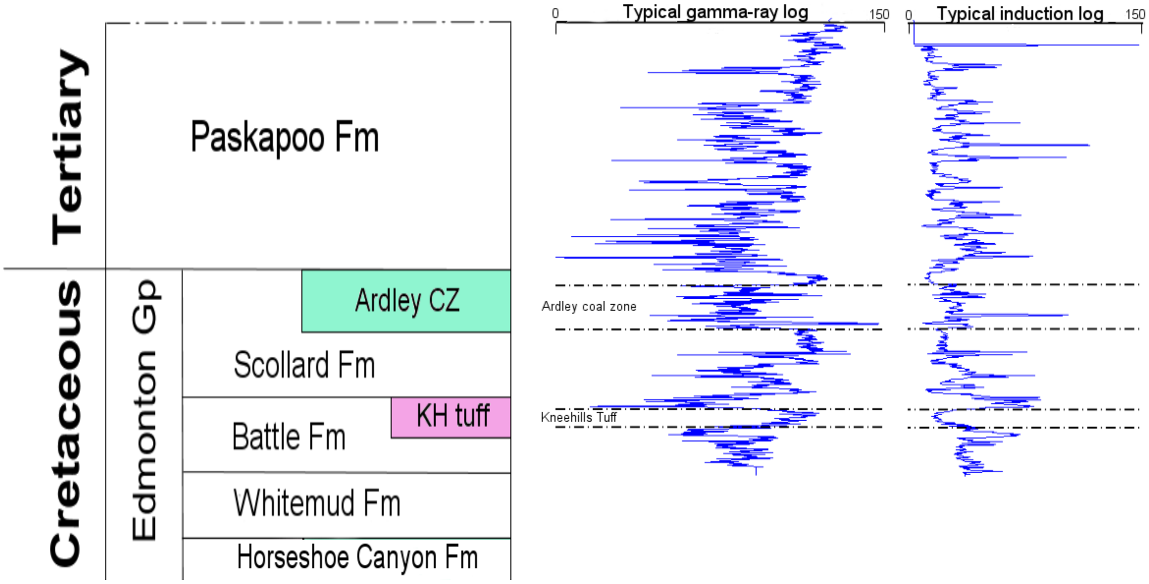

Figure 2.2 Stratigraphic column showing Upper Cretaceous/Tertiary strata in Central Plains of Alberta (after Beaton, 2003).

Ardley coal seams are unconformably overlain by the interbedded sands and shales of the Tertiary Paskapoo Formation, and underlain by Edmonton

Group strata, of similar lithology to the Paskapoo (Figure 2.2). The Kneehills tuff forms an important regional marker bed within the Battle Formation, as it is an easily correlatable, laterally extensive layer containing volcanic ash, displaying low resistivity on well logs, and low seismic velocity (Havard et al., 1968).

2.2 Survey Geometry

Zero-offset vertical seismic profiles (VSPs), multioffset ("walkaway") VSPs, and surface seismic were acquired at the 9-34 lease site. Here, the Ardley coals are at a depth of 282 m below surface. The geometry for all surveys is illustrated in Figure 2.3.

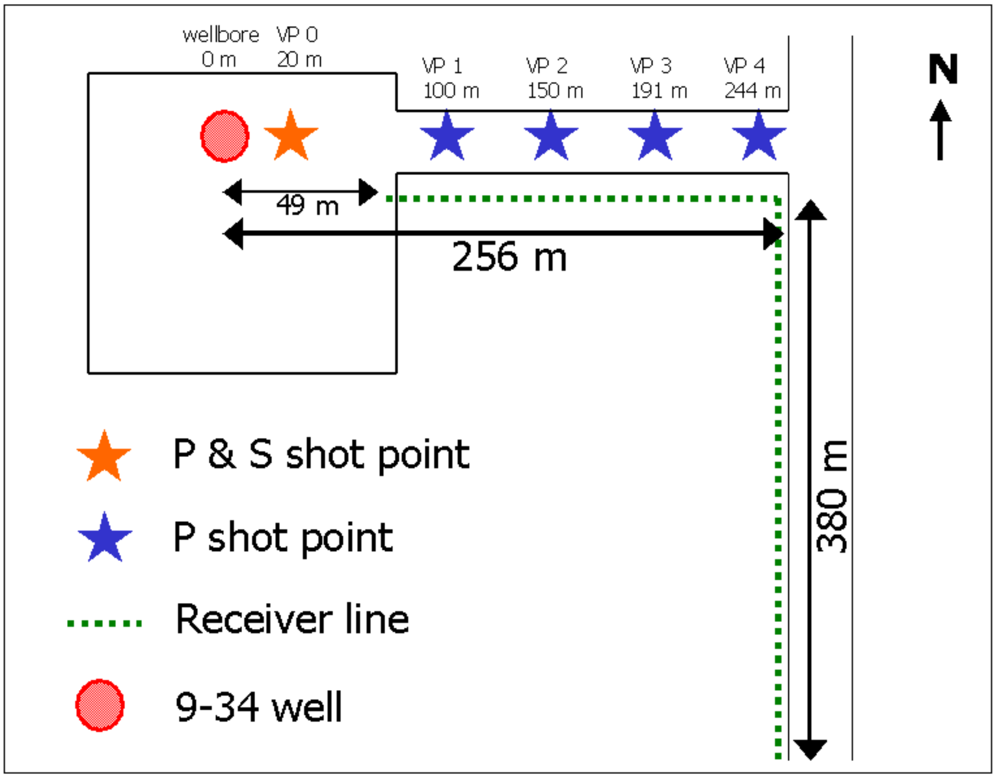

Figure 2.3 Plan view geometry of acquisition at 9-34-38-28W4 near Red Deer. Zero-offset vertical seismic profile sources (compressional and shear) were located at VP0, whereas walkaway source points (compressional only) were located at VP1 to VP4. Surface receivers were spaced at 10 m increments, illustrated by the green dashed line.

Zero-offset VSPs were acquired using a 44,000 lb. vertical vibrator source ("big-P") sweeping 8-150 Hz, a smaller truck-mounted vertical vibrating source ("mini-P") sweeping 8-250 Hz, and a truck-mounted horizontally polarized vibrator source ("mini-S") sweeping 8-150 Hz. In each case, sweep design was limited by the operational limitations set by the source operator. Although high-bandwidth (and thus, high resolution) data were desired to effectively image the coal, it was unknown whether the mini-P source would produce enough energy to generate clear reflections at the depth of the coal. For this reason, both the mini-P and big-P sources were used, to determine which is the better source for imaging coal seams at this site. A shear source was used such that shear-wave velocities in the shallow section could be determined, and to test shear-wave attenuation within the strata. The mini-S source was configured such that the polarization of S-waves was oriented normal to the source-receiver plane. A five-level, three-component VSP tool with a 15 m receiver spacing was used in an interleaved manner such that receivers were spaced at 5 m intervals from TD (300 m) to surface within the wellbore. All recording was undertaken at a 1 ms sampling rate.

Multioffset surveys were conducted using only the compressional sources, that is, the big-P and mini-P. Four shot points east of the borehole were used for these surveys, at offsets of 100 m, 150 m, 191 m, and 244 m from the borehole. For these walkaway surveys, three-component receivers were located at 15 m intervals from TD to surface of the wellbore.

Single vertical-component surface seismic data were recorded during the shooting of the vertical seismic profiles, using a 60-channel Geometrics ‘Strataview’ seismic recorder. Geophones were spread at 10 m intervals east along the lease road and south along the Range road as illustrated in Figure 2.3. Surface data were also recorded, using the zero-offset VSP shots (both mini-P and big-P) as sources, as well as the walkaway shots.

2.3 Open hole well Logs

Open hole wireline logs were obtained by Schlumberger Canada after drilling of the Red Deer well. Compressional sonic, bulk density, gamma-ray, and caliper logs were all run from TD to approximately 40 m below KB. These logs are shown in Figure 2.4.

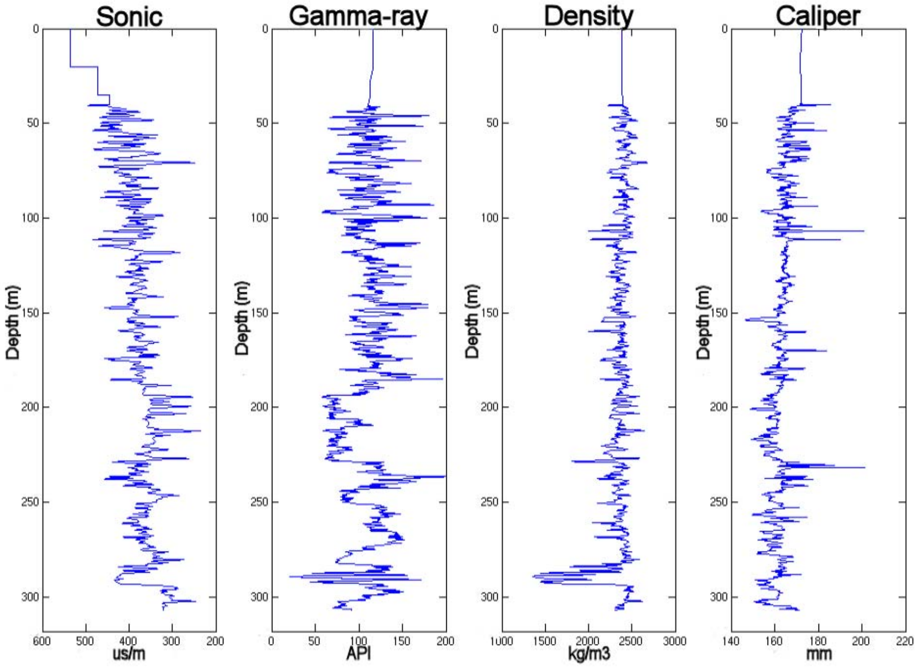

Figure 2.4 Open hole wireline logs recorded in well 9-34-38-28W4. Logs were run from TD to approximately 40 m KB.

Interpretation of these logs gives information about the lithologies penetrated by the wellbore, as well as the physical condition of the strata. The caliper log shows relatively little variation in borehole width, suggesting that little wash-out of strata has occurred during drilling. This in turn suggests that all other tools were able to properly couple with the borehole wall, yielding high quality data. Sonic, density, and gamma-ray logs are used in combination to interpret the Red Deer well data. The overlying and underlying strata are interpreted as interbedded shales and siltstones, and three distinct Paskapoo sand units are identified in addition to the Ardley coal zone (Figure 2.5).

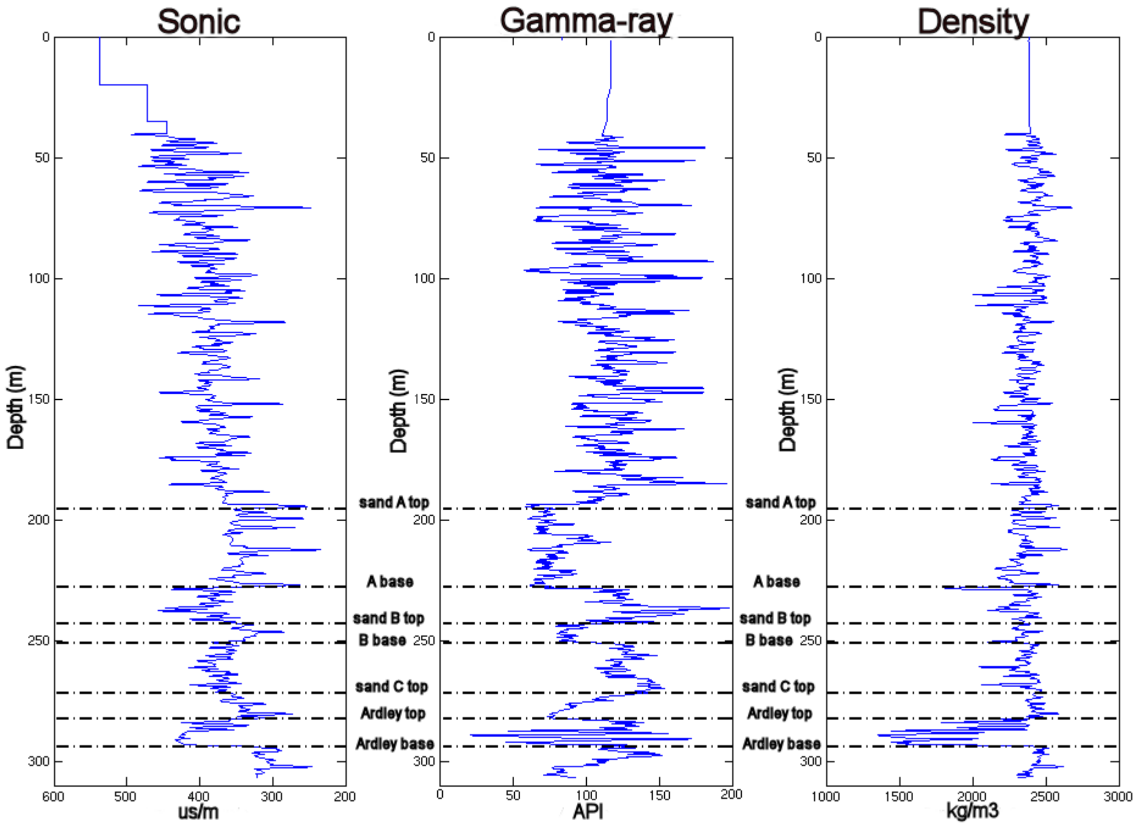

Figure 2.5 Open hole well logs of 9-34 well with lithological tops interpreted. Three sand packages are identified, as well as the Ardley coal zone. Overlying and underlying strata are interpreted to be interbedded siltstones and shales.

The base of the well contains interbedded silts and shales. Overlying these strata is the Ardley coal zone, which is 11.7 m thick, from 282.3 m KB to 294.0 m depth. It is immediately detectable on the well logs by its extremely low density, as well as its low sonic velocity, and low gamma-ray response.

Strata overlying the Ardley coal zone belong to the Paskapoo Formation, which comprises interbedded fluvial sandstones and overbank shales (Smith, 1994). Three separate Paskapoo sand packages were identified by their low gamma-ray counts and relatively low sonic transit times. Sand C, with an upper contact at 272.0 m, immediately overlies the Ardley coal zone. Its gamma-ray profile is characteristic of a fining-upward fluvial sequence, with the cleanest gamma response at its base, becoming increasingly shaley towards the top. Its sharp contact with the underlying Ardley and its fluvial signature lead it to be interpreted as a channel sand.

Sand B is a thinner sedimentary package than sand C, being 8 m thick with an upper contact at 243.0 m. It is characterized by a clean, blocky gamma-ray signature. Sand B is interpreted to be a high-energy channel deposit.

Sand A is 34.6 m thick, and is interpreted to start at 193.5 m KB with its basal contact at 228.1 m KB. The blocky log character with sharp upper and lower contacts suggests a well-sorted fluvial channel, typical of the Paskapoo Formation (Smith, 1994). A thin shaley layer (3-4 m thick) is noted in the middle of this sand body.

2.4 Cased hole logs

Several months following drilling and casing of the 9-34 wellbore, cased hole wireline logs were run to obtain a shear sonic curve. The logging suite included both a compressional and a shear sonic curve. The two sonic logs and the resultant Vp/Vs curve are shown in Figure 2.6, and these data are discussed in Chapter 3.

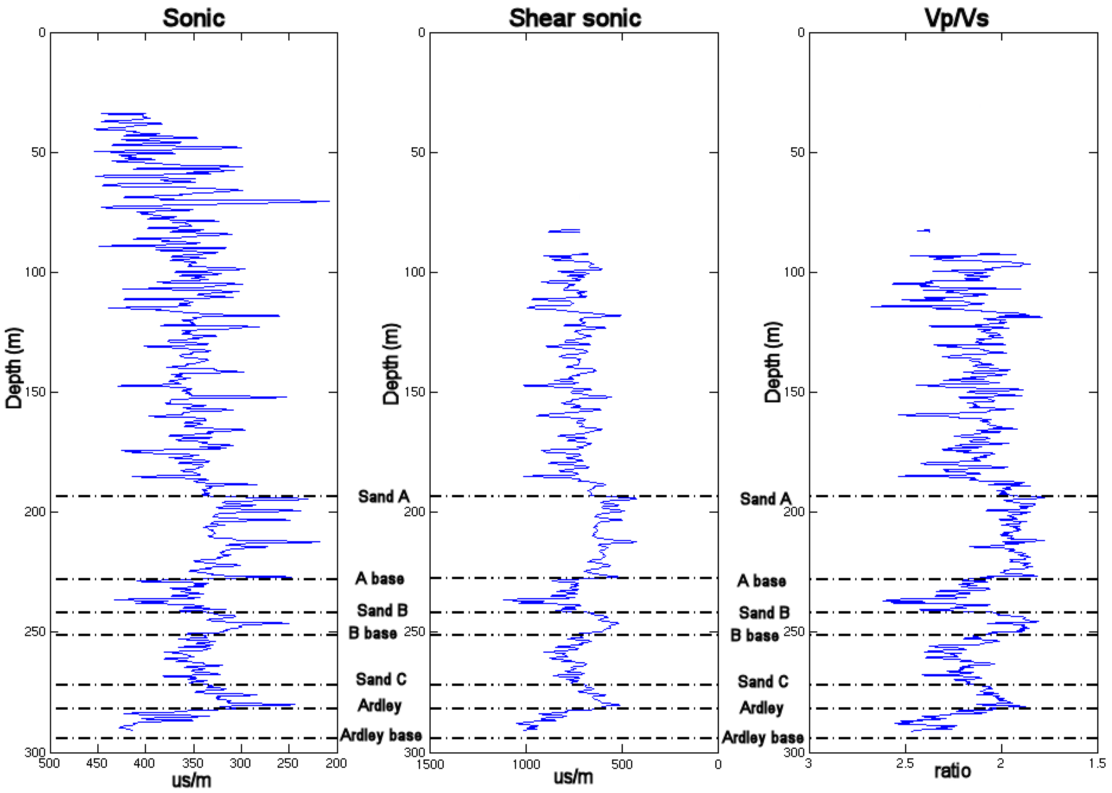

Figure 2.6 Cased hole logs of 9-34-38-28W4. Because of cement in the bottom of the well, it was not possible to log the base of the Ardley coal. Poor quality logs in the upper 100 m of the wellbore (particularly the shear sonic) are likely the result of a cement integrity problem.

The cased hole compressional sonic curve shows great similarity to the open hole log, both in shape and values, indicating a reliable log run. Casing the wellbore resulted in cement in the bottom of the hole, meaning the base of the

Ardley coal could not be reached by logging tools. Lower quality shear sonic readings in the upper portion of the well are likely the result of poor cement integrity.

A cross-plot of open hole vs. cased hole P-wave sonic curves shows generally an excellent correlation between the two data sets (Figure 2.7). This consistency in surveys demonstrates that the cased hole data are as reliable as the open hole data.

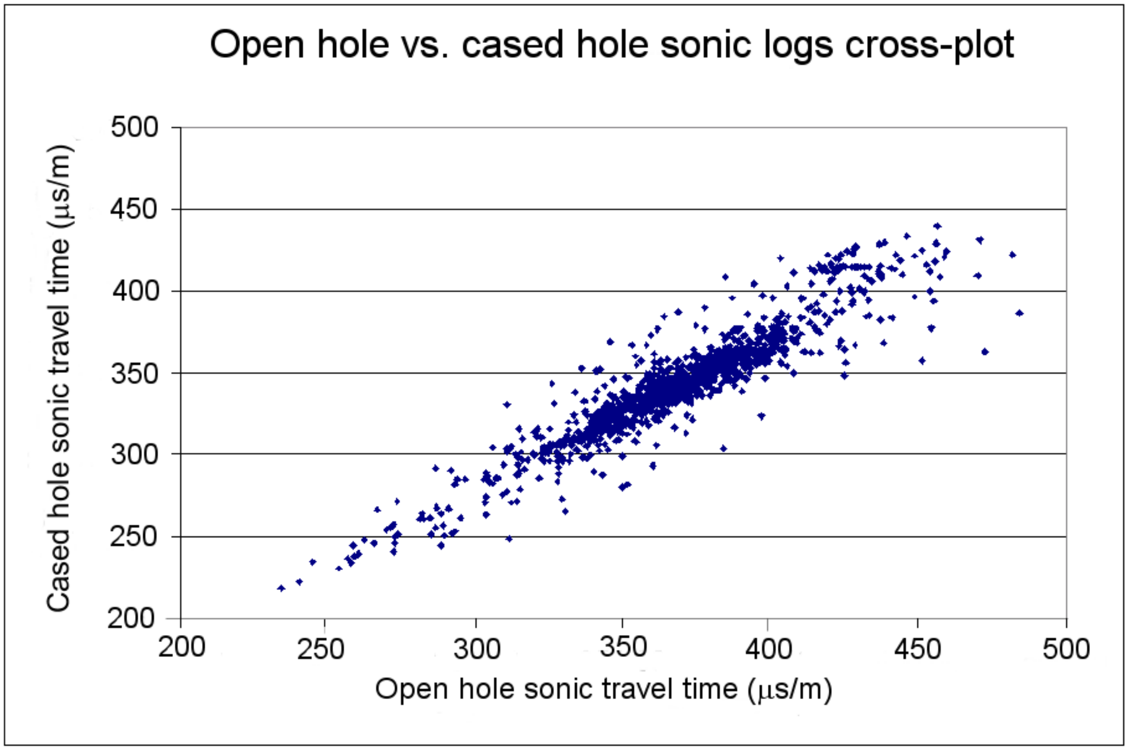

Figure 2.7 Cross-plot of open hole and cased hole P-wave sonic traveltimes. Good correlation is noted between the two data sets.

2.5 Summary

Zero-offset vertical seismic profiles, multi-offset VSPs, and surface seismic data were all obtained at the Red Deer study site to examine the seismic response of the Ardley coal zone. Two compressional sources and one shear source were used for the zero-offset VSP data, whereas the walkaway VSP and surface data were recorded using only compressional sources. At this site, the Ardley occurs at a depth of 282.3 m, and is 11.7 m thick. The coal zone is overlain by strata of the Paskapoo Formation, including three channel sands identified on open hole well logs. Cased hole logs were also run, including a dipole shear sonic curve.

Chapter 3 Zero-offset VSP Analysis

3.1 Raw zero-offset data

Data recorded at the Red Deer test site are of excellent quality. Raw data shows only one poorly coupled receiver (at 114 m depth) throughout all surveys, evidenced by the noisy trace at this receiver. The uppermost receiver, at 20 m depth, shows considerable noise. Both downgoing and upgoing energy can be distinguished on raw data for the mini-P, big-P and mini-S sources, illustrated in Figure 3.1, Figure 3.2, and Figure 3.3, respectively. All seismic data are plotted using the SEG standard polarity, that is, a positive amplitude (peak) on a P-P section indicates a P-wave impedance increase, whereas a positive amplitude on a P-S section indicates an increase in S-wave impedance (Thigpen et al., 1975).

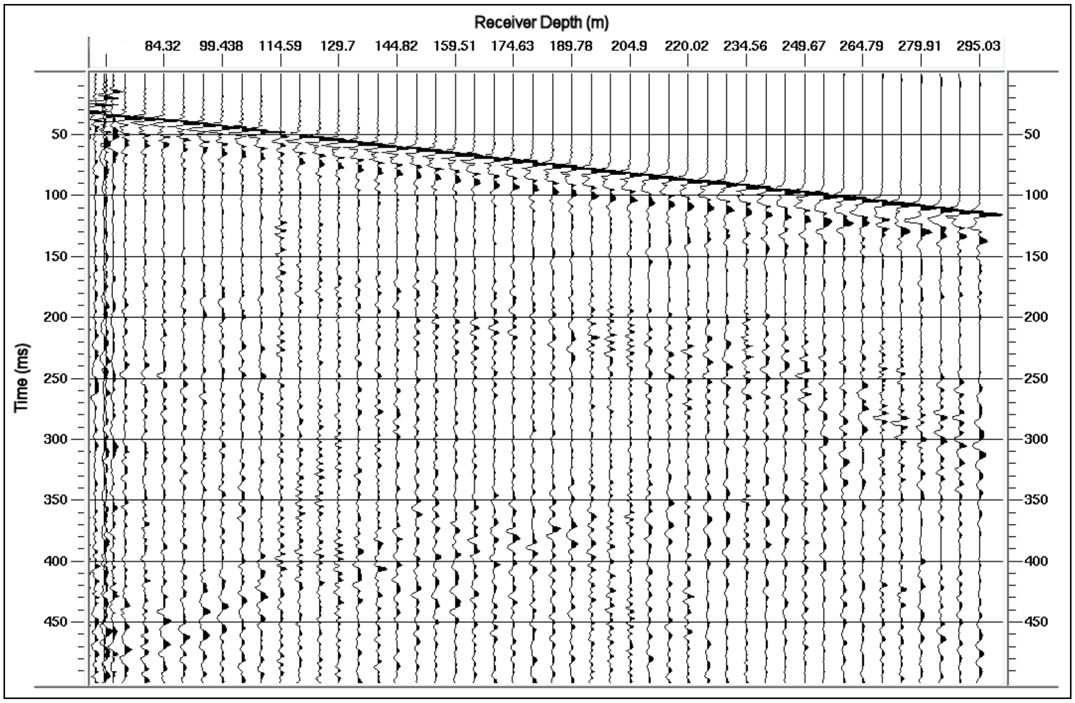

Figure 3.1 Summed raw vertical-component data recorded for mini-P zero-offset vertical seismic profile at Red Deer. Automatic gain correction (200 ms operator length) applied.

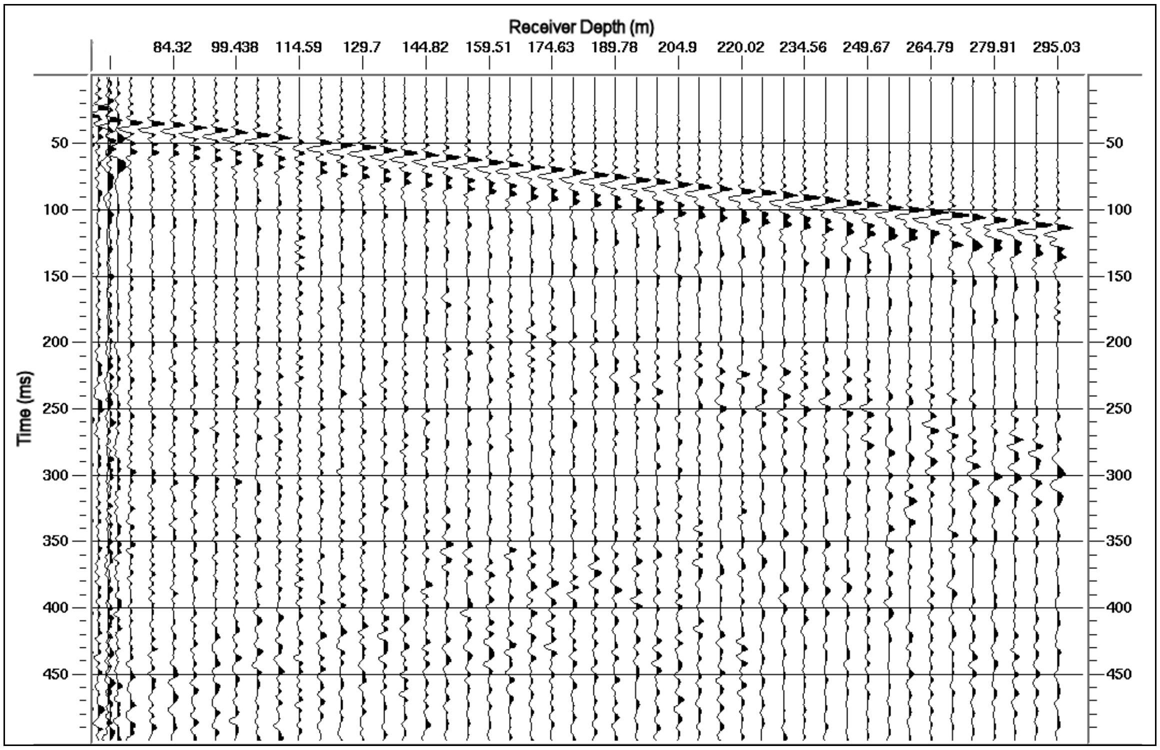

Figure 3.2 Summed raw vertical-component data recorded for big-P zero-offset vertical seismic profile at Red Deer. Automatic gain correction (200 ms operator length) applied.

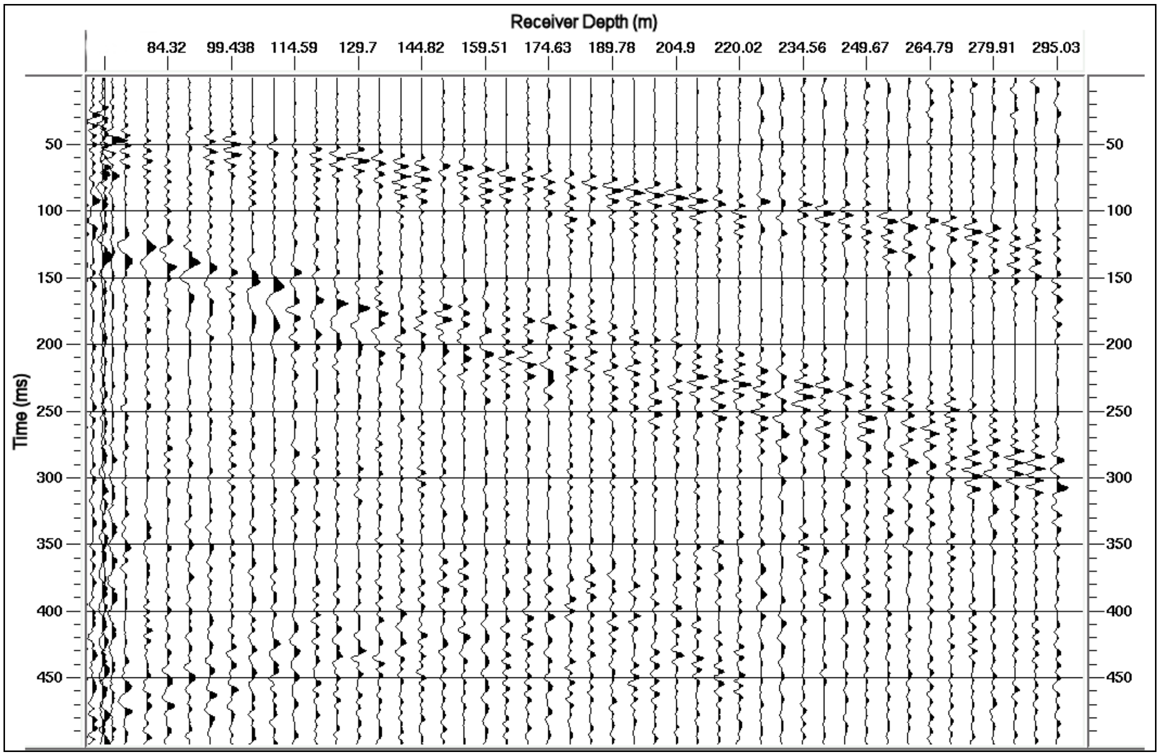

Figure 3.3 Summed raw horizontal-component data for mini-S zero-offset vertical seismic profile at Red Deer. Automatic gain correction (200 ms operator) applied.

First breaks picked on these data sets were used to examine average and interval velocities of the strata.

3.2 Vp/Vs analysis of shallow strata

Recording of the zero-offset VSPs from TD to surface allowed a detailed examination of the seismic velocities of shallow strata in the Red Deer section. Interval and average velocities, and Vp/Vs were calculated using first arrival times for mini-P and mini-S energy at each receiver (Table 3.1). First breaks were picked on each data set by picking the maximum of the first coherent peak, according to the Vibroseis convention used by Schlumberger. First breaks from the shallowest receiver were obscured by noise (Figures 3.1 to 3.3), resulting in inaccurate velocity calculations at this level. For this reason, data values from the uppermost receiver were excluded from the analysis. For simplicity, only the mini-P data were used for the P-wave velocity determinations.

Average velocities were calculated using the formula:

$$V_{avg} = \frac{t_n}{z_n}$$

where t_n is the first-break travel time at receiver n, and z_n is the distance traveled to receiver n, calculated using receiver depth and 20 m source offset, assuming straight ray-paths and a vertical wellbore.

To create a smoother profile, interval velocities were calculated for 15 m intervals rather than for every receiver, using the formula:

$$V_{\text{int}} = \frac{t_n - t_{n-3}}{z_n - z_{n-3}}$$

where *z* is calculated in the same manner as above.

Rec #	Depth (m)	Int Vp (m/s)	Int Vs (m/s)	Int Vp/Vs	Avg Vp (m/s)	Avg Vs (m/s)	Avg Vp/Vs
1	20.01	2854.8	2481.7	1.15	2854.8	2481.7	1.15
2	35.13	2302.3	489.0	4.71	2663.0	1116.4	2.39
3	50.24	2390.6	649.7	3.68	2588.5	945.0	2.74
4	65.36	2432.2	743.2	3.27	2554.2	894.3	2.86
5	74.51	2991.8	897.6	3.33	2597.6	894.7	2.90
6	80.48				2553.2	893.3	2.86
7	84.32				2578.4	894.9	2.88
8	89.62	2470.9	894.4	2.76	2576.4	894.6	2.88
9	94.62				2577.6	903.5	2.85
10	99.44				2584.2	913.5	2.83
11	104.74	2658.5	1073.0	2.48	2587.5	915.8	2.83
12	109.74				2593.5	924.6	2.81
13	119.86				2589.9	931.5	2.78
14	124.89	2611.7	1114.5	2.34	2591.3	942.1	2.75
15	129.7				2596.6	953.4	2.72
16	134.98				2592.2	951.2	2.73
17	139	2443.1	1040.3	2.35	2575.8	951.0	2.71
18	144.82				2599.0	973.7	2.67
19	149.52				2611.7	972.5	2.69
20	154.58	3062.9	1369.7	2.24	2617.0	980.7	2.67
21	159.51				2619.5	988.3	2.65
22	164.63				2612.5	989.7	2.64
23	169.69	2654.2	1159.8	2.29	2620.2	994.2	2.64
24	174.63				2625.8	995.4	2.64
25	179.75				2614.0	1000.6	2.61
26	184.81	2663.9	1220.5	2.18	2623.7	1009.3	2.60
27	189.78				2626.7	1011.0	2.60
28	194.87				2625.6	1014.3	2.59
29	199.93	2816.3	1237.8	2.28	2637.2	1023.5	2.58
30	204.9				2642.1	1033.8	2.56
31	209.99				2648.3	1040.3	2.55
32	215.05	2939.5	1567.7	1.87	2656.2	1048.8	2.53
33	220.02				2660.5	1053.3	2.53
34	224.53				2675.9	1055.8	2.53
35	229.53	3197.7	1086.0	2.94	2684.7	1051.1	2.55
36	234.56				2681.8	1062.9	2.52
37	239.65				2673.2	1064.8	2.51
38	244.64	2669.6	1304.7	2.05	2683.8	1063.8	2.52
39	249.67				2685.4	1069.6	2.51
40	254.79				2681.8	1072.7	2.50
41	259.76	2860.1	1321.0	2.17	2693.4	1075.9	2.50
42	264.79				2686.6	1076.0	2.50
43	269.91				2677.3	1077.7	2.48
44	274.03	2487.8	1087.9	2.29	2681.9	1076.5	2.49
45	279.06				2679.8	1075.8	2.49
46	284.03				2673.3	1073.8	2.49
47	289.03	2691.1	1311.3	2.05	2682.4	1086.6	2.47
48	294.06				2672.9	1079.8	2.48

Table 3.1 Velocity and Vp/Vs values extracted from first arrival times of mini-P and mini-S zero-offset VSP data.

Average P-wave and S-wave velocities demonstrate generally lower velocities in the near-surface, gradually increasing with depth (Figure 3.4). Analysis of the first arrival times from both sources demonstrates high average Vp/Vs (approximately 3.0) in the shallowest strata down to 100 m depth, decreasing to a value of slightly less than 2.5 at 300 m (Figure 3.5). The highest interval Vp/Vs is 4.7, at 40 m depth (Figure 3.6). Interval velocities are smoothed by plotting at 15 m intervals.

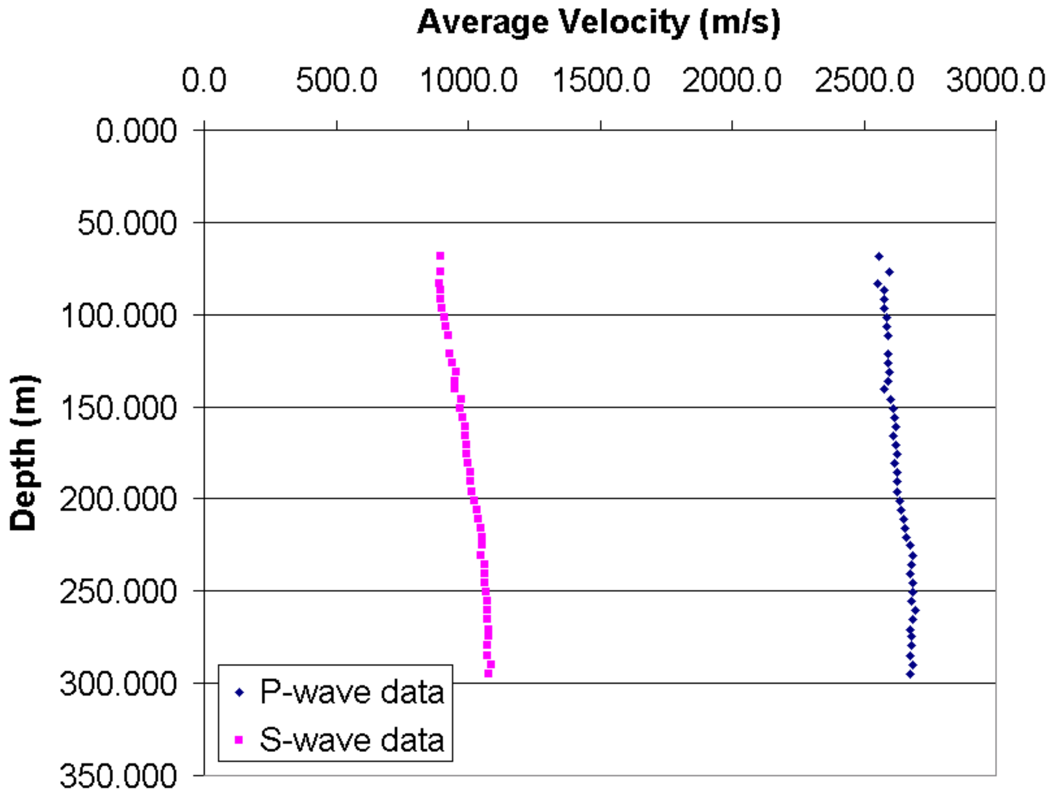

Figure 3.4 Average velocity vs. depth derived from zero offset mini-P and mini-S VSP data.

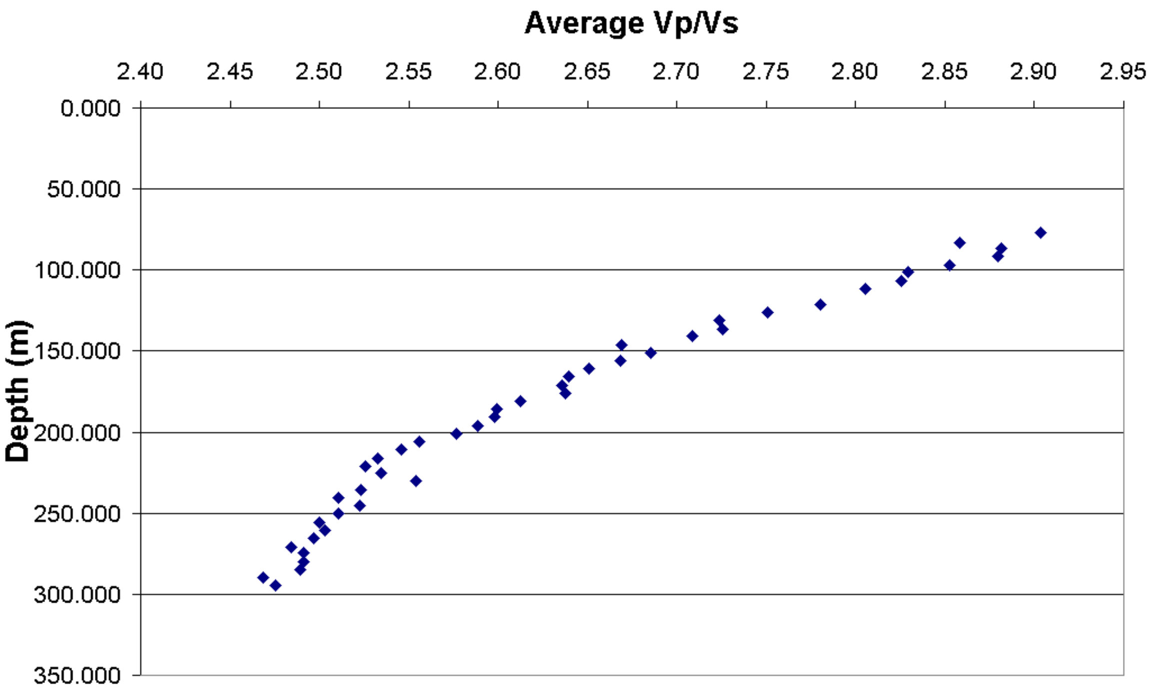

Figure 3.5 Average Vp/Vs vs. depth for zero-offset VSP. High values are noted in the near-surface, decreasing gradually to less than 2.5 at the base of the well.

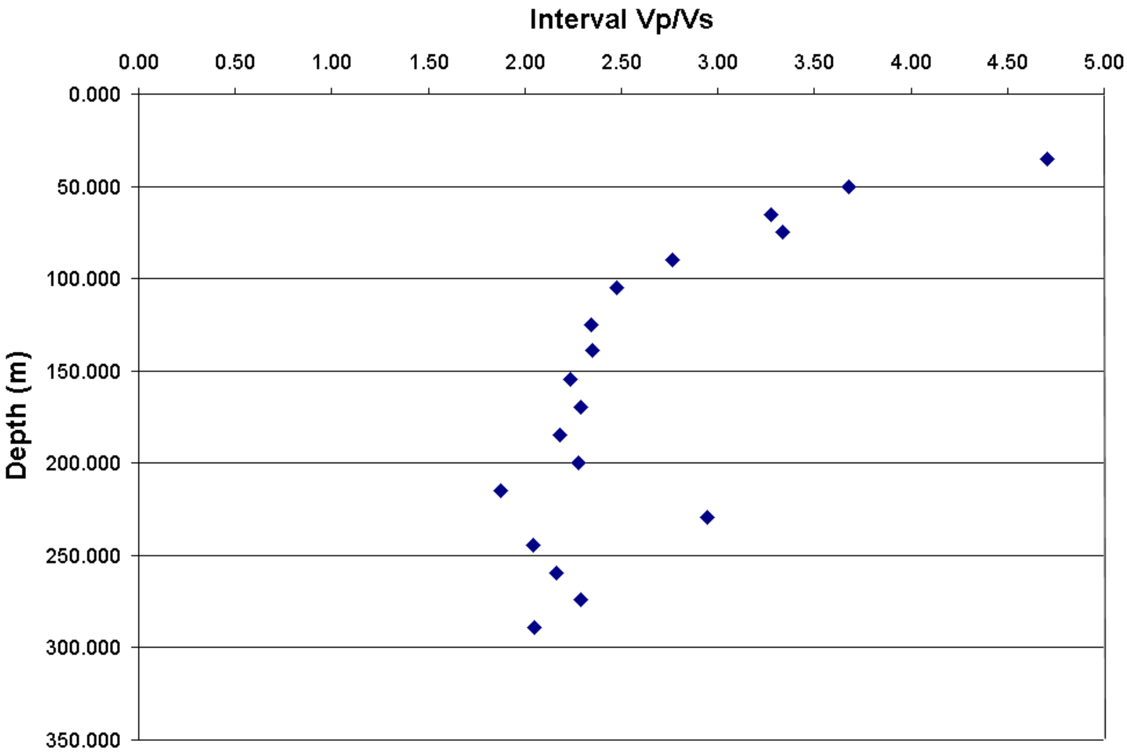

Figure 3.6 Interval Vp/Vs values vs. depth for Red Deer strata, plotted in 15 m increments rather than for every receiver.

Comparing Vp/Vs determined from the VSP data to those determined from well log analysis shows a good correlation (Table 3.2). For comparison purposes, the cased hole Vp/Vs log was smoothed using a 31-sample median filter, and instantaneous Vp/Vs found at each depth. Given the log sample interval of 0.1524 m, a 31-sample filter equals approximately 4.75 m in length. Log values are not available at depths of less than 100 m, however most recorded values match the seismic Vp/Vs values well (Figure 3.7). Although the log data do not show as wide a range of values as the seismic data, the general trend of Vp/Vs is consistent between the two data sets, with most values differing very little. This suggests that either well log or seismic data may be used for numerical modelling purposes and will produce similar results.

Depth (m)	Log Vp/Vs	VSP Vp/Vs
75	unavailable	3.33
87.5	unavailable	2.86
100	2.10	2.31
112.5	2.29	2.34
125	2.06	2.01
137.5	2.13	2.40
150	2.07	2.12
162.5	2.06	2.32
175	2.13	2.73
187.5	2.04	2.25
200	1.93	2.02
212.5	1.94	1.90
225	1.94	3.13
237.5	2.32	2.00
250	2.03	1.90
262.5	2.19	2.30
275	2.05	3.00
287.5	2.33	2.42
300	unavailable	2.80

Table 3.2 Comparison of cased hole log Vp/Vs with Vp/Vs derived from zero-offset VSP data. Correlation is good between the two data sets.

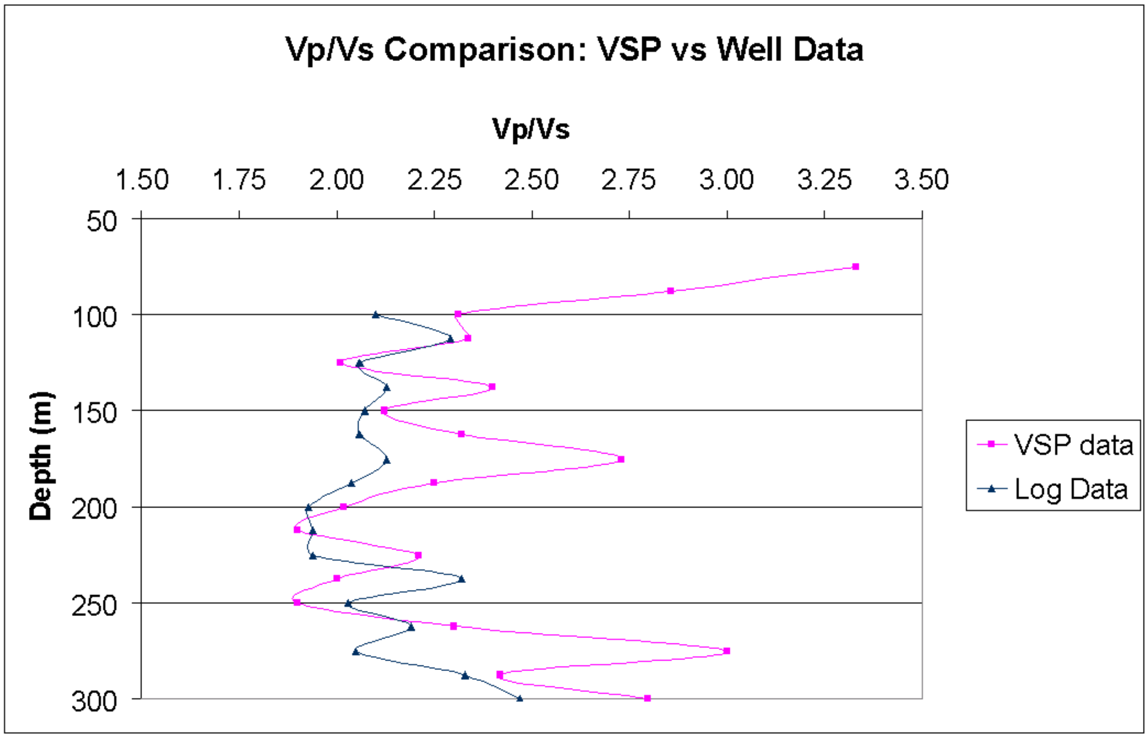

Figure 3.7 Comparison of Vp/Vs values derived from zero-offset VSP data with those derived from well log data.

In addition to the favourable comparison of Vp/Vs from both well log and seismic data, integration of both the P-wave and S-wave sonic logs (Figure 3.8 and Figure 3.9, respectively) results in traveltimes that also match the seismic data well. Table 3.3 summarizes the 2-way traveltimes derived from integrated logs (integrated from the top of logs (approximately 50 m) to the total depth of logs) and those derived from VSP data. Dispersion results in seismic velocities that are generally slower than those calculated by integrating well logs. When well log traveltimes are integrated, the velocity dispersion is determined to be approximately 2.3% for P-wave data and approximately 6.8% for shear-wave data (Figure 3.10).

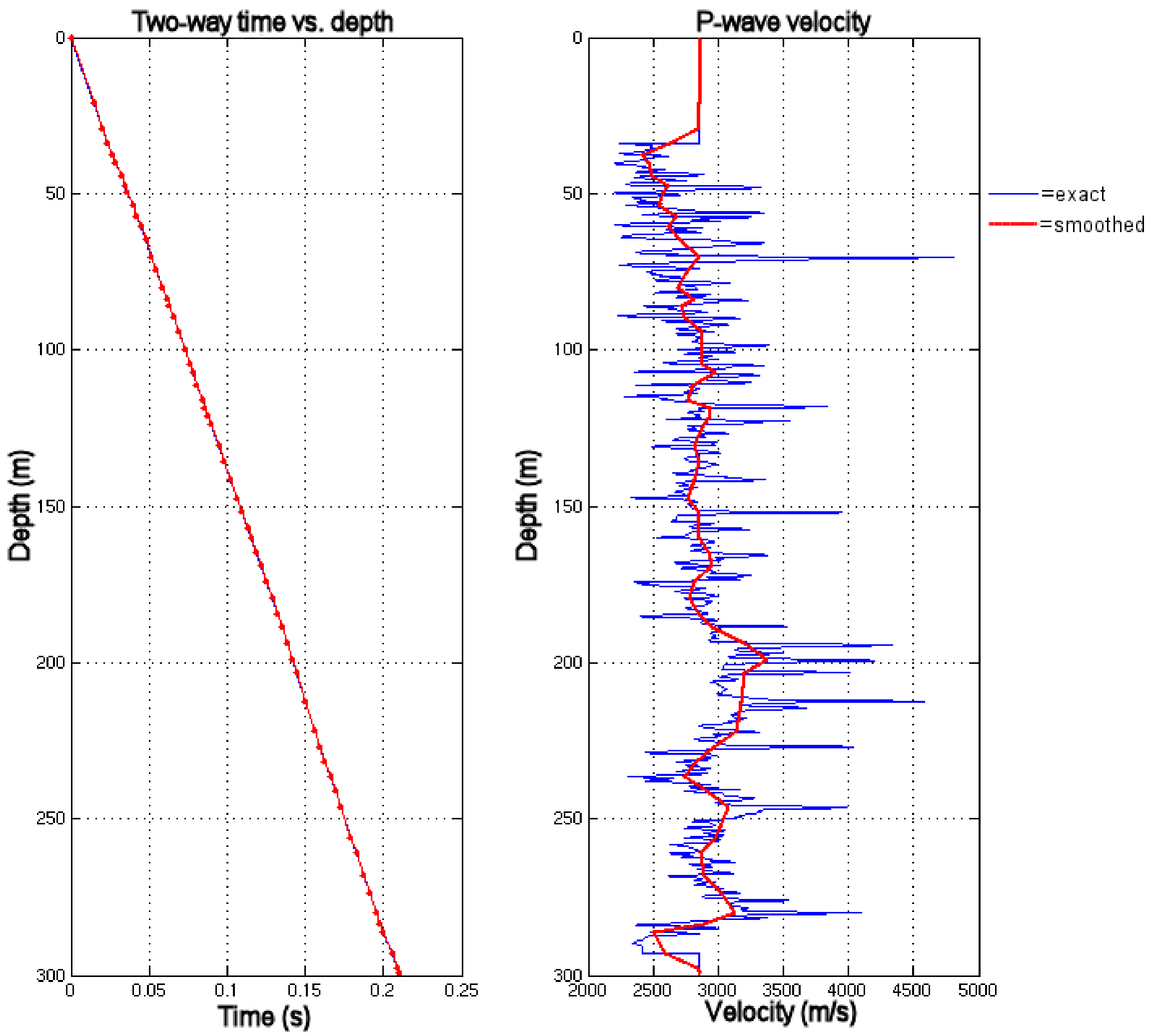

Figure 3.8 Integrated P-wave sonic log, showing calculated instantaneous velocities and two-way travel times with depth.

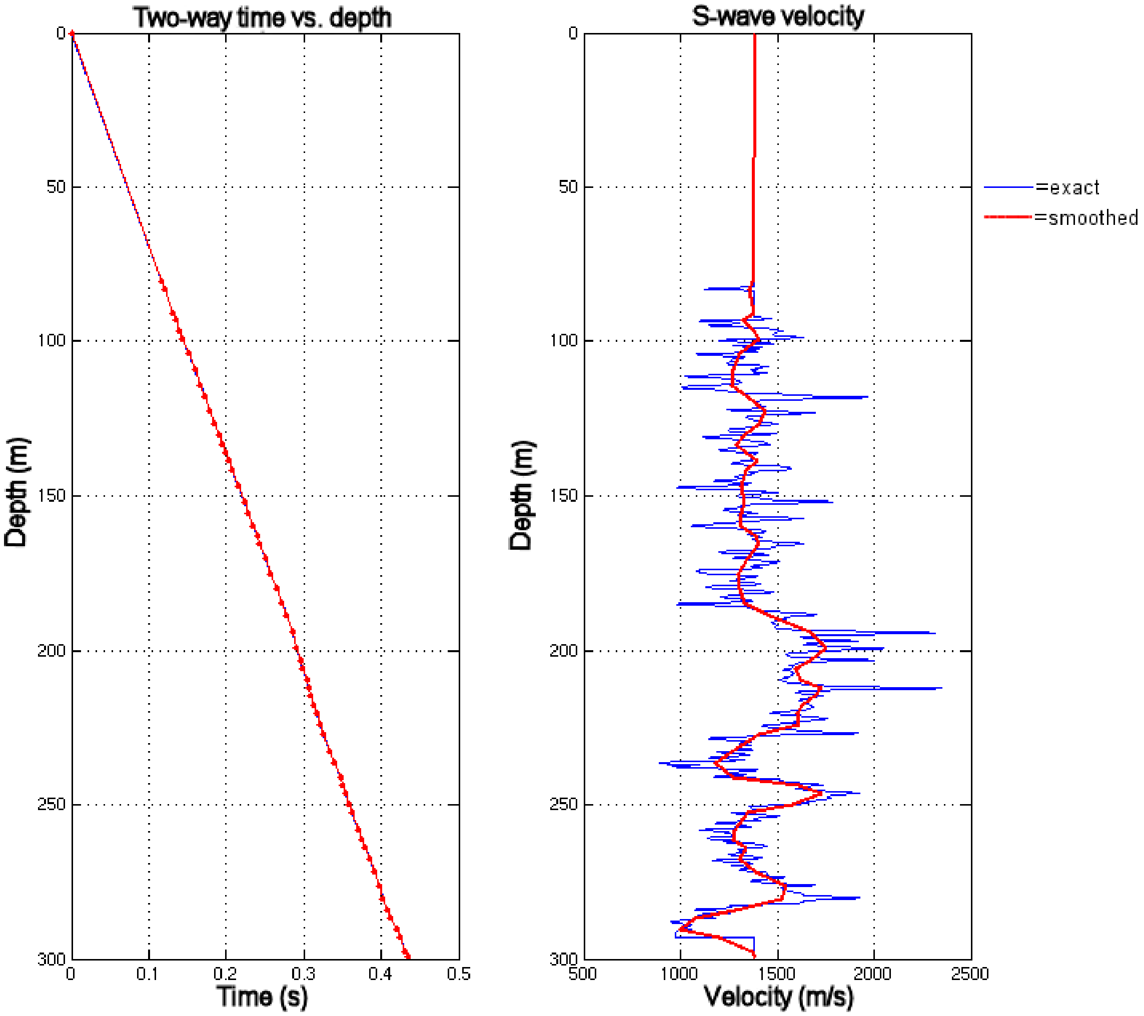

Figure 3.9 Integrated S-wave sonic log, showing calculated instantaneous velocities and two-way travel times with depth.

Depth (m)	P-wave sonic 2-way traveltime	P-wave seismic 2-way traveltime	S-wave sonic 2-way traveltime	S-wave seismic 2-way traveltime
50	0.035	0.040	0.070	0.114
100	0.075	0.078	0.150	0.222
150	0.109	0.116	0.221	0.310
200	0.142	0.152	0.290	0.392
250	0.178	0.186	0.355	0.468
300	0.215	0.220	0.435	0.544

Table 3.3 Comparison of 2-way traveltimes calculated from integrated well logs (from top of well logs to TD) with those calculated from zero-offset VSP data.

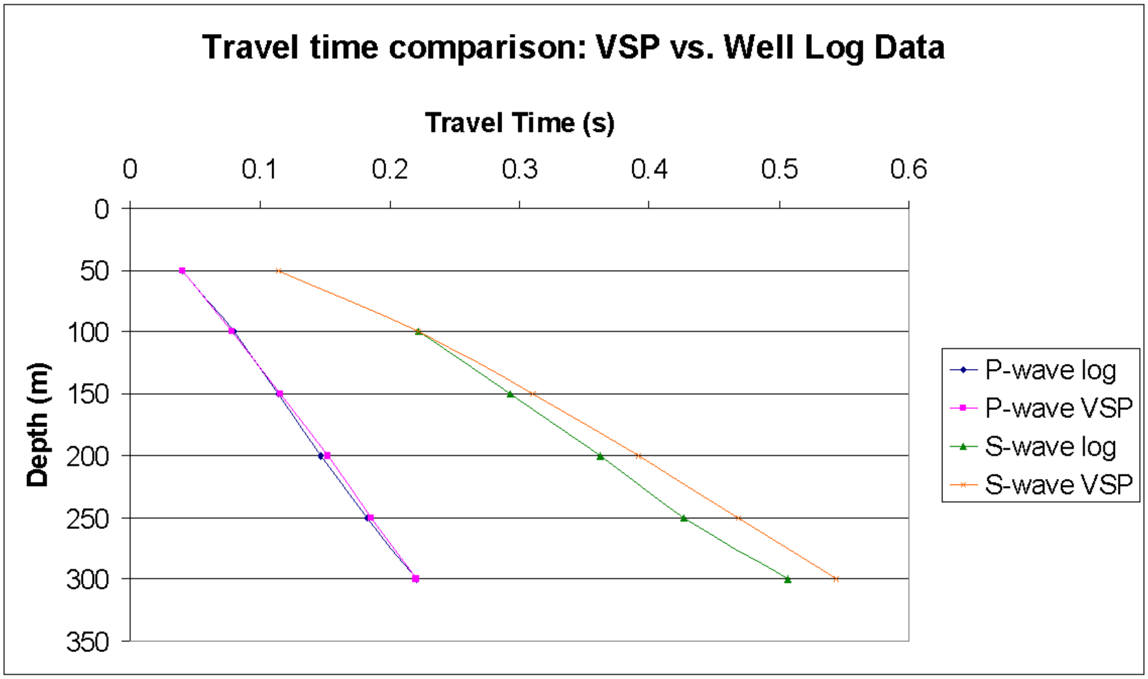

Figure 3.10 Graphical comparison of 2-way traveltimes calculated from integrated well logs with those calculated from zero-offset VSP data.

Vp/Vs profiles of shallow strata are rarely determined in such detail as in the Red Deer survey, as the majority of vertical seismic profiles do not include receivers in the shallow section. At Red Deer, interval Vp/Vs values are high (greater than 4.5) nearest the surface, gradually decreasing with depth to approximately 2.0. These values agree well with published data regarding near-surface velocities, as summarized in Table 3.4.

Depth (m)	Hamilton (1976,1979) Marine silts & turbidites	Toksöz & Stewart(1984) Dallas, TX	Lawton (1990) Calgary, AB	Osborne & Stewart (2001) Pikes Peak, SK	Hoffe & Lines (1999) Blackfoot, AB	Jaramillo & Stewart (2002) Whiterose, NL	Cieslewicz (1999) Chin Coulee, AB	Sun (1999), Cold Lake, AB	Study data (2003) Red Deer, AB
6			2.0				2.8		
12							5.1		
18			8.0				4.7		
20			8.0						
35		3.6							4.7
50	5.2			5.0				4.0	3.7
65		5.7							3.3
75									3.3
100	4.5	5.8		4.6		3.9		4.0	2.3
125									2.0
150	4.0	3.7		4.3				2.9	2.1
175									2.7
200	4.0			4.0		3.9		3.1	2.2
225									3.1
250	3.8			3.8	2.4			3.1	3.3
275									3.0
300	3.7			3.5		3.8		3.0	2.8
350				3.5	2.3				

Table 3.4 Comparison of shallow interval Vp/Vs in various areas. Red Deer values show a trend similar to other published data.

Hamilton (1976, 1979), one of the first to predict Vp/Vs relationships in shallow strata, relied on shallow marine and land in-situ measurements, and derived empirical relationships to predict Vp/Vs with increasing depth. This prediction has proved to be reasonably accurate.

Both within Alberta and in other parts of the world, several determinations of Vp/Vs within the shallow section have found high values nearest the surface, decreasing gradually with depth. This pattern is seen in the very near surface at Chin Coulee, where Vp/Vs of approximately 5.0 was calculated using refraction methods in sediments of 6-18 m depth (Cieslewicz, 1999), and near Calgary, where a Vp/Vs of 8.0 was found using refraction methods at depths of 10-20 m (Lawton, 1990). In both of these studies, lower Vp/Vs values were found above the water table.

Vertical seismic profiles have been used to identify this pattern of decreasing Vp/Vs with depth at Pikes Peak, in Saskatchewan (Osborne & Stewart, 2001), and at a site near Dallas, Texas (Toksöz & Stewart, 1984). Compressional and shear-sonic well logs may also be used in examining Vp/Vs of shallow strata, and have been used to delineate the Vp/Vs profile at Blackfoot, Alberta (Hoffe & Lines, 1999), at Cold Lake, Alberta (Sun, 1999), and in offshore data, such as a Whiterose well, offshore Eastern Canada (Jaramillo & Stewart, 2002). In the Whiterose case, well logs started at a depth of 350 m, but the Vp/Vs relationship demonstrated a similar character to those observed in the shallow section for this study. The Whiterose trend was extrapolated to shallower depths to calculate the expected Vp/Vs behaviour.

3.3 Mini-P zero-offset processing

3.3.1 Schlumberger mini-P processing

Zero-offset VSP vertical-component data sets were processed by Schlumberger Canada. In addition, the mini-P data set was processed using ProMAX VSP, a commercial VSP processing package available at the University of Calgary. Schlumberger’s processing flow is outlined in Figure 3.11.

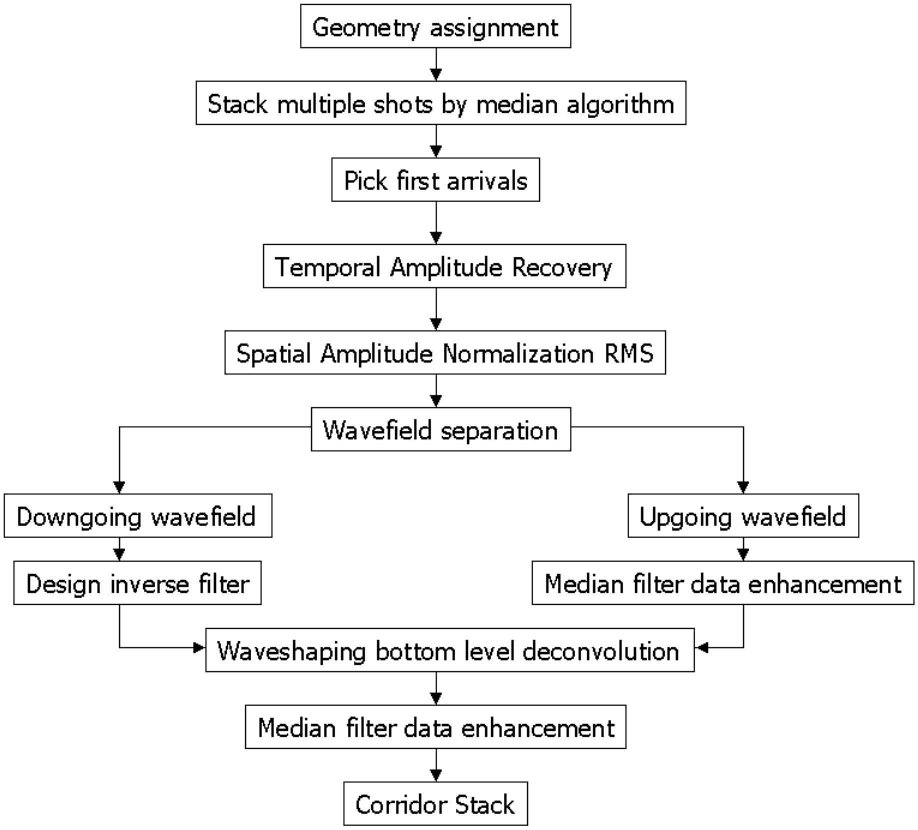

Figure 3.11 Processing flow used to process zero-offset mini-P VSP data (Schlumberger).

After geometry assignment and separation of vertical components, multiple shots were summed using a median algorithm, and first breaks were picked (Figure 3.12). Temporal amplitude recovery (with a time-power constant of 1.7) and spatial amplitude normalization RMS (with a 0.1 s time window) were used to compensate for spherical divergence and transmission losses (Figure 3.13). Wavefield separation was accomplished by use of an eleven-trace median filter. Flattened downgoing energy is illustrated in Figure 3.14, whereas the upgoing wavefield is shown in Figure 3.15.

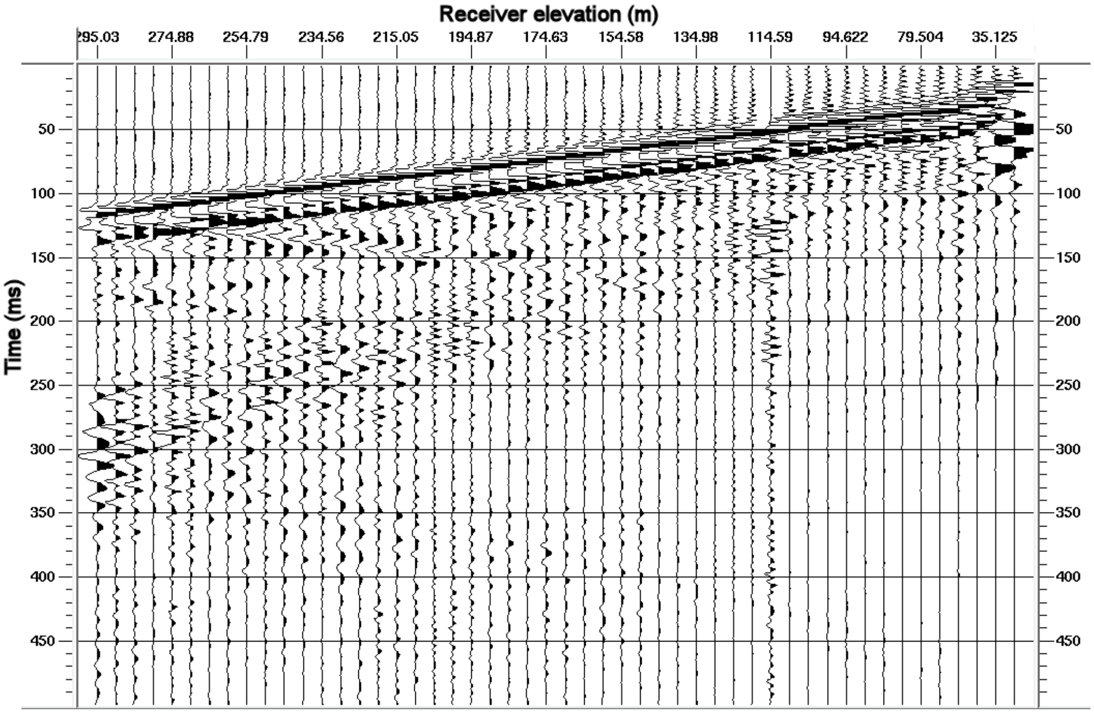

Figure 3.12 Raw zero-offset mini-P data, stacked by median algorithm. First breaks were picked on this data set (Schlumberger).

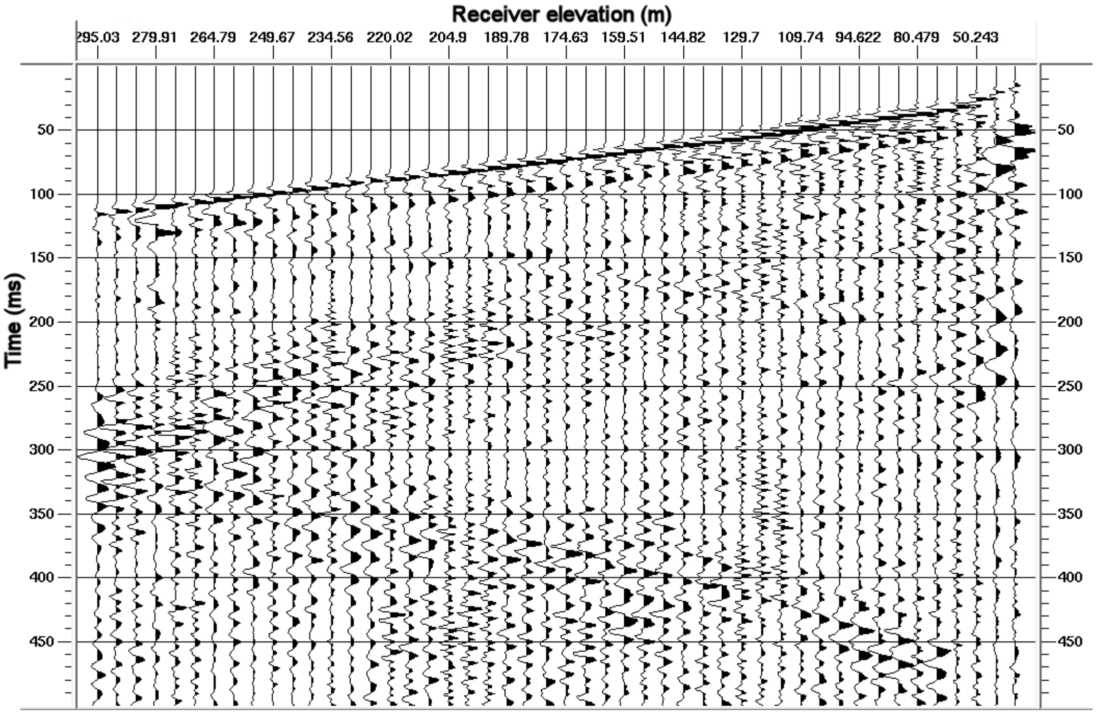

Figure 3.13 Zero-offset mini-P data after correction for spherical divergence and transmission losses using temporal amplitude recovery and spatial amplitude normalization (Schlumberger).

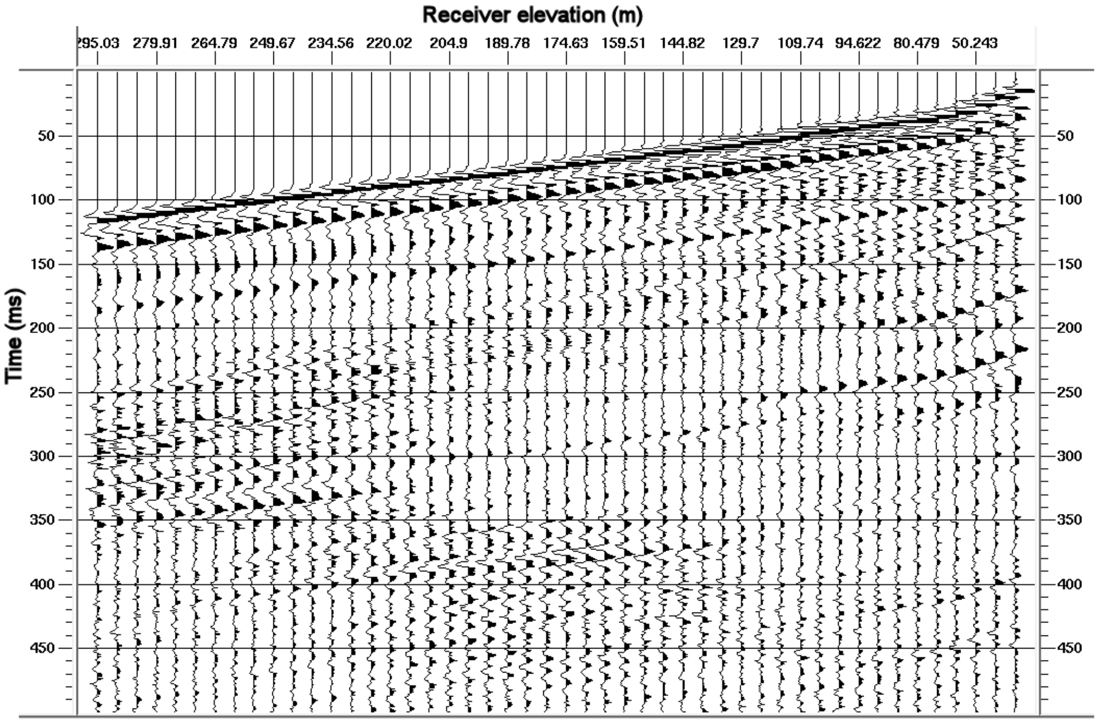

Figure 3.14 Downgoing energy separated from zero-offset mini-P data (Schlumberger).

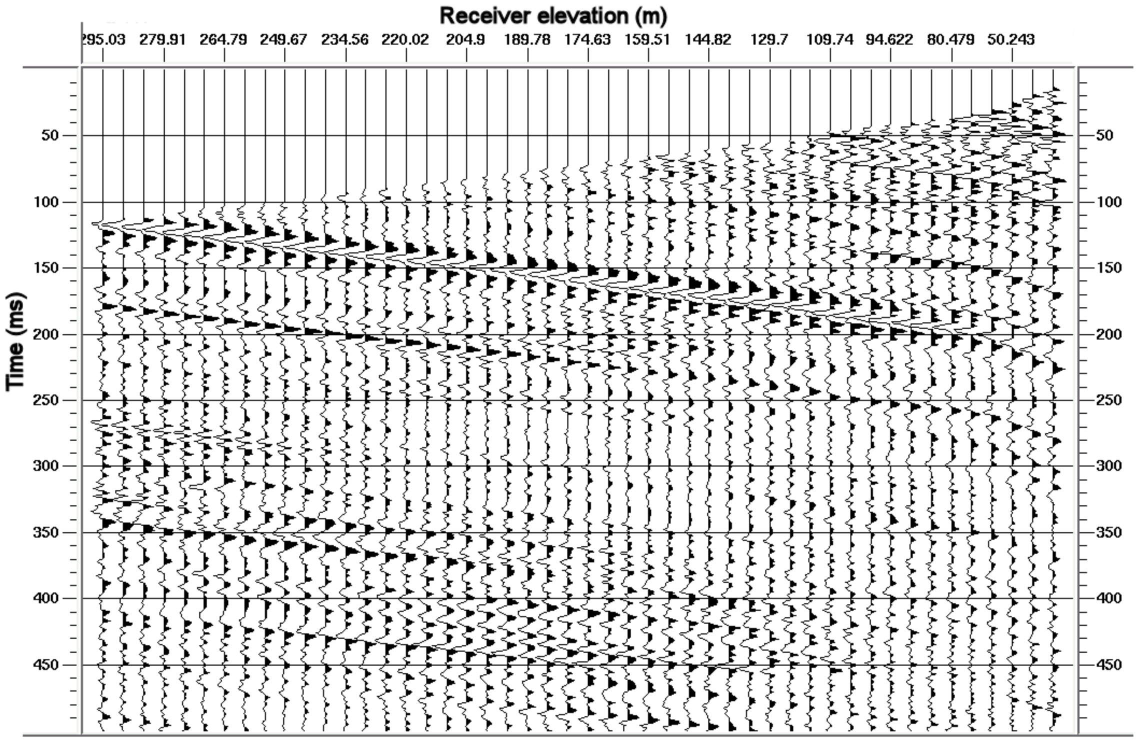

Figure 3.15 Upgoing wavefield separated from zero-offset mini-P data using an 11-trace median filter (Schlumberger).

Another median filter (5 traces) was applied to enhance the separated upgoing wavefield, and waveshaping bottom level deconvolution (using a 0.6 s time window and 1.0% white noise) was used to remove the effect of the source signature from the upgoing energy (Figure 3.16). The data were once again enhanced with a three-trace median filter (Figure 3.17). A corridor stack was produced by defining the top and bottom of the corridor, and by adding first arrival times to convert the data to two-way time (Figure 3.18). Various bandpass filters were tested on the final corridor stack (Figure 3.18).

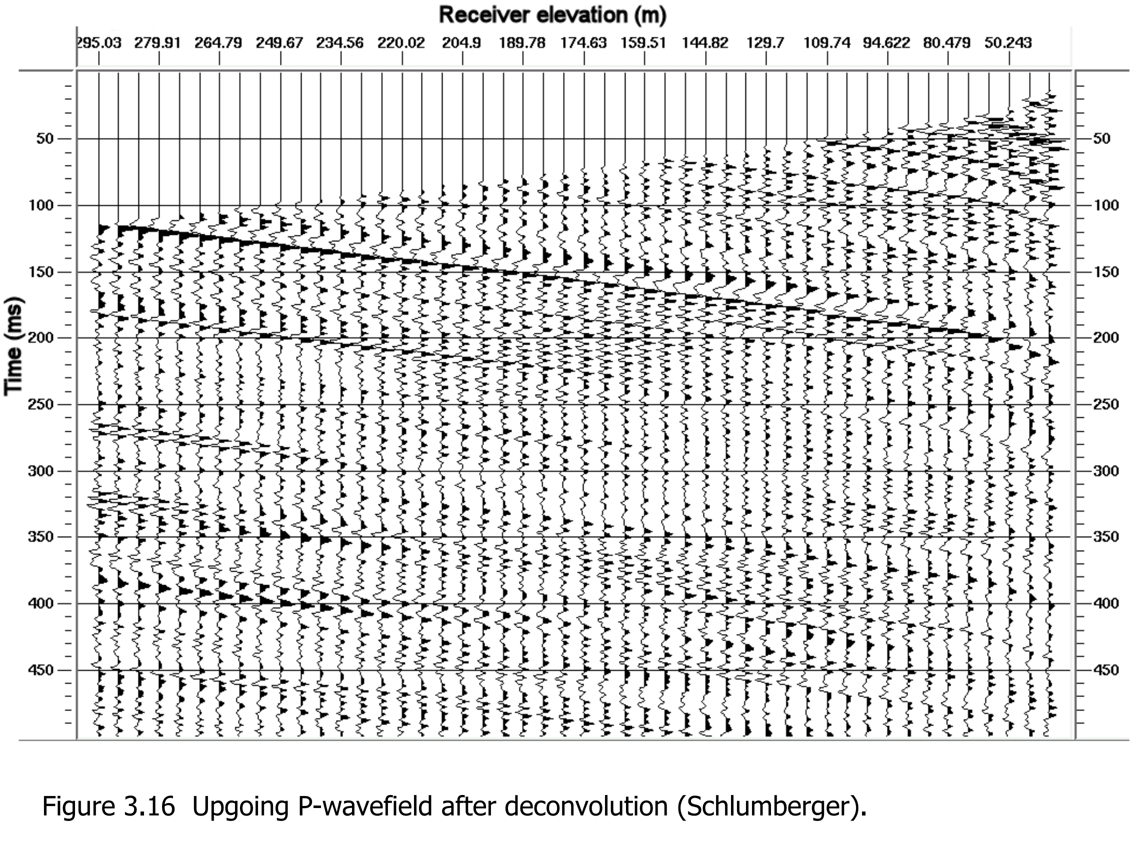

Figure 3.16 Upgoing P-wavefield after deconvolution (Schlumberger).

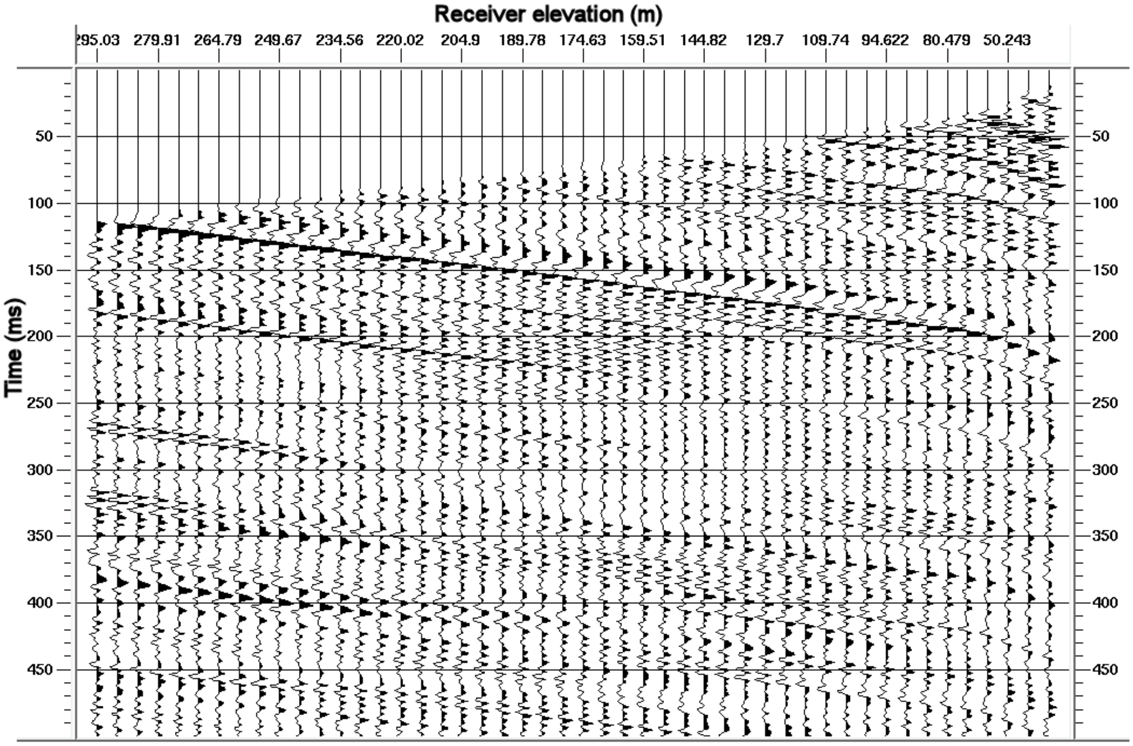

Figure 3.17 Deconvolved upgoing P-wavefield after enhancement using a 3-trace median filter (Schlumberger).

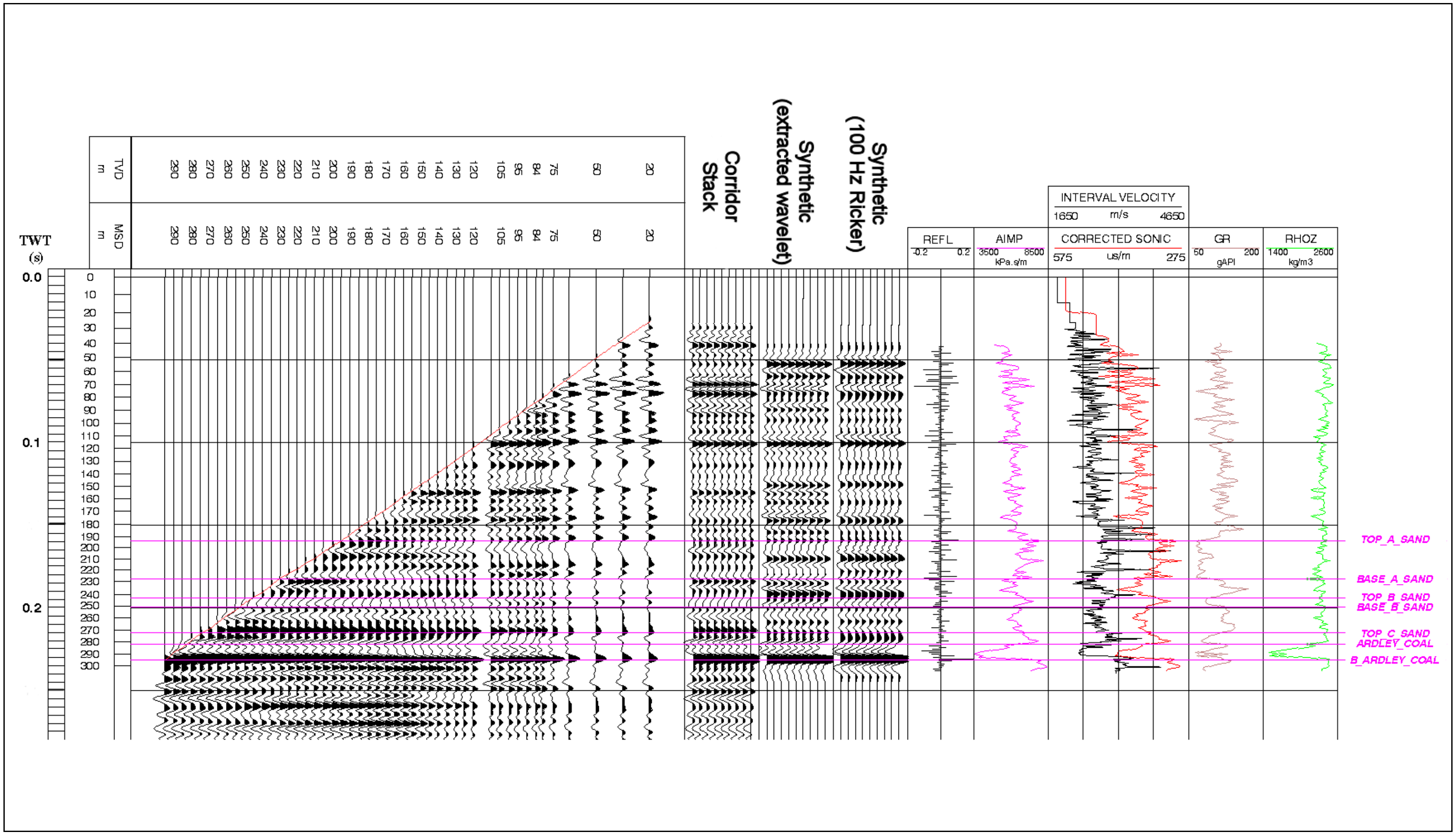

Figure 3.18 Final corridor stack of upgoing P-wavefield from zero-offset mini-P data (Schlumberger).

3.3.2 ProMAX VSP mini-P processing

ProMAX processing of the mini-P data set used a flow (Figure 3.19) very similar to that used by Schlumberger. After separating vertical components, assigning geometry and stacking multiple shots using a mean algorithm, first breaks were picked. Average velocity vs. depth was calculated using these first break times, then converted to RMS velocity vs. depth for use in true amplitude recovery and spherical divergence correction. True amplitude recovery used a 6 dB/sec correction and a time-power constant of 1.2 (Figure 3.20).

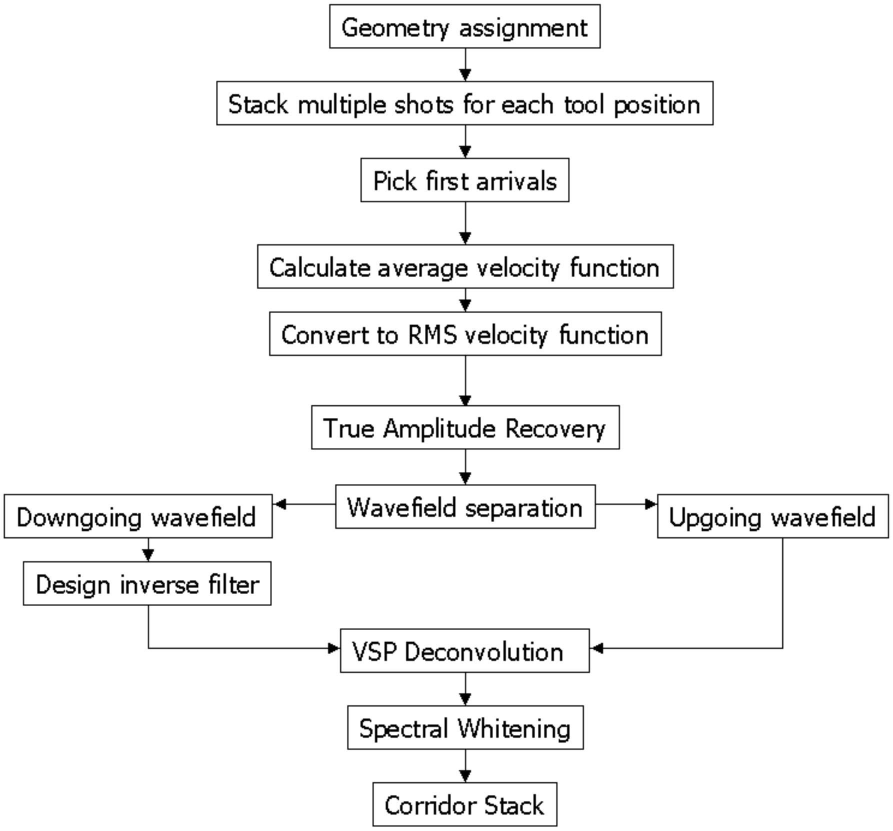

Figure 3.19 Processing flow used to process zero-offset mini-P VSP data using ProMAX VSP.

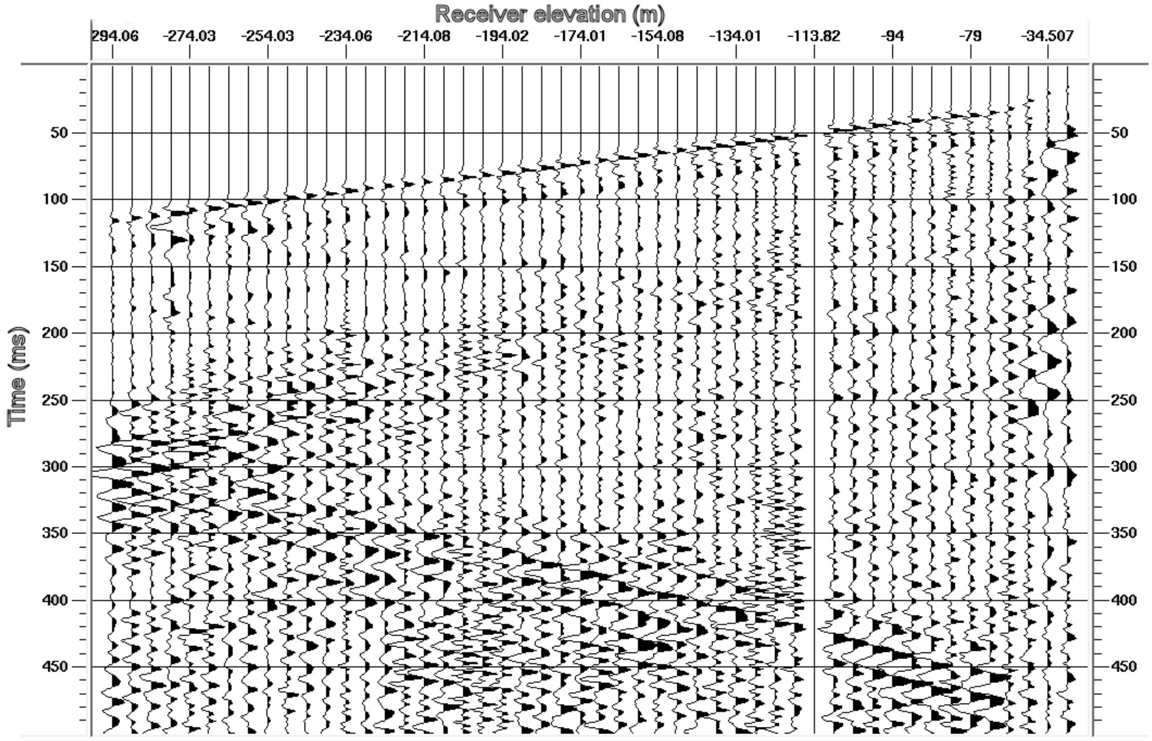

Figure 3.20 Zero-offset mini-P data after correcting for spherical divergence and transmission losses (ProMAX VSP).

A seven-trace median filter was used to separate upgoing and downgoing energy, and a bandpass filter (10-20-200-250 Hz) applied to enhance the upgoing wavefield. The flattened downgoing wavefield and the separated upgoing wavefield are illustrated in Figure 3.21 and Figure 3.22, respectively.

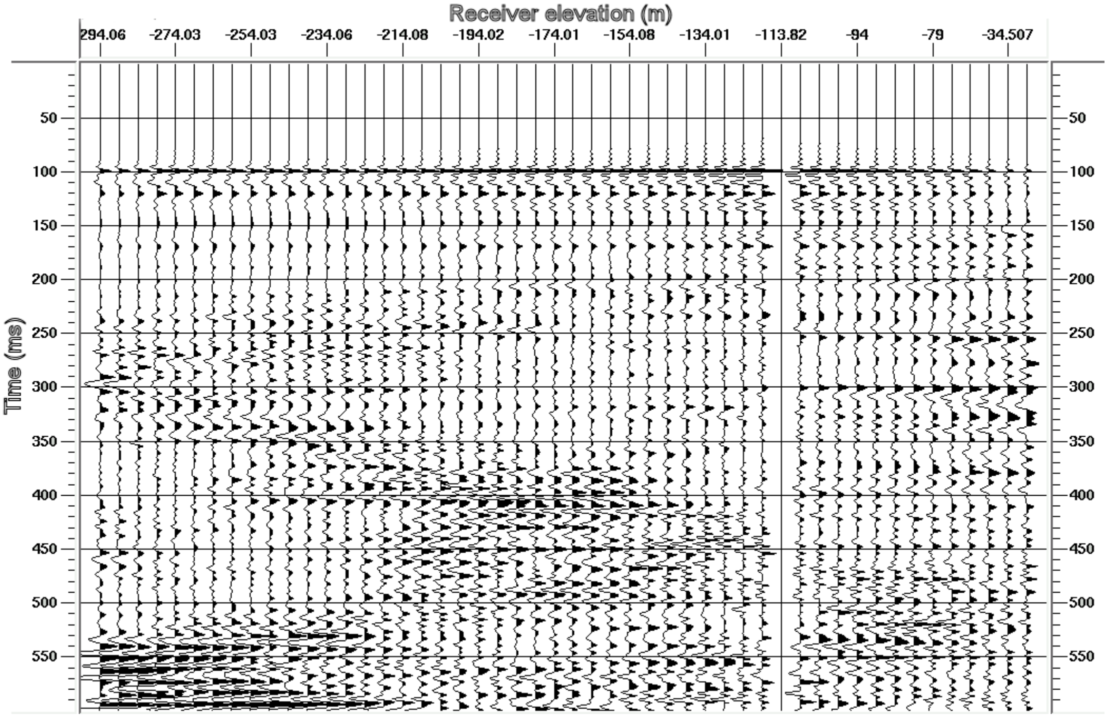

Figure 3.21 Flattened downgoing wavefield separated from zero-offset mini-P VSP data using a 7-trace median filter (ProMAX VSP).

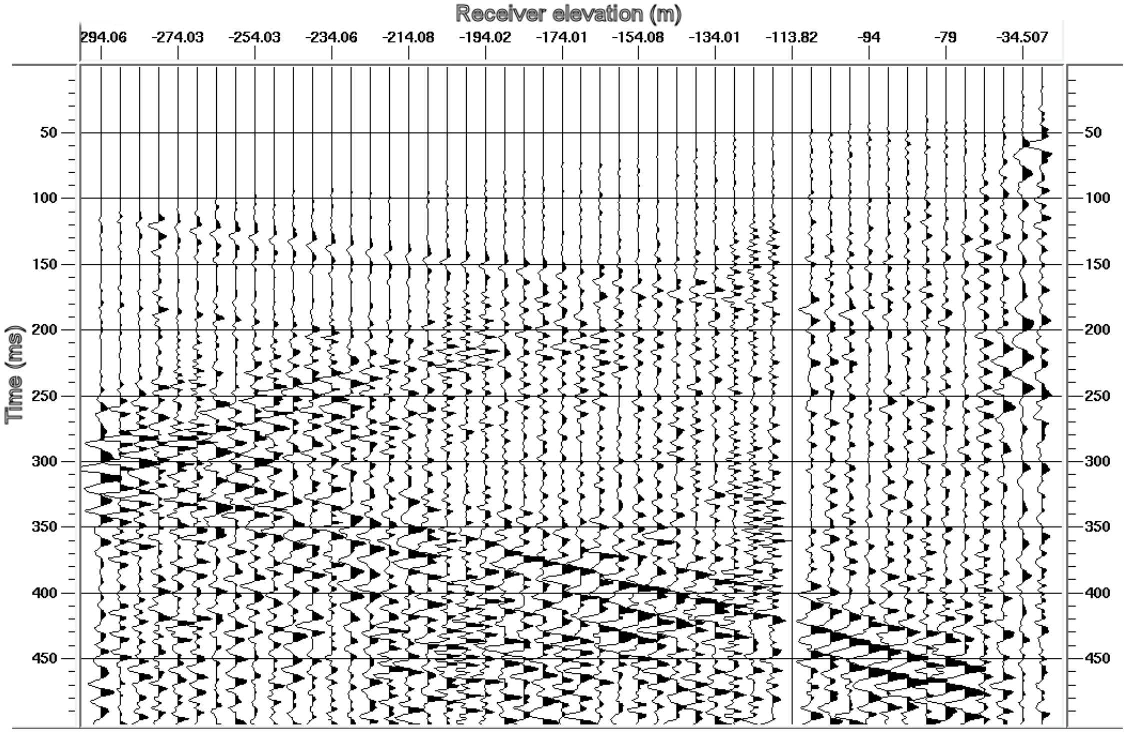

Figure 3.22 Smoothed upgoing wavefield separated from zero-offset mini-P data using median filter (ProMAX VSP).

VSP deconvolution was used to remove the effect of the source signature from the upgoing energy, using a 0.3 s time window and adding 1% white noise (Figure 3.23). The inverse filter was designed using the separated downgoing wavefield.

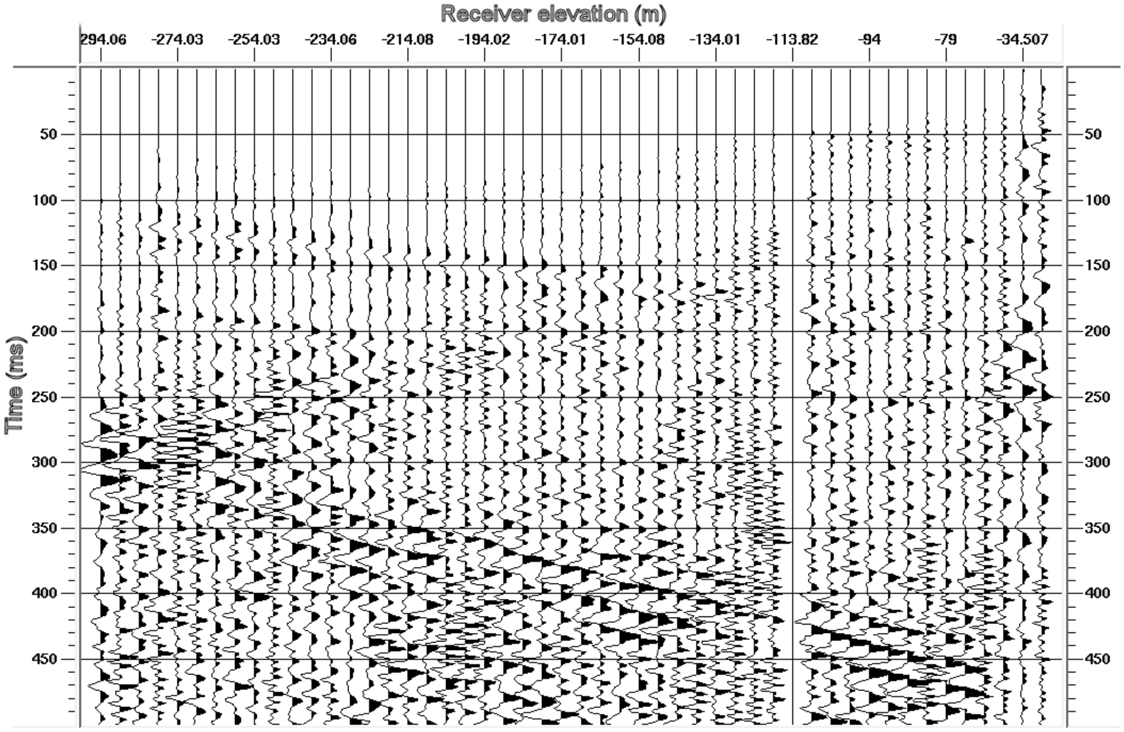

Figure 3.23 Deconvolved upgoing wavefield extracted from zero-offset mini-P data. VSP deconvolution used a 0.3 s time window, and added 1% white noise (ProMAX VSP).

Spectral whitening (10-20-240-260 Hz) was applied to the deconvolved upgoing energy, and a corridor stack created (using 40 ms corridor width) by shifting the data to two-way time and stacking data to form a single trace. This trace is repeated several times in the corridor stack display (Figure 3.24).

A comparison of the corridor stacks resulting from Schlumberger's processing and ProMAX VSP processing is illustrated in Figure 3.25.

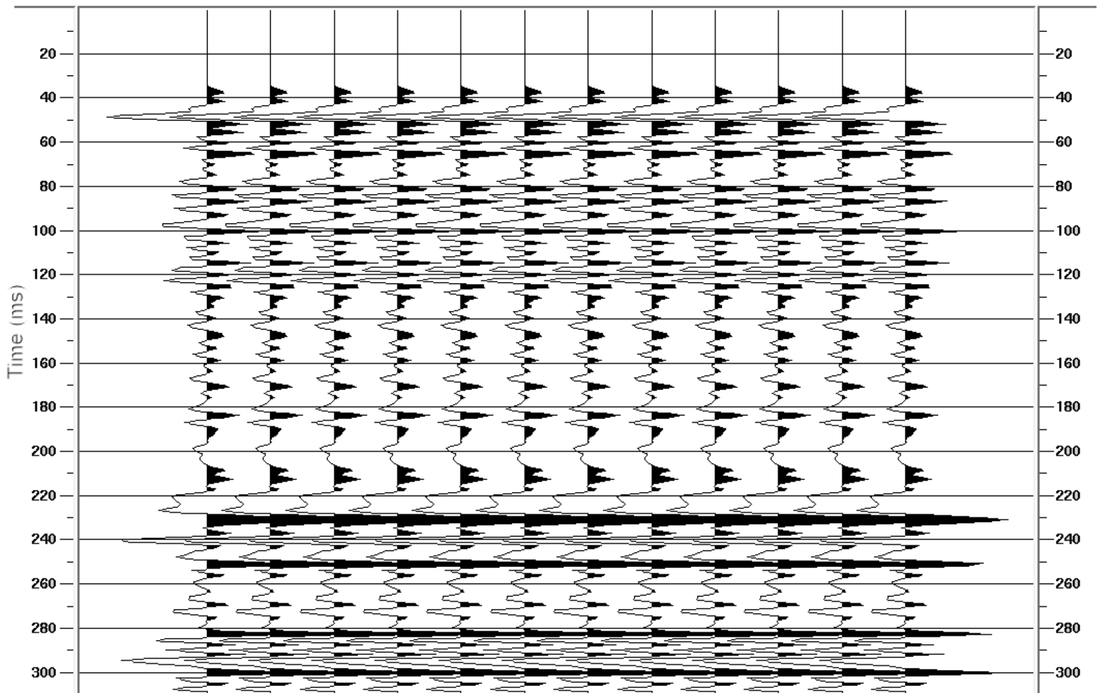

Figure 3.24 Final corridor stack of zero-offset mini-P P-wave VSP data. Coal event is visible at 220 ms (ProMAX VSP).

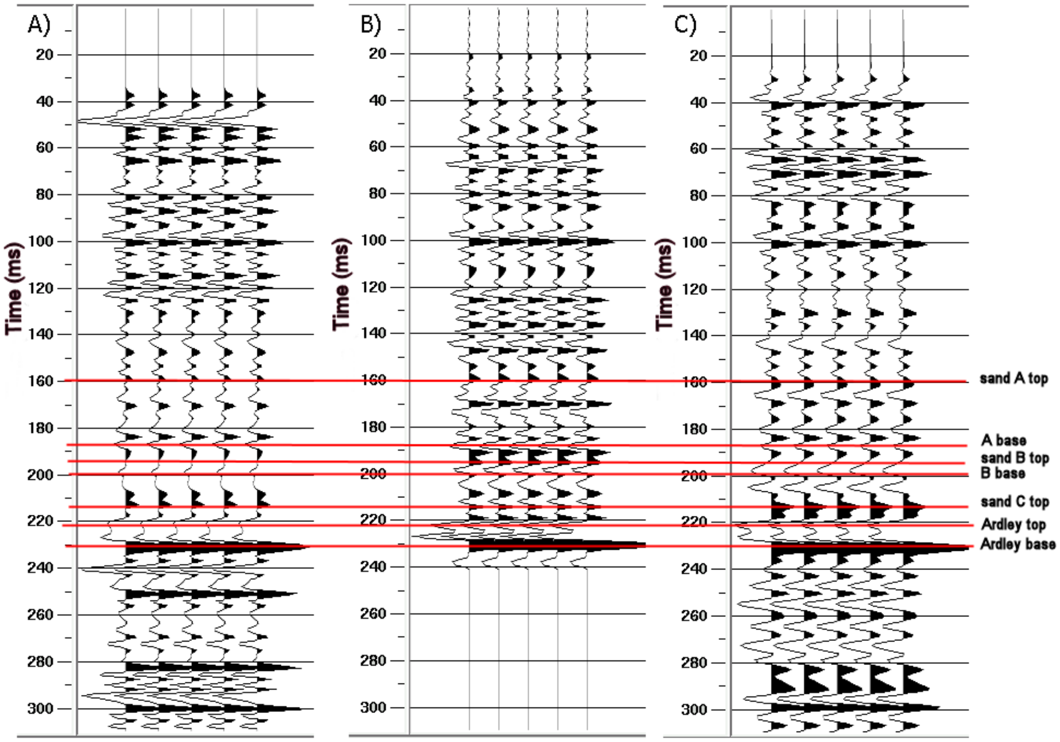

Figure 3.25 Comparison of zero-offset mini-P P-wave corridor stacks produced by A) ProMAX VSP, B) synthetic seismogram with extracted mini-P wavelet, and C) Schlumberger processing. Geological markers are highlighted in red.

Both resultant mini-P data sets show a high-amplitude coal event, with the upper coal contact imaged at approximately 220 ms, and the basal contact at approximately 230 ms. Both processed data sets correlate well with the synthetic seismogram generated by convolution of the well logs with the extracted mini-P wavelet. Processed mini-P data sets are able to resolve not only upper and lower coal contacts, but also an intra-coal event at approximately 225 ms. Although it is possible this is the result of wavelet side-lobe interference, this event is also visible on the synthetic seismogram, and detailed examination of the well logs suggest that this event may represent one of the shale partings or a calcite streak within the coal zone.

3.3.3 Zero-offset big-P processing

Using a flow nearly identical to that used for mini-P processing (Figure 3.11) zero-offset big-P vertical-component data were processed by Schlumberger. Changes were made only to minor parameters within the processing steps, such as the extents of bandpass filters. The final big-P corridor stack is illustrated in Figure 3.26.

A comparison of the final big-P corridor stack to the mini-P corridor stack (Schlumberger version) is illustrated in Figure 3.27.

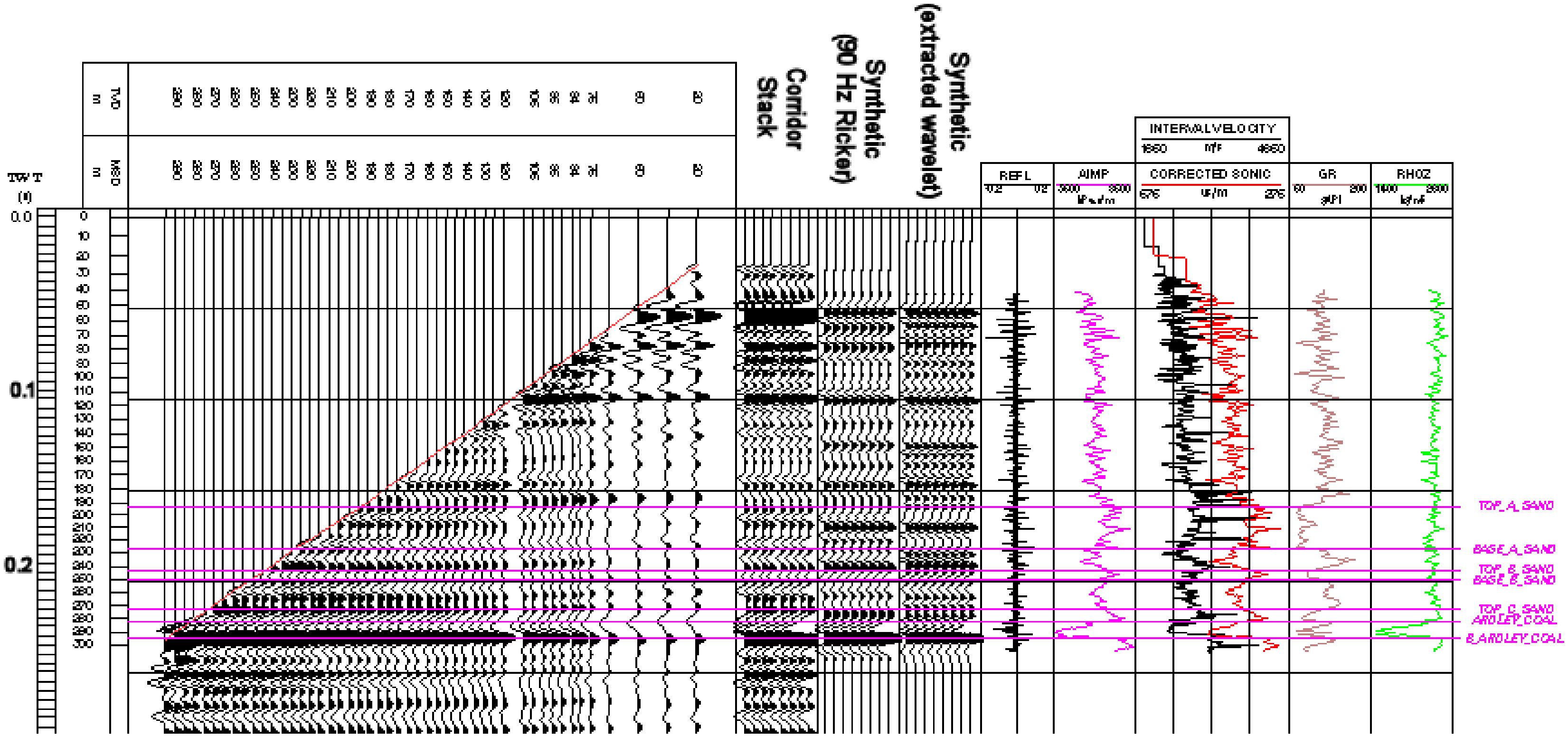

Figure 3.26 Final corridor stack and L-plot of big-P data (Schlumberger).

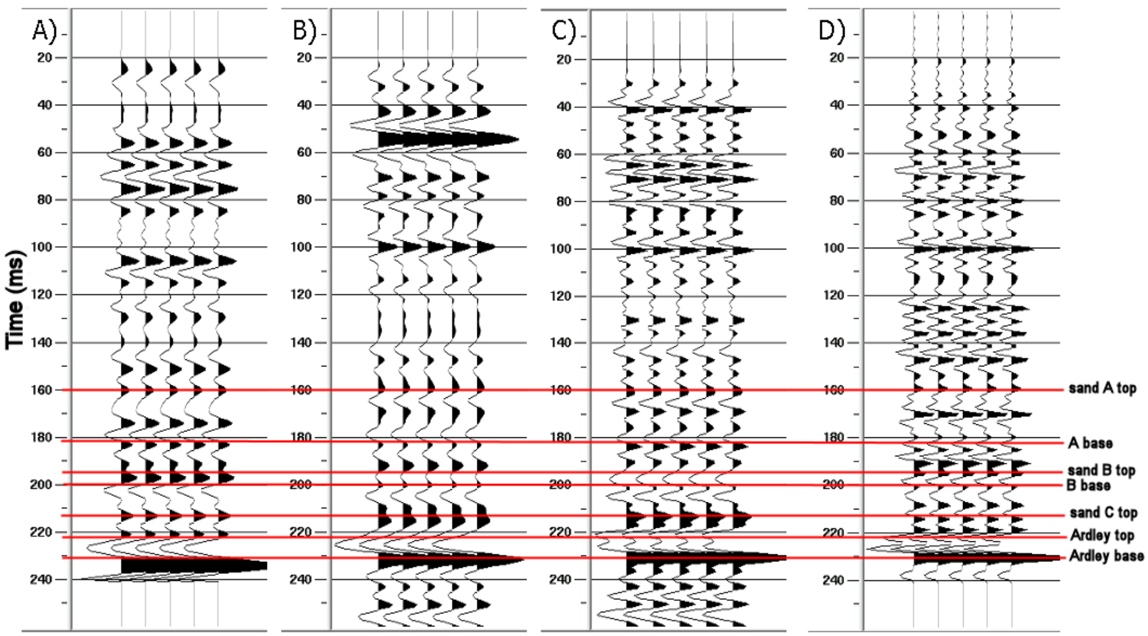

Figure 3.27 Comparison of zero-offset VSP corridor stacks produced from A) synthetic seismogram using well logs and extracted big-P wavelet, B) big P-wave source, C) mini-P wave source, and D) synthetic seismogram convolved with extracted mini-P wavelet. Ardley coal zone response begins at 220 ms, with upper and lower coal contacts highlighted in red. The mini-P response clearly shows an intra-coal event between the upper and lower coal contacts, whereas the big-P data are not able to resolve this event.

Big-P data images the coal zone well, although it is not able to resolve the intra-coal event imaged by the higher-bandwidth mini-P source. This corridor stack shows, however, that a big-P source is suitable for detection of coal seams, but not for detailing intra-seam inhomogeneities.

Amplitude spectra of the final stacks for each source indicate that the mini-P data set has much higher bandwidth than the big-P data, as expected. Frequency analysis for the big-P dataset demonstrates useable frequency content of 15-150 Hz (Figure 3.28), virtually identical bandwidth to the source sweep. Assuming an average coal velocity of 2450 m/s in the study area (from the VSP data), this results in a maximum theoretical possible resolution up to 4.08 m using the traditional $\lambda/4$ formula, or up to 2.04 m using the Gochioco (1992) modified limit of resolution for coal. Little attenuation of the high frequencies has occurred, suggesting that even higher bandwidth would have been attainable, had the sweep not been limited by operating parameters. At the depth of the coal zone, the dominant frequency is approximately 80 Hz, resulting in a practical limit of resolution of 7.6 m (using $\lambda/4$) or 3.8 m using Gochioco's modified limit.

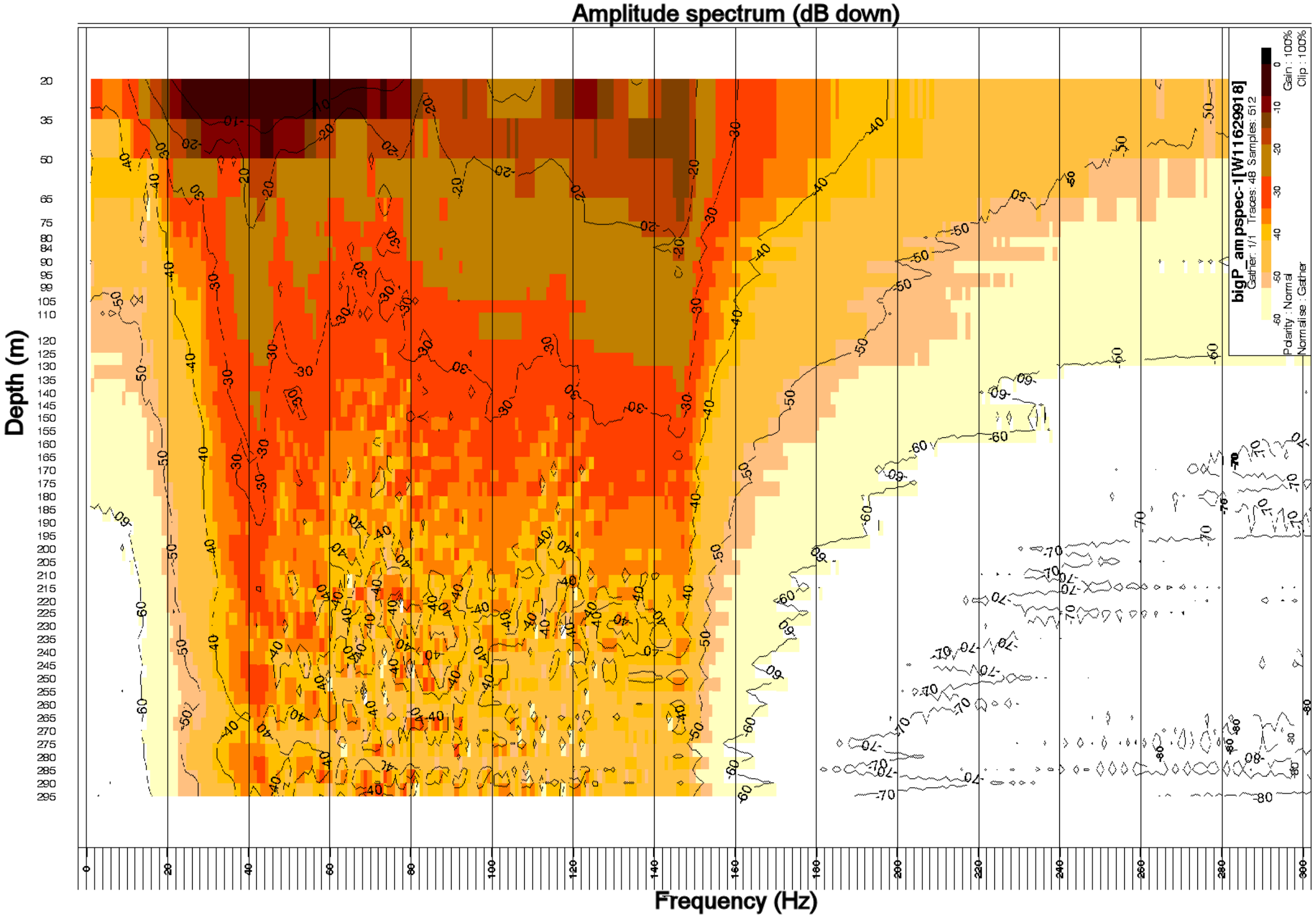

Figure 3.28 Amplitude spectrum for raw big-P zero-offset VSP data. Useable bandwidth ranges from 15-150 Hz, with little attenuation of high frequencies, even at depth (Schlumberger).

Higher bandwidth was obtained in the mini-P survey, with useable frequencies ranging from 15-220 Hz (Figure 3.29). With an input sweep of 8-250 Hz, only the very lowest and highest frequencies have been attenuated. Dominant frequency at the depth of the coal is approximately 110 Hz. This results in a practical resolution as high as 5.6 m (using $\lambda/4$) or 2.8 m (using $\lambda/8$). The final corridor stacks clearly demonstrate the improved resolution of the mini-P data set, which is able to image an intra-coal event. Log data shows the largest impedance contrasts within the coal zone bound a layer only 0.5 m thick. The high bandwidth recorded suggests that strong impedance contrasts within a coal zone may allow detailed mapping of individual seams within a coal zone, or locating undesirable tight streaks prior to CBM development.

In both big-P and mini-P amplitude spectra, frequencies above the input sweep are detected at shallow depths. These high frequencies may be the result of mechanical noise from the vibrators, or may be the result of harmonics.

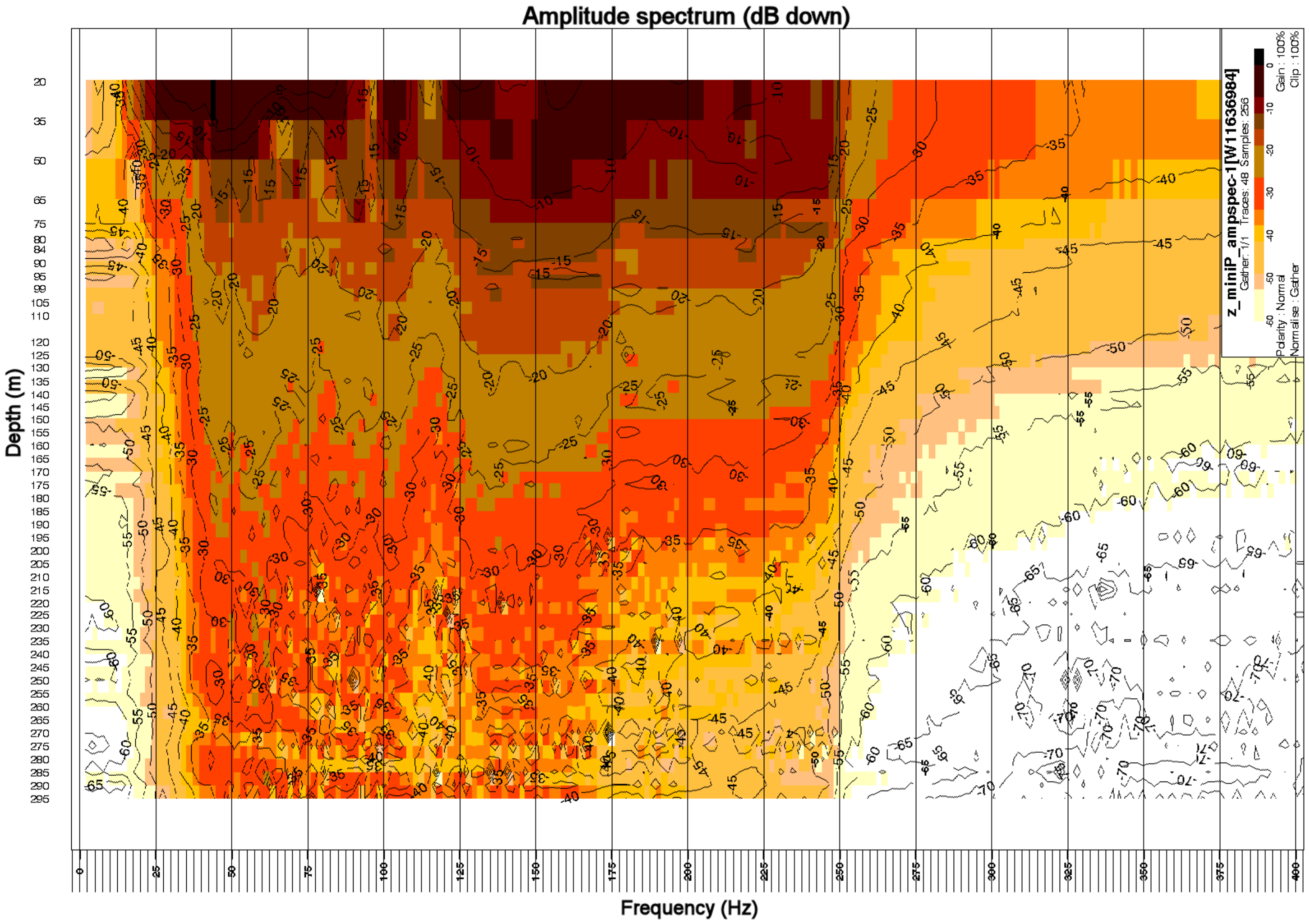

Figure 3.29 Amplitude spectrum of raw zero-offset mini-P VSP data. Useable bandwidth ranges from 8-220 Hz (Schlumberger).

Comparing bandwidth and resolution of the two data sets, it can be concluded that in this study area, a mini-P source is preferable for imaging of the Ardley coal zone. The resolution attainable in mini-P data is superior to that of the big-P source, and attenuation of the signal has occurred only at the highest frequencies. A big-P source, however, is suitable for coal detection, as it has effectively imaged both the upper and lower contacts of the Ardley coal zone.

3.2.3 Zero-offset mini-S processing

Schlumberger's processing flow for the mini-S data set is outlined in Figure 3.30.

Horizontal components were rotated into the plane of the source and receivers. The horizontal component showing maximum energy was selected for processing. After picking first breaks, true amplitude recovery and amplitude normalization were applied. Shear wavefield separation was accomplished using a fifteen-trace median filter, and the resultant upgoing energy was enhanced using a nine-trace median filter. Waveshaping bottom level deconvolution removed the effects of the input source energy, and the deconvolved traces were once again enhanced with a median filter. No shear sonic log was recorded prior to processing the mini-S zero-offset data, so a model was built using the compressional-sonic log and the mini-S first arrival times to convert the data to P-time.

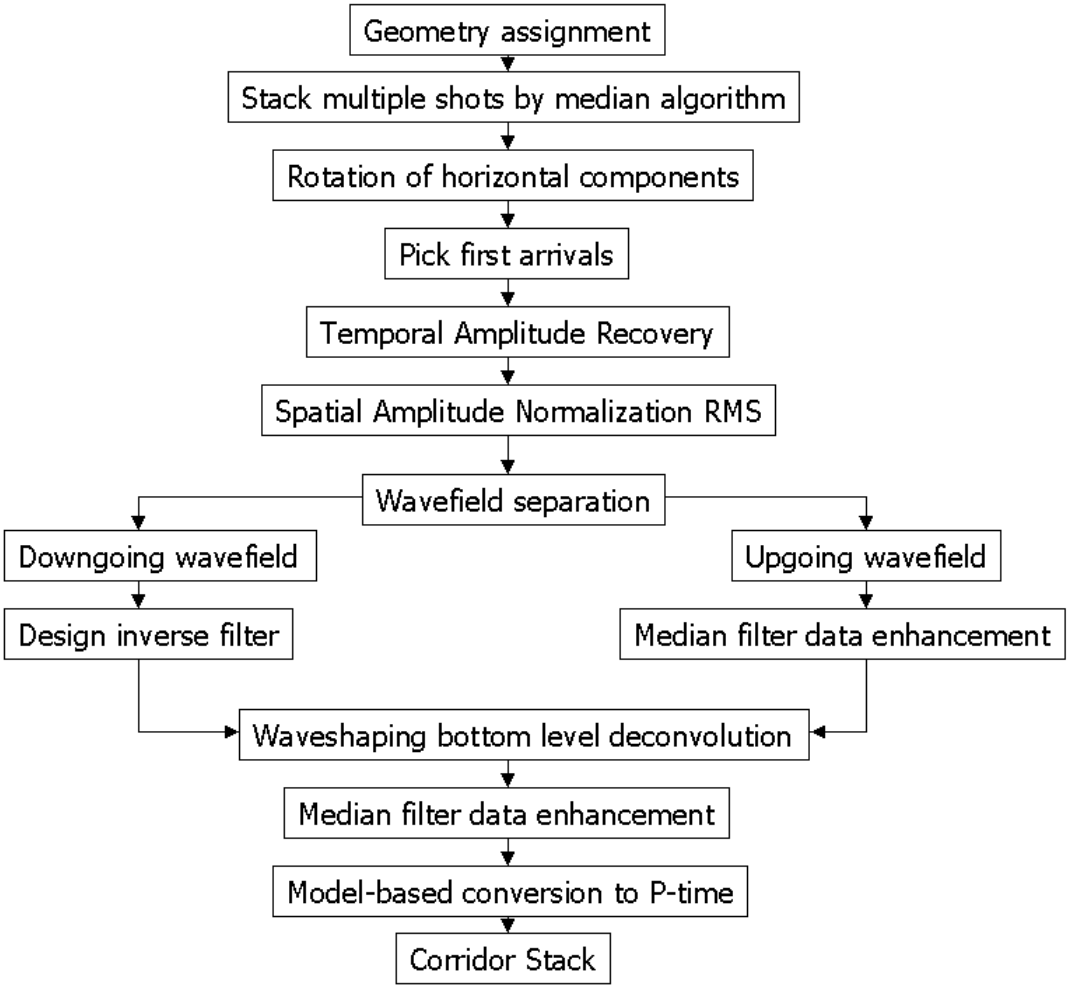

Figure 3.30 Outline of processing flow used by Schlumberger to process the zero-offset mini-S VSP data.

The final corridor stack of mini-S data is illustrated in Figure 3.31, whereas Figure 3.32 shows a comparison to the mini-P corridor stack. An apparent phase shift is noted when comparing the two data sets, as the mini-S coal top response is a zero crossing, whereas the P-data coal top response is a trough. This is attributed to a difference in tuning between the two wavefields.

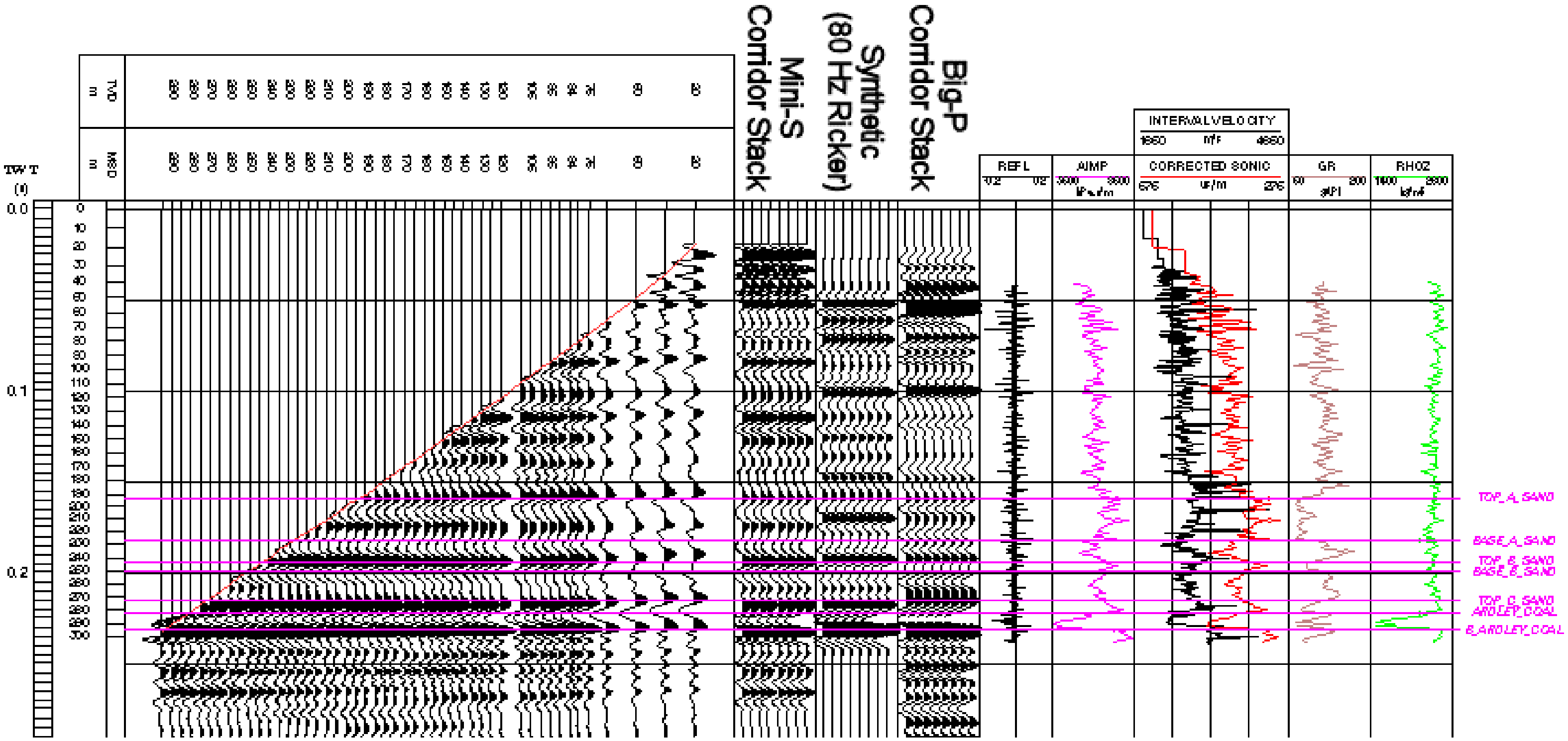

Figure 3.31 Final corridor stack and L-plot of mini-S data (Schlumberger).

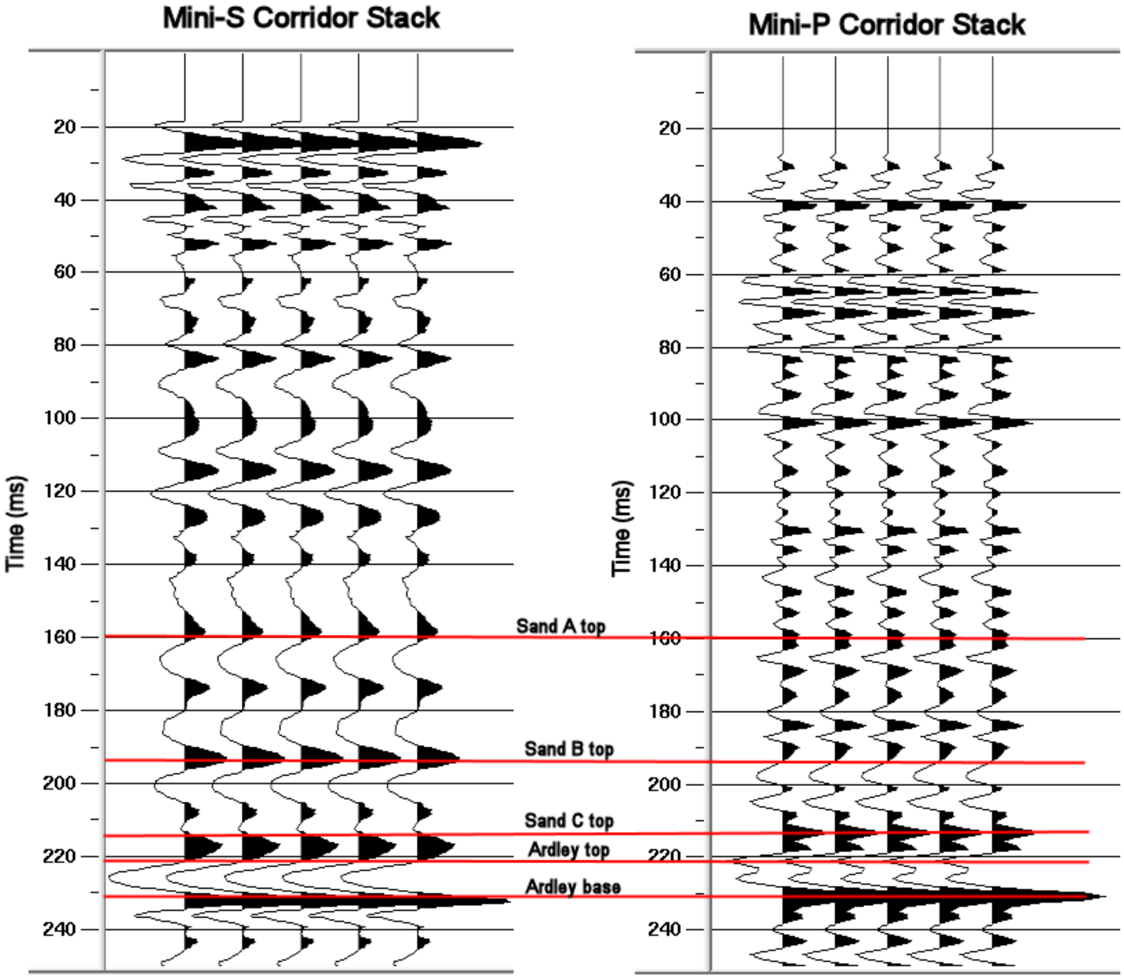

Figure 3.32 Comparison of mini-S and mini-P corridor stacks (in P-time). Upper coal response is highlighted in red. The mini-S coal response is a zero crossing, whereas the mini-P response is a trough.

Upper and lower coal contacts both produce strong amplitude reflections recorded on the horizontal component of the mini-S VSP data. In the compressional-wave data sets, the seismic response of the upper contact of the coal is a trough, and a slight phase difference is noted between the P and S data sets. The amplitude spectrum of the mini-S data shows useable frequencies of 15-80 Hz (Figure 3.33), with a dominant frequency of approximately 30 Hz, meaning the input sweep of 8-150 Hz has been considerably attenuated. Using average S-velocities of 1010 m/s in the study area, the calculated limit of resolution is approximately 8.4 m, using λ/4 or 4.2 m, using the λ/8 criterion.

The attenuation of shear waves relative to P-waves is considerably higher. Whereas P-wave data retained a high proportion of the bandwidth of the original sweep, exponential decay is noted in the S-wave data (Figure 3.33). Limits of resolution at the level of the coal are similar for mini-S and big-P data sets, with inherent shorter wavelengths compromised by lower frequencies.

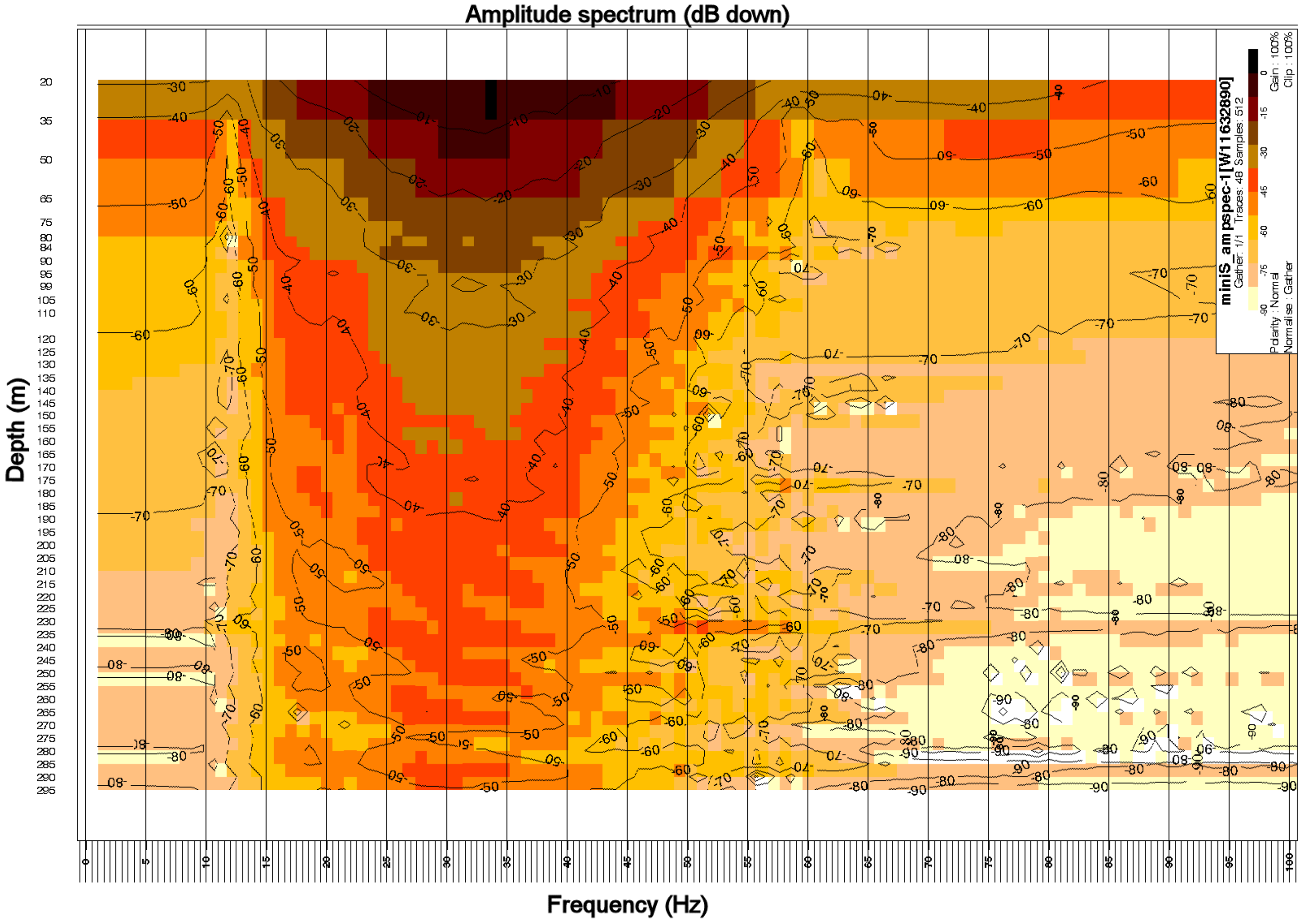

Figure 3.33 Amplitude spectrum of raw zero-offset mini-S VSP data. Useable bandwidth ranges from 8-50 Hz (Schlumberger).

3.4 Discussion

Source tests illustrate that in this area, a mini P-wave truck-mounted vertical vibrator source unit is an ideal source for imaging coal seams at a depth of approximately 300 m, yielding much higher resolution data than a conventional heavy-duty vertical vibrating source. Ardley coal zone contacts at the Red Deer site may be effectively imaged using any of the three sources tested, but lithological changes within the coal may be detected using the high-frequency mini-P source.

Bandwidth comparisons show useable frequencies of 8-150 Hz in big-P data, whereas mini-P data contains frequencies ranging 8-220 Hz. Shear wave attenuation was considerably higher than that of P-waves, with the mini-S source yielding useable bandwidth of 8-50 Hz. Such low attenuation of the mini-P source suggests that high-bandwidth converted-wave data may be obtained using the mini-P source.

Using extracted amplitude spectra combined with seismic and sonic well log traveltimes, the attenuation for P-waves (Q_p) of the Cygnet strata may be estimated. This is calculated using the equation:

$$t_{delay} = \frac{d \ln(\omega_2 / \omega_1)}{\pi Q_p V(\omega_2)} \qquad \text{(Stewart et al., 1984)}$$

where t_{delay} is the delay time between sonic log and seismic traveltimes, d is the distance traveled, Q_p is the attenuation, $V(\omega_2)$ is the sonic velocity, and ω_1 is the seismic center frequency.

For the mini-P vibrating source to the base of the wellbore, Q_p is estimated to be 31.4. The parameters used for this estimate are: t_{delay}=0.00622 s; d=300 m; $V(\omega_2)$=2545 m/s; ω_1=20000 Hz; and ω_2=110 Hz.

Attenuation of shear waves (Q_s) can be determined in the same fashion, using the appropriate shear velocity and shear-wave frequencies. To the base of the Red Deer wellbore using the mini-S vibrating source, Q_s is estimated to be 9.7. The parameters used for this estimate are: t_{delay}=0.07006 s; d=300 m; $V(\omega_2)$=915 m/s; ω_1=20000 Hz; and ω_2=30 Hz.

Examination of the Vp/Vs character of the shallow strata demonstrated a profile similar to those seen in other parts of Alberta and the world. Vp/Vs values were high (nearly 5.0) in the near-surface, decreasing with depth to a Vp/Vs of approximately 2.0. Good correlation was noted between Red Deer Vp/Vs values calculated using the zero-offset VSP data and those calculated using cased hole sonic logs. This suggests that either well log or seismic data may be used to extract velocities used in numerical modelling.

Chapter 4 Imaging and Reflectivity

4.1 Walkaway VSP Processing

Walkaway data were recorded using both the big-P and mini-P sources. Using a flow very similar to that used for zero-offset data, processing of the mini-P walkaway data was completed by Schlumberger. Geometry was assigned, vertical and horizontal components were separated, horizontal components were rotated into the source-receiver plane, and the in-line component then used for P-S imaging and analysis. After picking first breaks, temporal amplitude recovery with a time-power constant of 1.7 and spatial amplitude normalization RMS (with a time-window of 0.1 s) were applied. Total wavefield separation was accomplished using parametric decomposition (10-150 Hz frequency range, 0.02-1.0 s time window). This flow is outlined in Figure 4.1. Schlumberger provided SEG-Y data of the downgoing P-wavefield (Figure 4.2), upgoing P-wavefield (Figure 4.3), and both downgoing and upgoing S-wavefields (Figure 4.4, and Figure 4.5 respectively). All raw wavefields have had a bulk shift applied for simplicity of plotting.

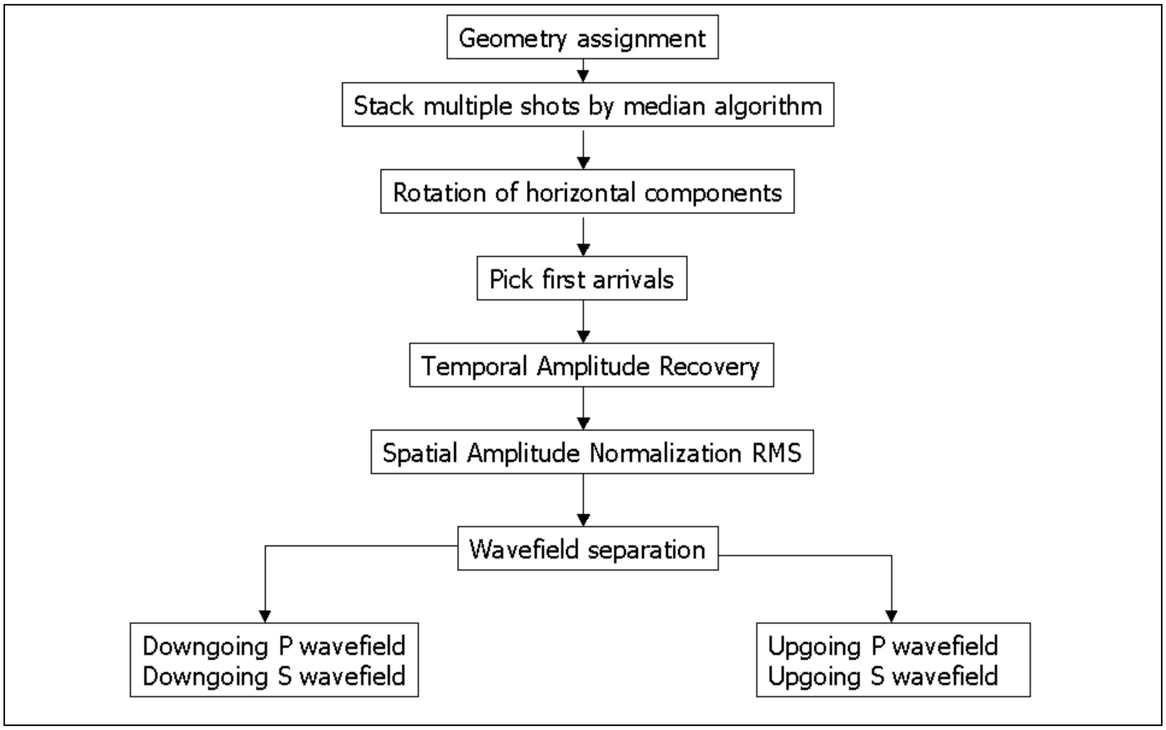

Figure 4.1 Outline of processing flow employed by Schlumberger in processing of multi-offset VSP data.

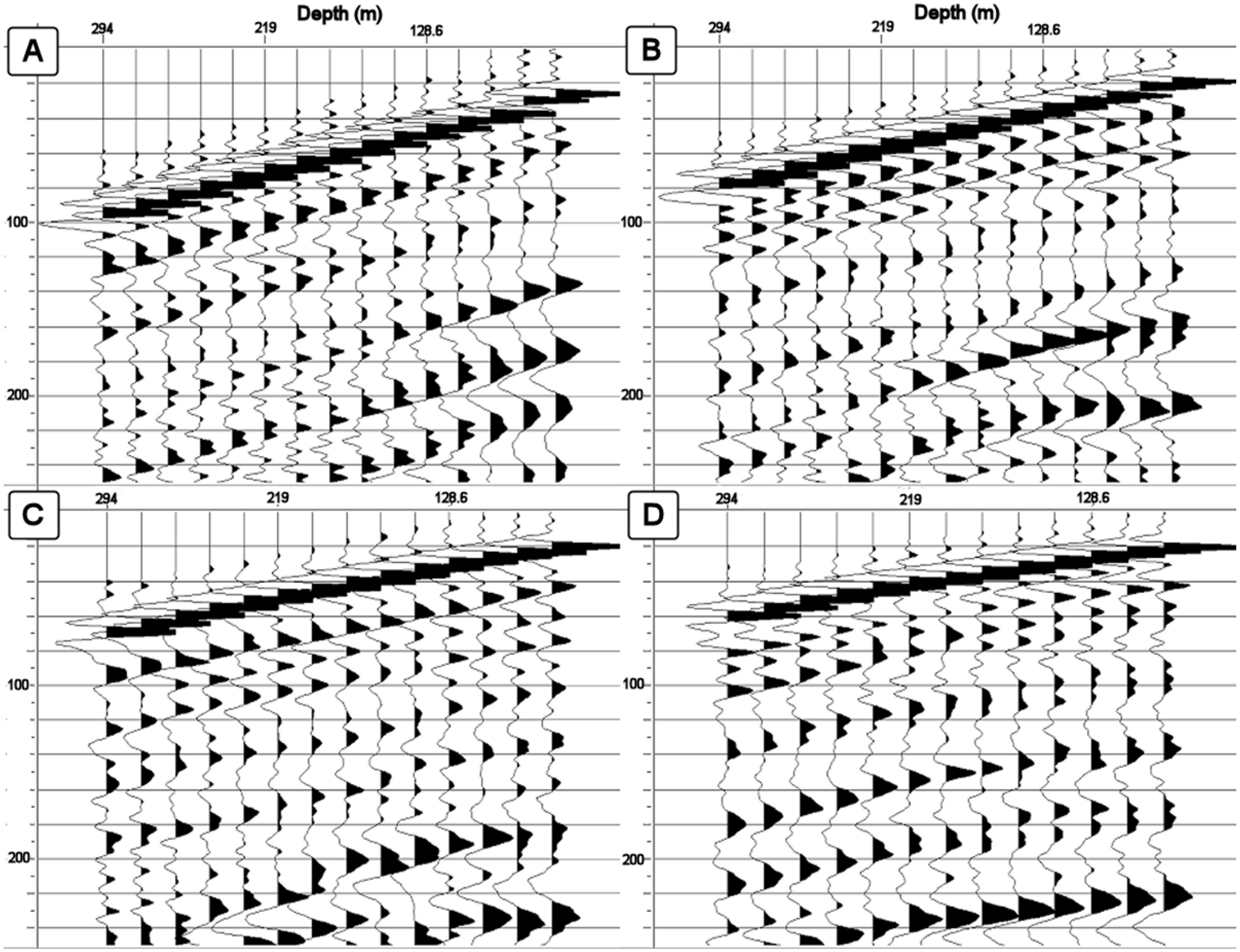

Figure 4.2 Downgoing P-wavefields for source offsets of: A) 100 m, B) 150 m, C) 191 m, D) 244 m. Receivers are ordered from deepest to shallowest (left to right). All time scales are in milliseconds.

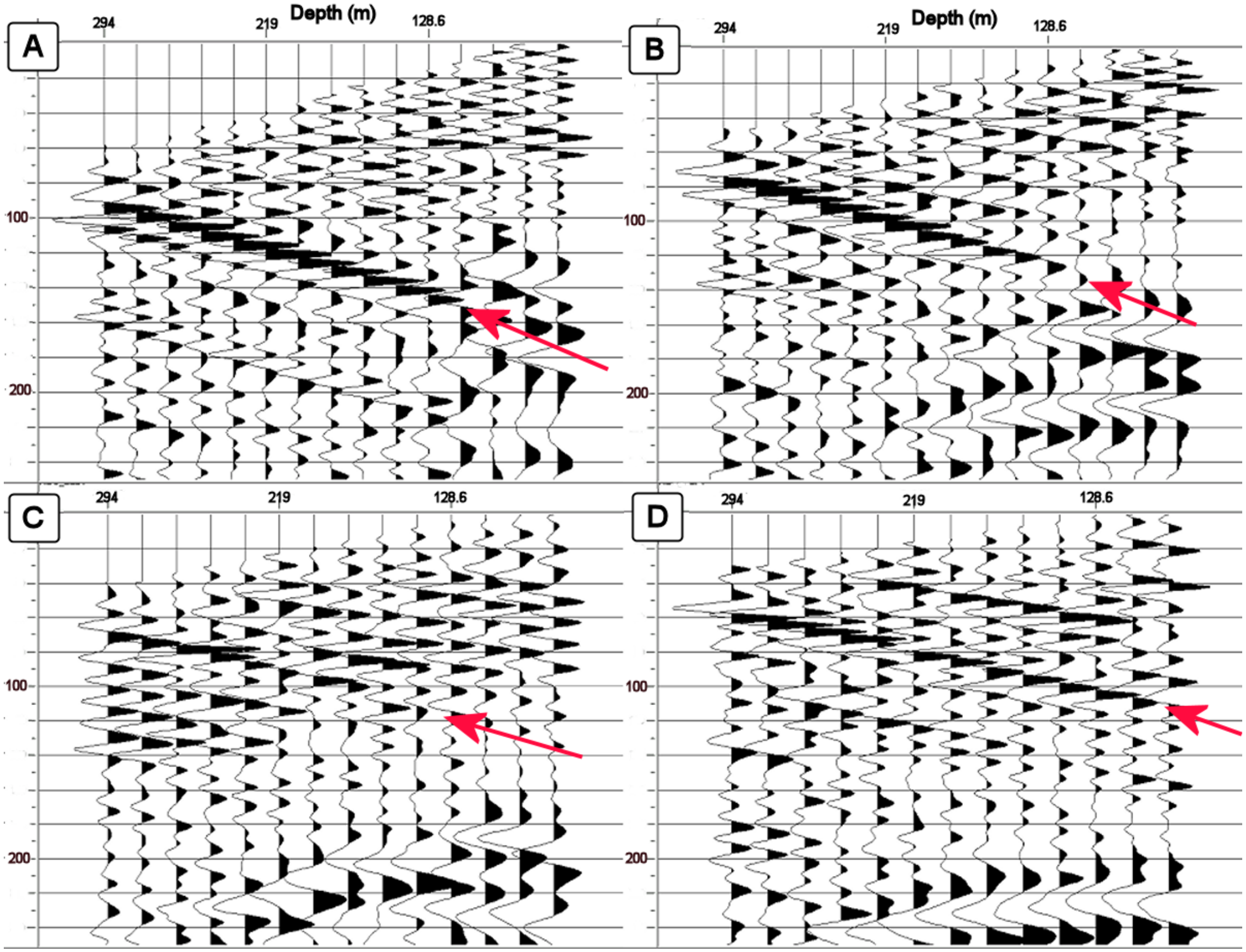

Figure 4.3 Upgoing P-wavefields for source offsets of: A) 100 m, B) 150 m, C) 191 m, D) 244 m. Receivers are ordered from deepest to shallowest (left to right). Upgoing energy is indicated with an arrow.

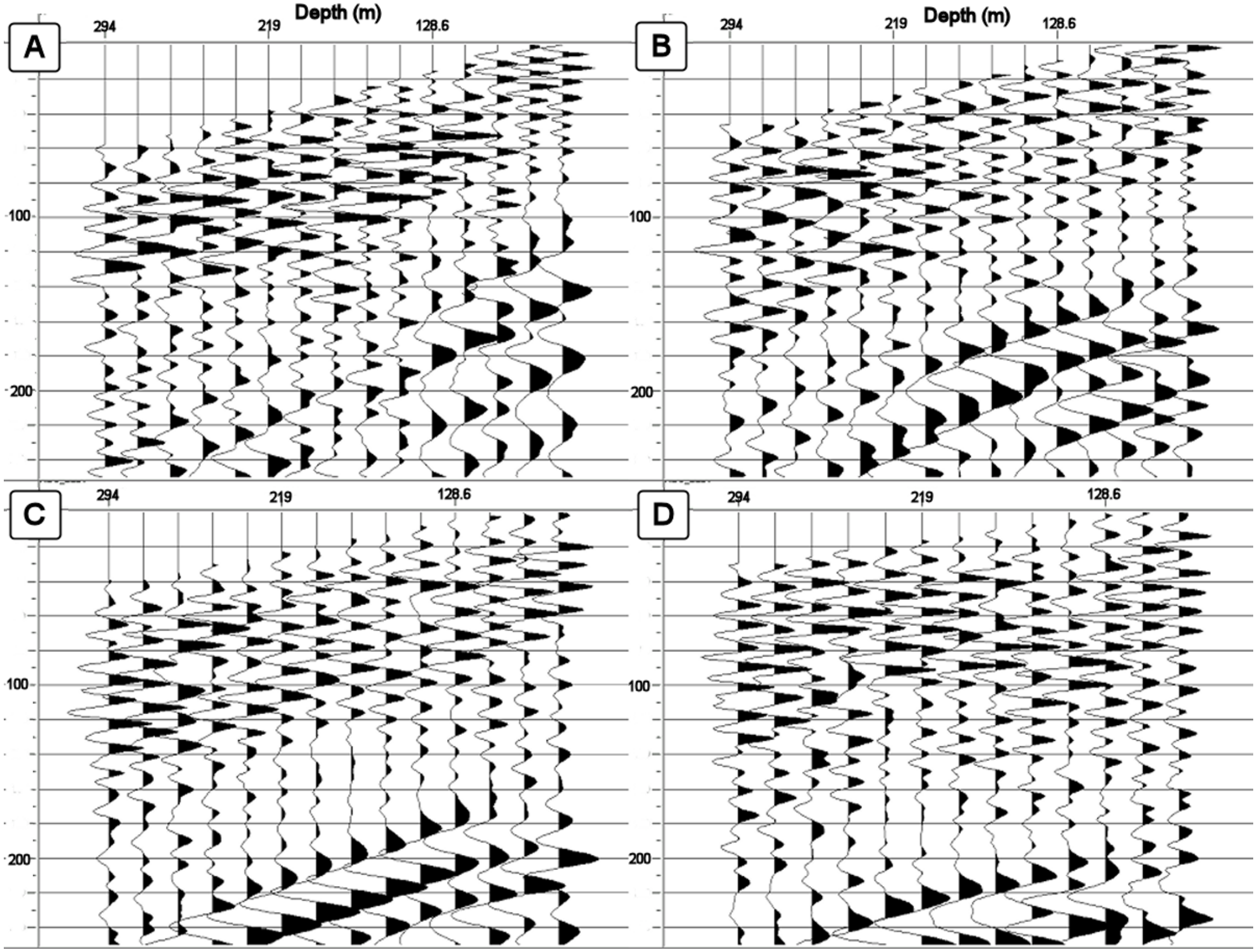

Figure 4.4 Downgoing S-wavefields for source offsets of: A) 100 m, B) 150 m, C) 191 m, D) 244 m. Receivers are ordered from deepest to shallowest (left to right).

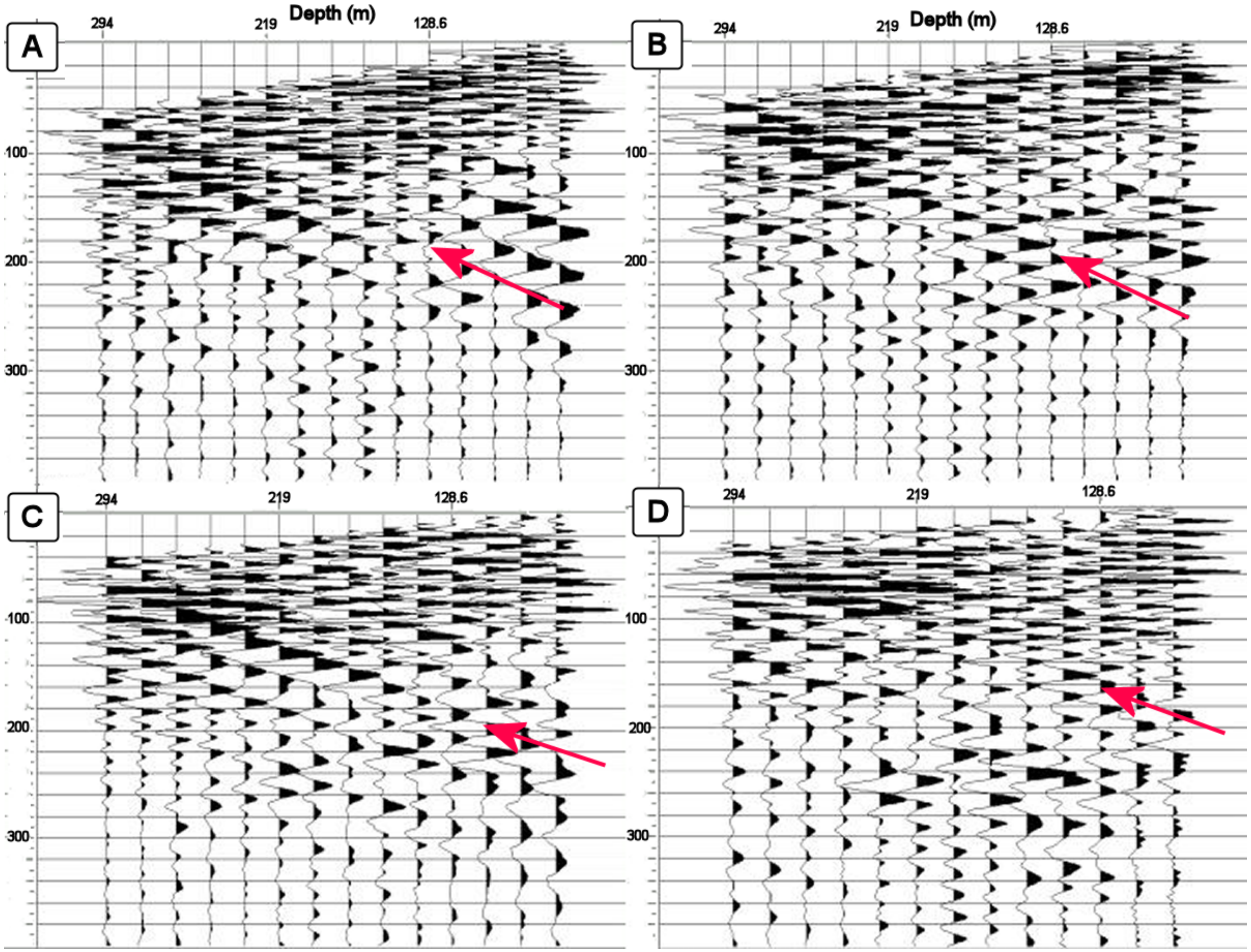

Figure 4.5 Upgoing S-wavefields for source offsets of: A) 100 m, B) 150 m, C) 191 m, D) 244 m. Receivers are ordered from deepest to shallowest (left to right). Upgoing energy is highlighted with an arrow.

These separated wavefields were further processed to produce a final VSP-CDP stack for P-P data and a VSP-CCP stack for P-S reflections. Schlumberger’s flows to produce these final sections are outlined in Figure 4.6.

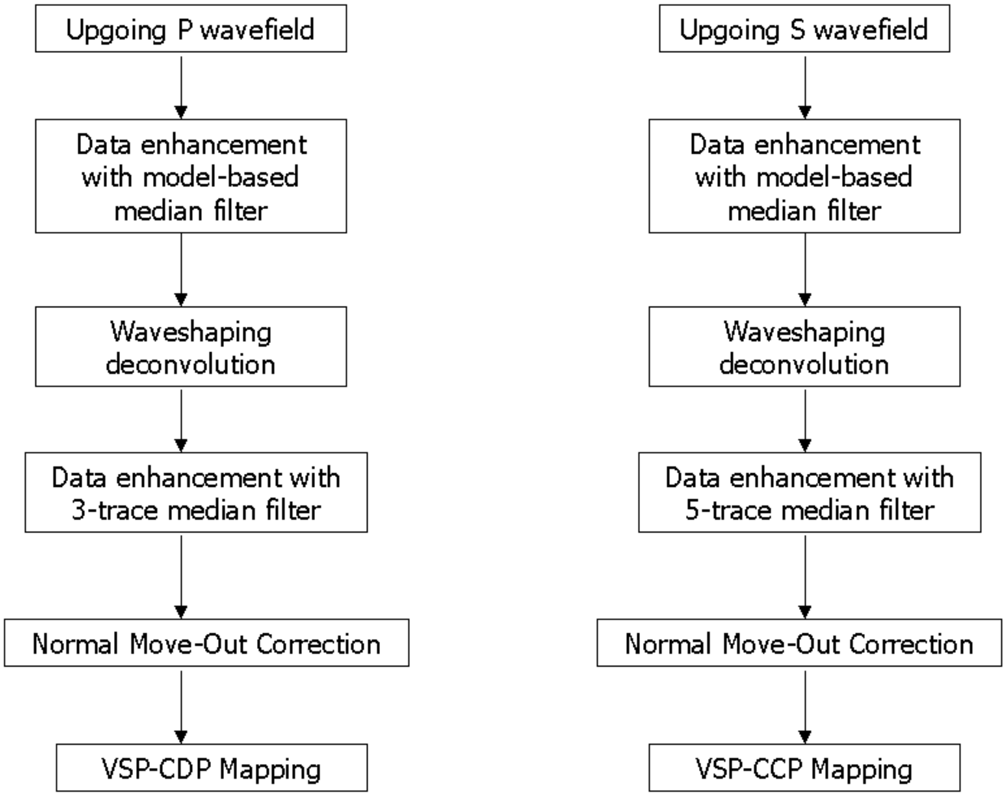

Figure 4.6 Processing flow used to create VSP-CDP transform of P-P walkaway data, and VSP-CCP mapping of P-S walkaway data (Schlumberger).

Separated wavefields were enhanced using a model-based median filter of 5 traces length. Trace by trace waveshaping deconvolution was applied using a 0.15 s window, 10-150 Hz spectrum, and 0.1% noise. A second median filter was applied to the deconvolved data, using 3 traces to enhance the P-wave data, and 5 traces to enhance the S-wave data. The wider filter was used to better enhance the noisier shear-wave data set. A normal move-out correction was applied to both compressional and converted-wave data sets. Finally, the VSP-

CDP and VSP-CCP mapping was performed using 2 m binning/mapping intervals, resulting in one set of images for each shot point. Imaging at offsets 1 through 4 is illustrated in Figure 4.7 through Figure 4.10, respectively.

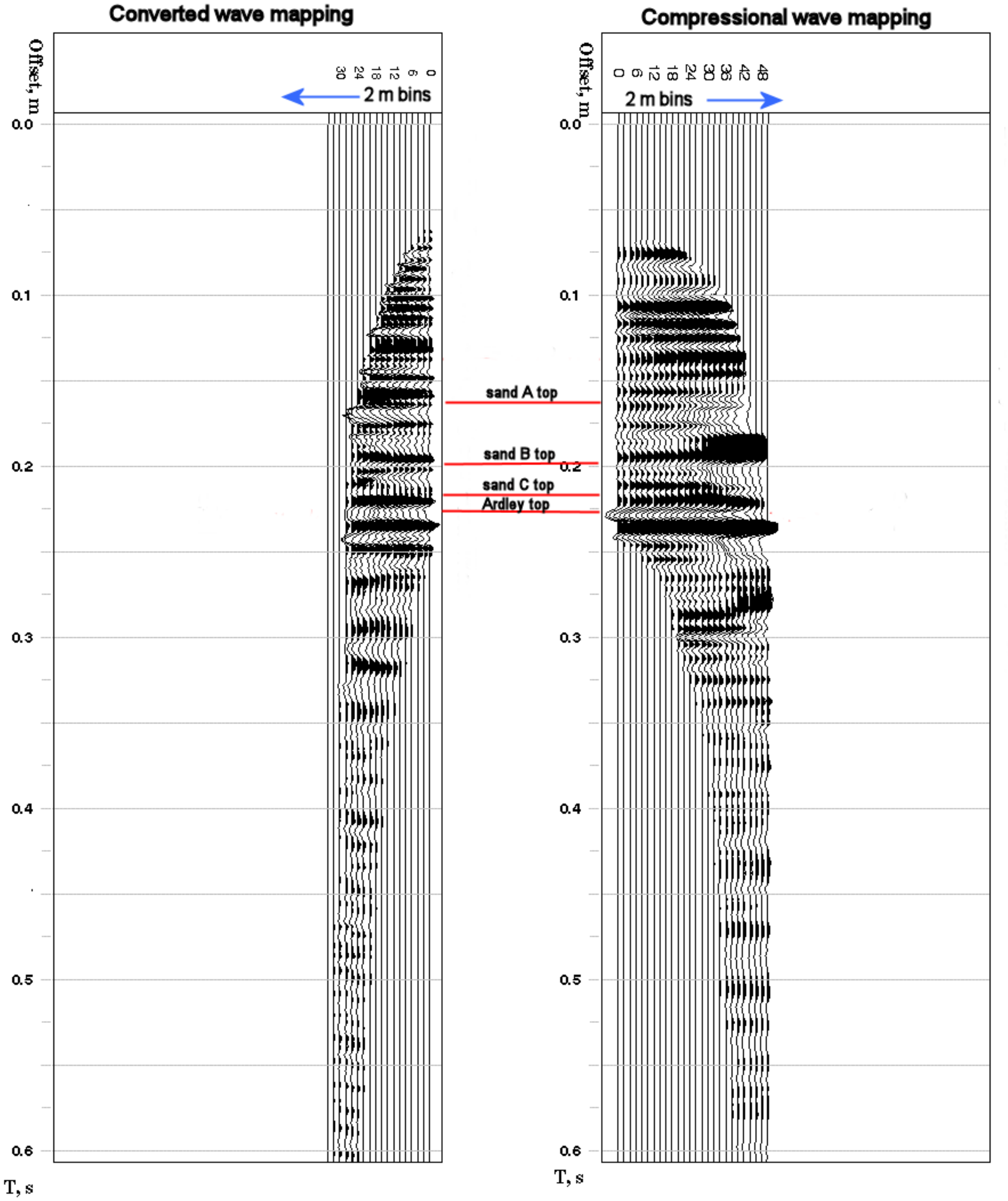

Figure 4.7 Walkaway VSP imaging for shot point #1, located 100 m from the wellbore. VSP-CCP transform is plotted in P-time for ease of comparison (Schlumberger).

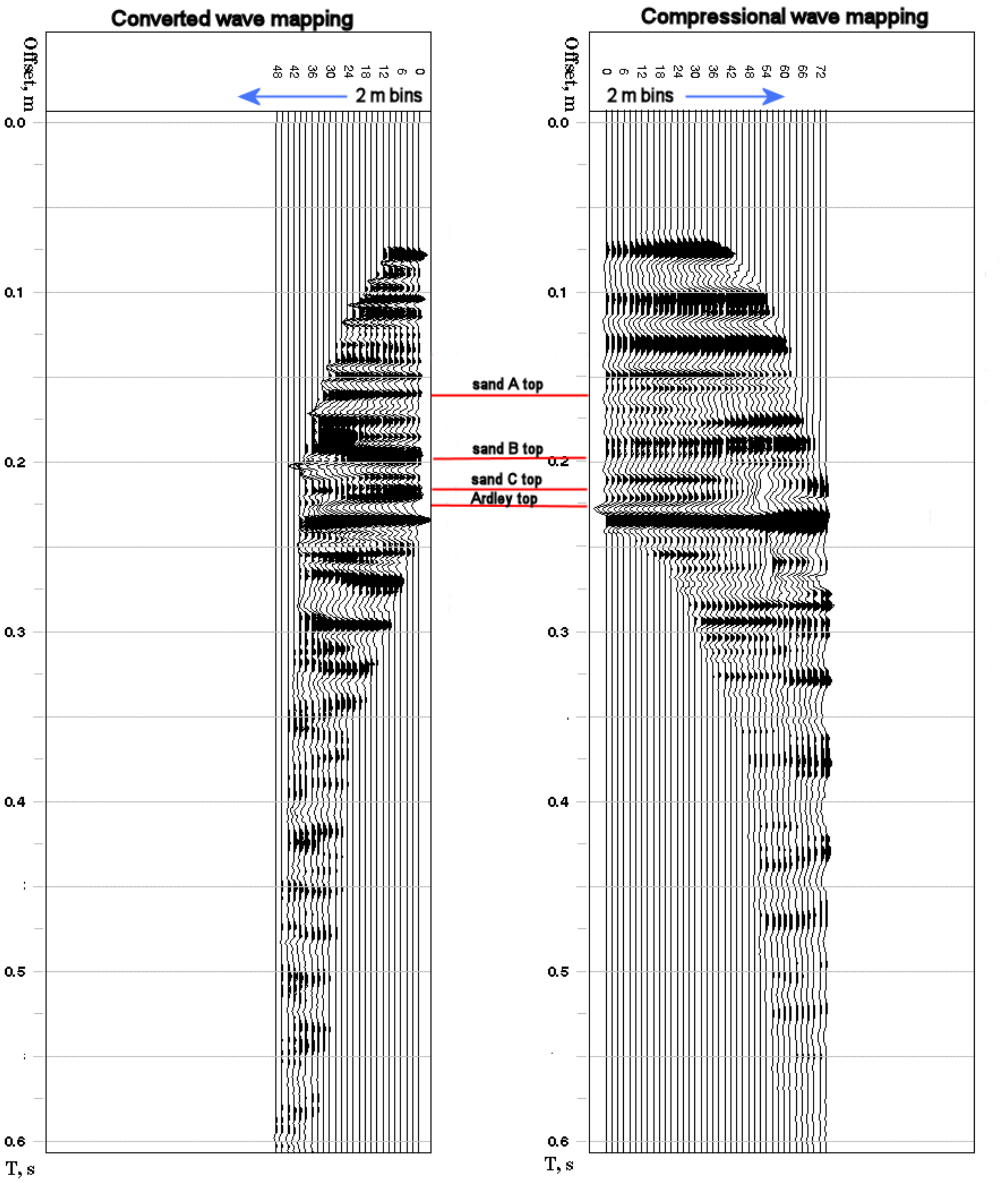

Figure 4.8 Walkaway VSP imaging for shot point #2, located 150 m from the wellbore. VSP-CCP transform is plotted in P-time for ease of comparison (Schlumberger).

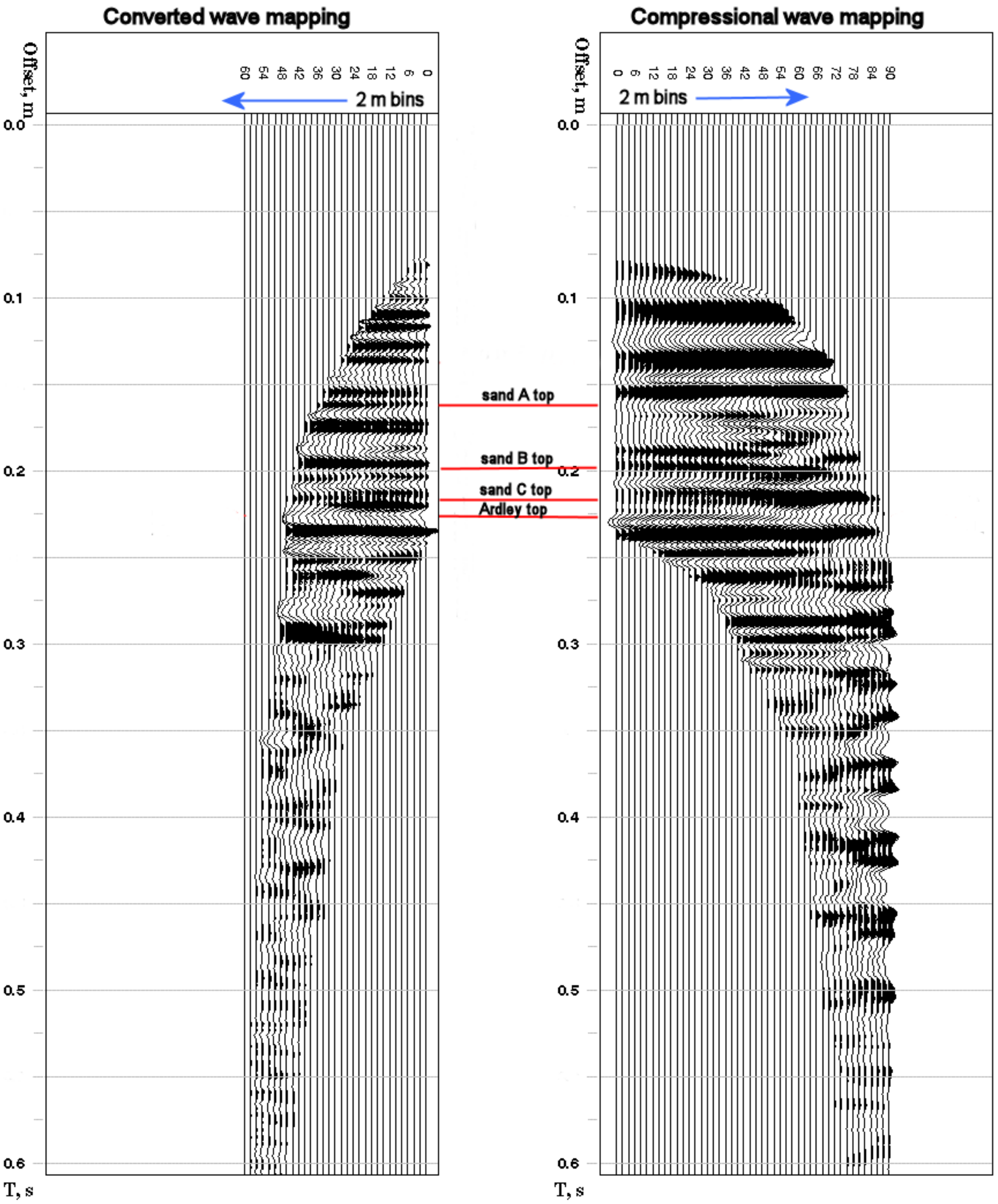

Figure 4.9 Walkaway VSP imaging for shot point #3, located 191 m from the wellbore. VSP-CCP transform is plotted in P-time for ease of comparison (Schlumberger).

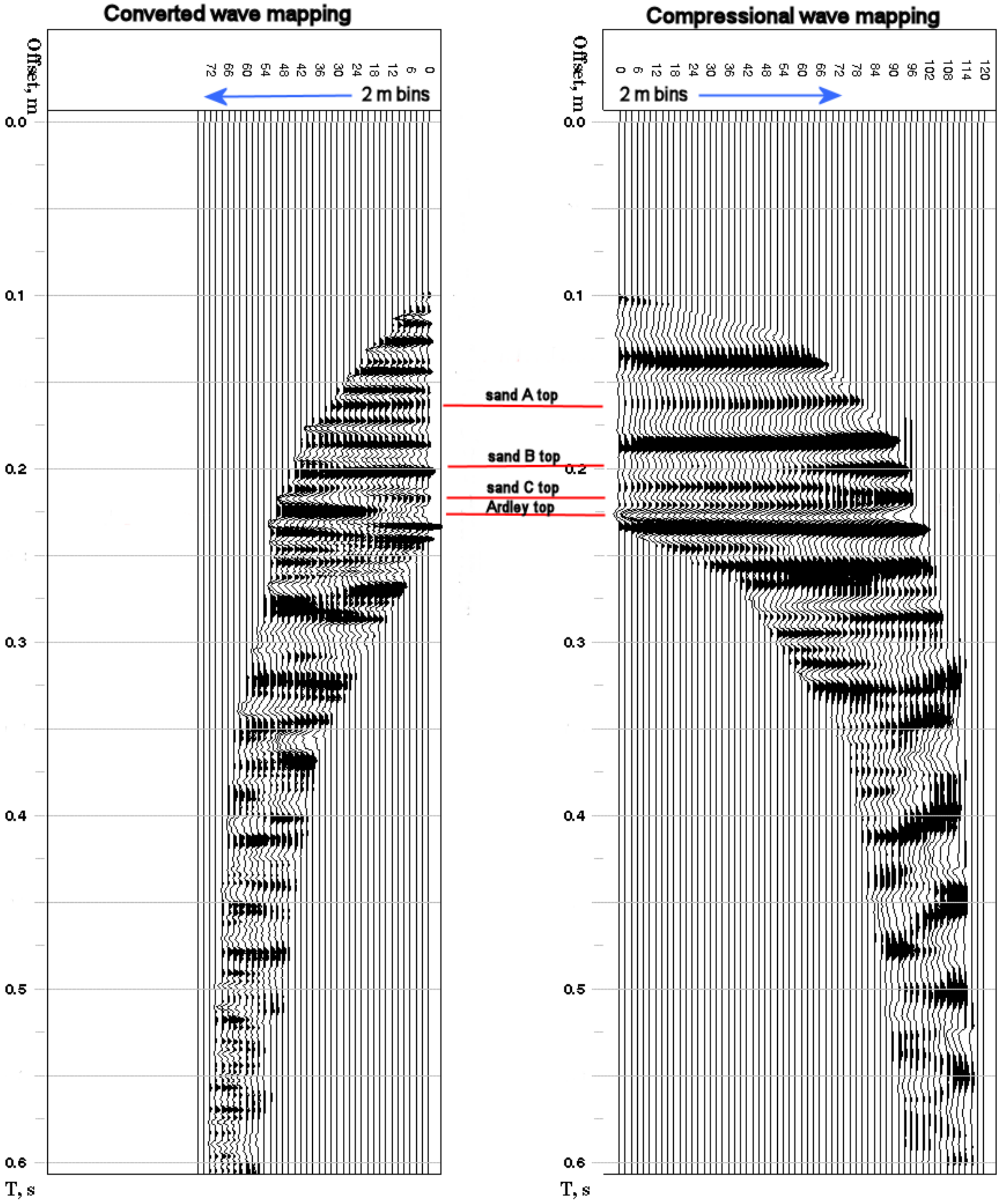

Figure 4.10 Walkaway VSP imaging of shot point #4, located 244 m from the wellbore. VSP-CCP transform is plotted in P-time for ease of comparison (Schlumberger).

Both CDP and CCP mapping show good correlation with the zero-offset corridor stacks and with synthetic seismograms (Figure 4.11 and Figure 4.12). Events are aligned in time, and relative amplitudes are similar throughout the sections.

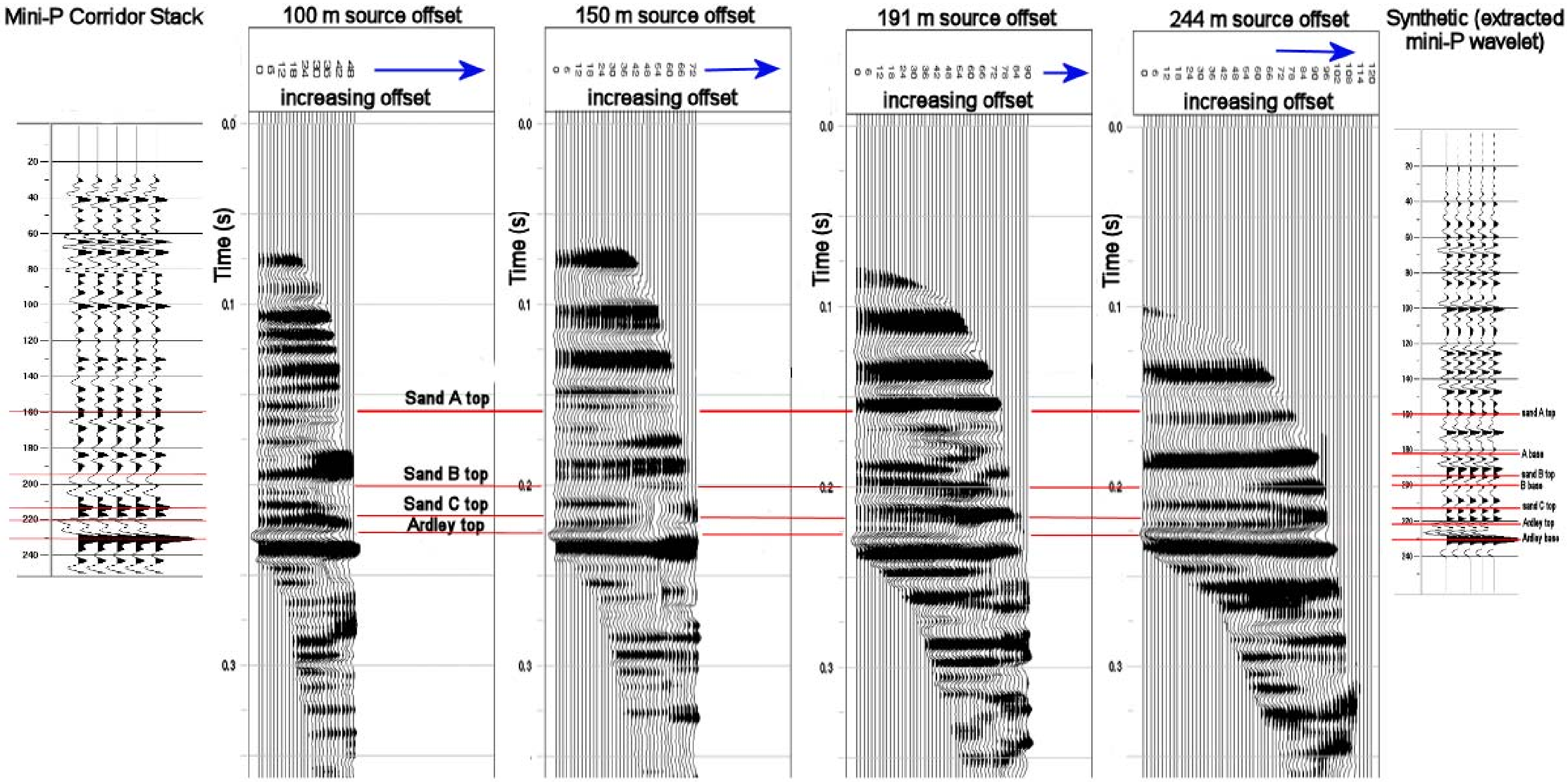

Figure 4.11 Comparison of VSP-CDP mapping with mini-P zero-offset corridor stack and synthetic seismogram created by convolution with extracted mini-P wavelet. All events correlate well, although higher bandwidth is evident in the zero-offset corridor stack.

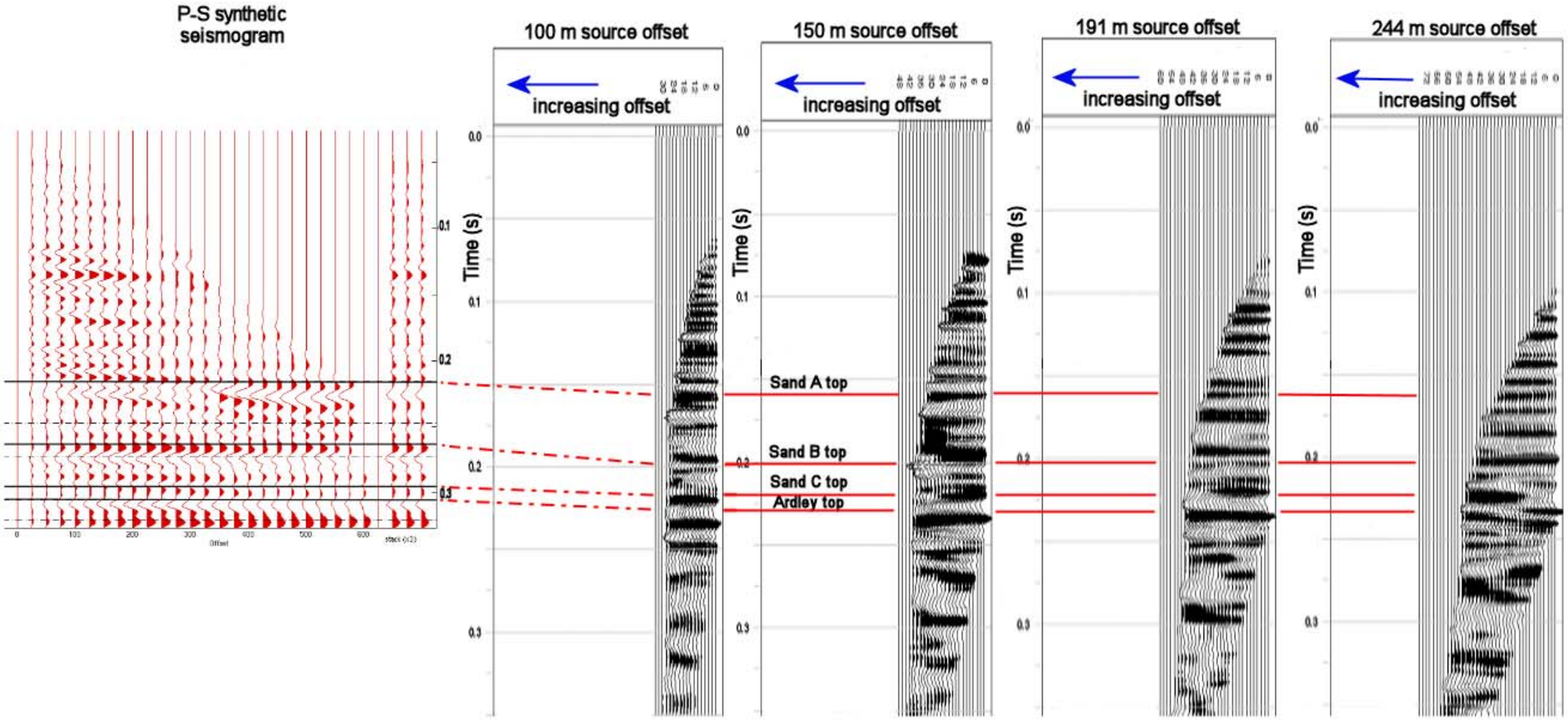

Figure 4.12 Comparison of VSP-CCP transform with P-S synthetic seismogram. VSP-CCP gathers are plotted in P-time, with the synthetic seismogram graphically plotted to match, not transformed to P-P time.

Coal contacts are clearly resolved across the section in both the compressional and converted-wave data. VSP-CDP mapping correlates well with zero-offset data, demonstrating slightly lower bandwidth. At the nearest offset (100 m), the converted-wave data shows even more detail at the coal top, showing a double-trough event, whereas the P-P data shows a single trough representing the coal top. At the furthest offset (244 m), the compressional data gives a more continuous coal response than the converted wave imaging. At the level of the coal top, the VSP-CCP gather at 244 m source offset shows an apparent phase change. Without another source offset, it is not possible to tell whether this is a processing artifact or a legitimate phase change, and it requires further investigation.

4.2 Surface seismic data

Processing of the surface seismic data proved to be limited as a result of the unusual acquisition geometry (Figure 2.3). A simple processing flow was applied to the raw shot records using ProMAX 2D, however, such that coal reflections may be assessed on surface seismic data. This flow is outlined in Figure 4.13.

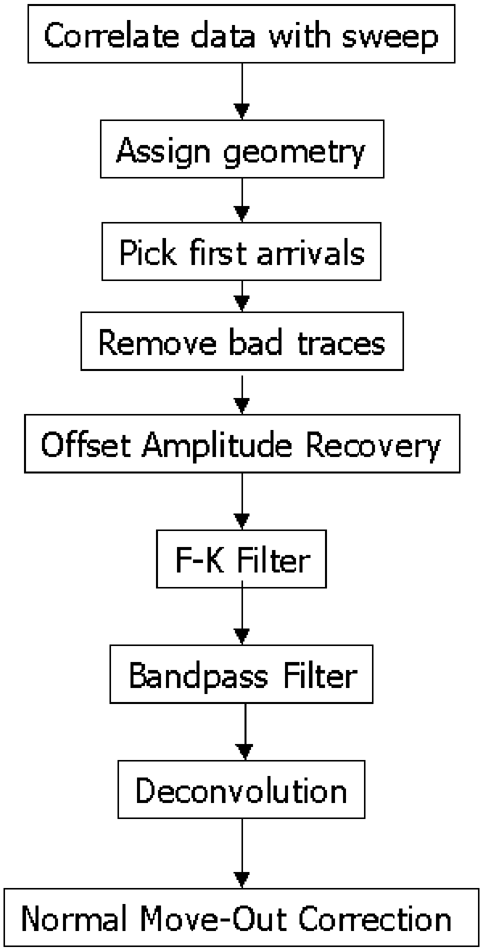

Figure 4.13 Outline of processing flow used to enhance surface seismic data shot records.

Data were sorted and mini-P shot records were isolated, then correlated with the mini-P Vibroseis sweep. Geometry was assigned, and first arrivals picked. After killing bad traces, offset amplitude recovery was used to restore true amplitudes to the data, and an F-K filter was applied to remove source-generated noise and ground roll. Data quality was enhanced using a bandpass filter and then deconvolved. Finally, a one-way normal move-out correction was applied to restore reflections to their proper arrival times. A sample shot record is illustrated in Figure 4.14. The surface data do not tie perfectly with the big-P corridor stack, time-wise.

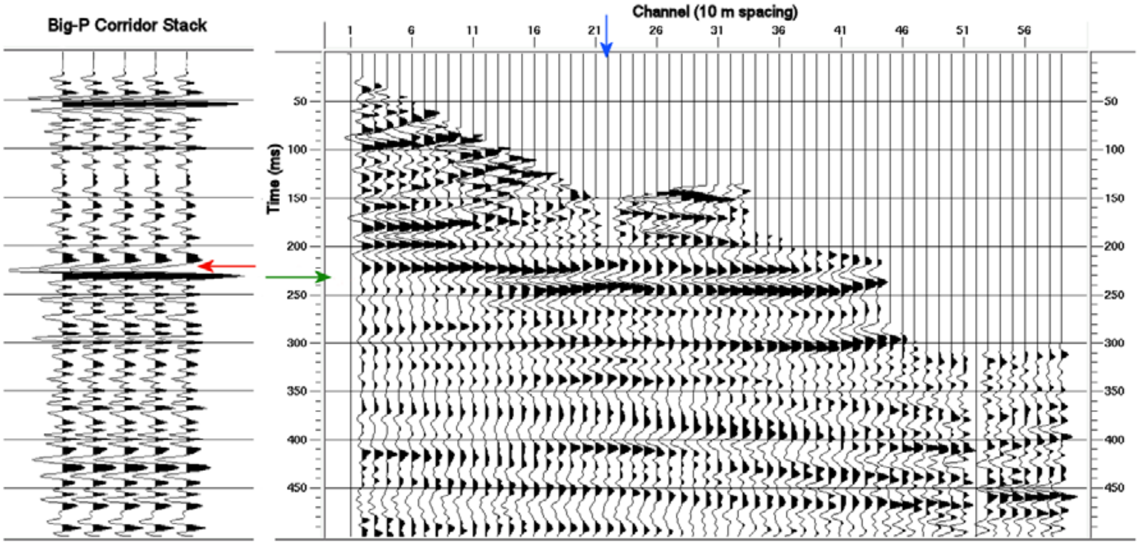

Figure 4.14 Shot record from surface seismic data recorded at Red Deer. Receiver number 22 (highlighted by blue arrow) indicates the location of the corner in the L-shaped receiver line.

The time of the big-P upper coal reflection in the corridor stack (as indicated by the red arrow) does not tie with the coal reflection imaged in the surface seismic data (green arrow), but strong coal events are indeed noted on the shot record, slightly later than those imaged using the VSP (230 ms on surface seismic, 220 ms on the zero-offset VSP). The strength of the coal response recorded on the surface data suggests that a mini-P vertical vibrator is a suitable source for not only VSP data, but also surface surveys imaging Ardley coal seams at this depth. A full-fold 3D survey is expected to successfully map lateral facies and thickness changes of the coal zone across the survey area.

4.3 Reflectivity Analysis

Vertical seismic profiles record both downgoing and upgoing wavefields, providing insight into the reflectivity of the subsurface. The ratio of incident and reflected amplitudes may be used to obtain a good estimate of the reflection coefficient of an interface, that is:

$$R_{PP} = \frac{A_{upgoingP}}{A_{downgoingP}}$$

And for converted waves:

$$R_{PS} = \frac{A_{upgoingP}}{A_{downpgoingS}}$$

where R_{PP} and R_{PS} are the reflection coefficients, and A represents the peak amplitude of a given event.

Amplitudes recorded in-situ immediately above the interface of interest are free from most wavefield propagation effects, resulting in the true amplitude reflectivity with respect to the incident wavefield. Walkaway VSP data from Red Deer were used to calculate coal reflectivity at a number of offsets, thus testing for AVO effects. The approach used was to undertake numerical modelling, followed by analysis of the field data.

4.3.1 Two-dimensional ray-tracing

A 1-dimensional model of the Cygnet strata was built using GX2 modelling software, and 2-D ray-tracing was undertaken. Densities and lithologies were derived from analysis of the 9-34 well logs, whereas P- and S-wave velocities were extracted from the zero-offset mini-P and mini-S VSP surveys. Model parameters are summarized in Table 4.1, and Figure 4.15 illustrates the model. Ray-tracing of the model was performed using the survey geometry of the Red Deer walkaway VSP. The depth and thickness of the Kneehills tuff, included in the model, is estimated from well logs in the surrounding region.

Layer Name	Depth to top (m)	Depth to base (m)	V_p (m/s)	V_s (m/s)	Density (kg/m^3)	V_p/V_s
Layer1	0	30	1900	480	2321	3.96
Layer2	30	55	2400	645	2365	3.72
Layer3	55	80	2700	825	2418	3.27
Layer4	80	105	2660	990	2422	2.69
Layer5	105	130	2675	1180	2348	2.27
Layer6	130	155	2700	1150	2347	2.35
Layer7	155	180	2610	1120	2355	2.33
Layer8	180	193.5	2825	1200	2395	2.35
UpsandA	193.5	205	2872	1500	2355	1.91
LwsandA	205	228	3080	1400	2333	2.2
Layer9	228	230	3250	1000	2180	3.25
Layer10	230	243	2400	1100	2342	2.18
sandB	243	251	3050	1250	2325	2.44
Layer11	251	255	2290	1250	2408	1.83
Layer12	255	272	2740	1300	2361	2.11
SandC	272	282	3050	1140	2427	2.68
Ardley	282	294	2450	1010	1905	2.43
Layer13	294	320	2800	1300	2440	2.15
Tuff	320	330	2500	1100	2100	2.27
Layer14	330	350	2800	1300	2440	2.15

Table 4.1 Model parameters used in GX2 model of Red Deer strata.

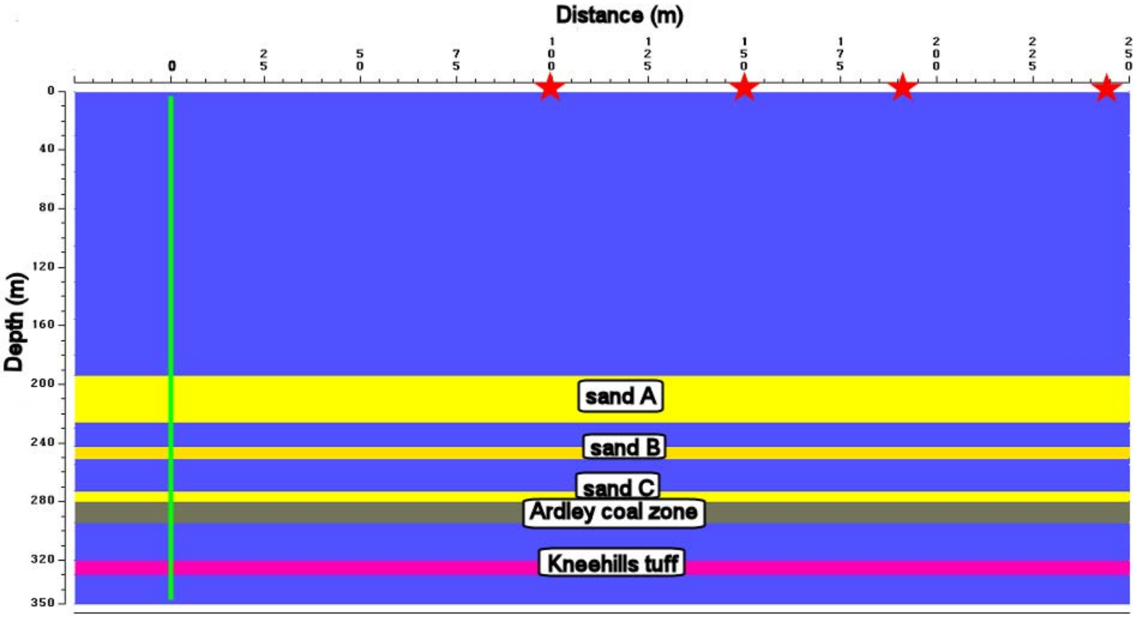

Figure 4.15 Illustration of GX2 model used to numerically simulate the Red Deer study site. Sand layers are yellow, Ardley coal strata are grey, and the Kneehills tuff is pink. Wellbore is green line at distance 0, and shot points are indicated with red stars.

GX2 allows individual horizons to be turned on or off as active reflectors during ray-tracing. Initially, only the upper coal contact was used as an active reflector. Ray-tracing was performed in both P-P and P-S modes, and traces were generated by convolution with an 80 Hz Ricker wavelet. This wavelet was chosen to simulate the dominant frequency found in field data.

Receiver types can be varied during ray-tracing such that an omni-phone (recording the total wavefield), a vertical-component geophone, or a horizontal-component geophone may be used. Ray-tracing was run using each of these geophone types, and incidence angles were extracted from the rays to calculate the total wavefield amplitude from either a vertical or horizontal geophone (Figure 4.16).

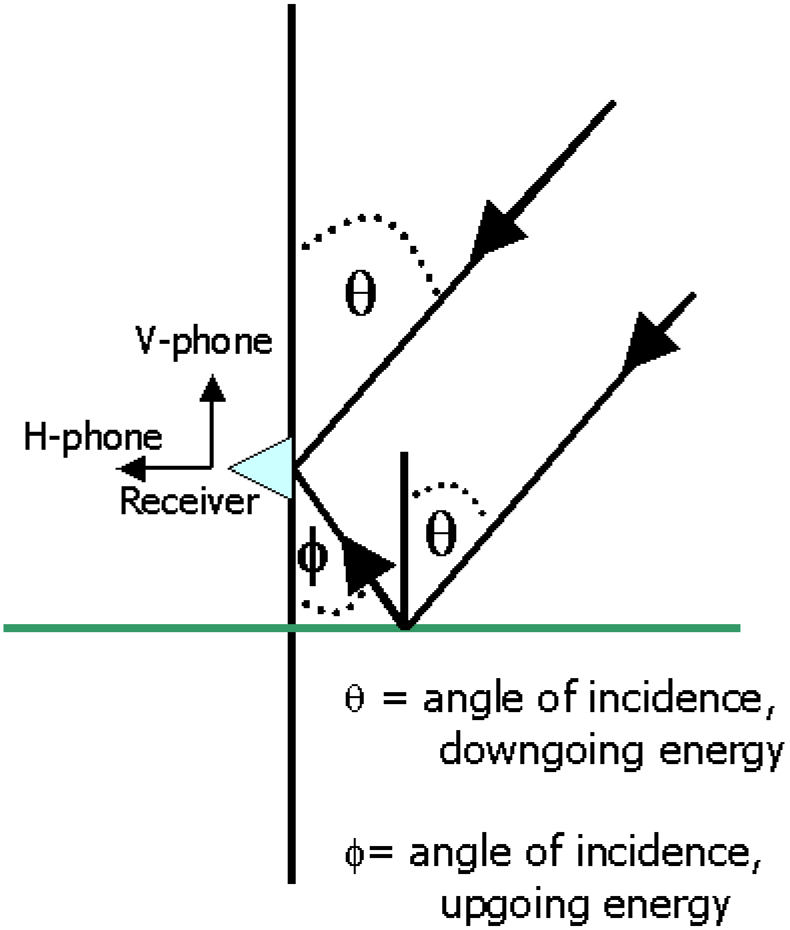

Figure 4.16 Angles of incidence for downgoing and upgoing energy. Angles can be used in conjunction with vertical or horizontal amplitude to calculate the total wavefield amplitude.

Using simple triangle geometry, the amplitude of the total downgoing wavefield can be written as:

$$A_{downgoing(P)} = \frac{A_{vertical(P)}}{\cos\theta}$$

where A is the peak amplitude of a given event. In this case, amplitudes were found by examining the data in ProMAX VSP and picking the maximum (peak or trough) amplitude of the given event. The amplitude of the total upgoing wavefield can be calculated by:

$$A_{upgoing(P)} = \frac{A_{vertical(P)}}{\cos\phi}$$

In the converted-wave case, it is easier to extract the upgoing S-wave amplitudes from the horizontal component of the receiver, so the total amplitude is found by:

$$A_{upgoing(S)} = \frac{A_{horizontal(S)}}{\sin\phi}$$

In the GX2 model, as the reflectivity of the coal top is being examined, the only receiver made active for ray-tracing was that located at 279 m depth, the receiver immediately above the top of coal. Coal reflectivity was calculated using both omniphone amplitudes and those amplitudes calculated using incidence angles. The P-P reflectivity results are summarized in Table 4.2. Amplitudes are stated in relative values, not in units. To assess the GX2 results, reflectivities were also calculated using the CREWES Zoeppritz Explorer, using incidence angles determined from the GX2 ray-tracing.

Offset (m)	Omni down amplitude	θ (degrees)	V down amplitude	Omni up amplitude	ϕ (degrees)	V up amplitude	Omni PP Reflectivity	Angled PP Reflectivity
100	-0.77	21.61	-0.71	0.17	19.22	0.16	-0.22	-0.22
150	-0.77	31.14	-0.66	0.17	27.92	0.15	-0.22	-0.22
191	-0.73	37.67	-0.58	0.17	34.03	0.14	-0.23	-0.23
244	-0.71	44.67	-0.51	0.17	40.74	0.13	-0.24	-0.24

Table 4.2 PP reflectivity calculated using GX2 ray-tracing software. Reflectivity calculated using omniphone amplitudes matches that calculated using vertical-component amplitudes and angles of incidence.

Using Zoeppritz equations to calculate the coal reflectivity based on the model parameters, it becomes clear that GX2 software produces relatively accurate amplitudes, with differences increasing slightly with offset (Table 4.3).

Offset (m)	GX2 Reflectivity	Zoeppritz Reflectivity	Difference (%)
100	-0.22	-0.22	0
150	-0.22	-0.22	0
191	-0.23	-0.22	4.3
244	-0.24	-0.23	4.2

Table 4.3 Comparison of GX2 PP reflectivity to values calculated using Zoeppritz equations.

Zoeppritz equations also indicate that no measurable P-P AVO gradient will be noted in the top coal reflection (Figure 4.17). Until large incident angles (>50°) are reached, reflectivity varies by no more than 0.04, remaining near constant at approximately 0.22. This suggests that any amplitude variations noted in the PP reflectivities will be the result of lateral variations in coal properties, not simply an AVO effect.

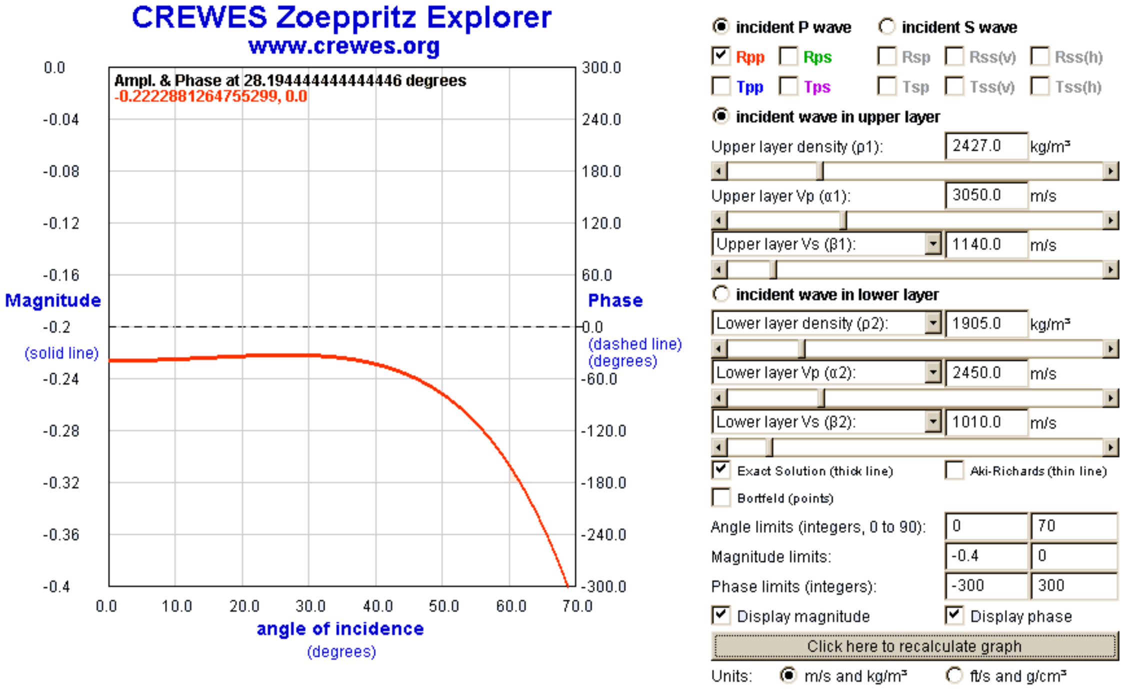

Ampl. & Phase at 28.194444444444446 degrees
-0.2222881264755299, 0.0

● incident P wave ○ incident S wave
☑ Rpp ☐ Rps ☐ Rsp ☐ Rss(v) ☐ Rss(h)
☐ Tpp ☐ Tps ☐ Tsp ☐ Tss(v) ☐ Tss(h)
● incident wave in upper layer
Upper layer density (ρ1): 2427.0 kg/m³
Upper layer Vp (α1): 3050.0 m/s
Upper layer Vs (β1): 1140.0 m/s
○ incident wave in lower layer
Lower layer density (ρ2): 1905.0 kg/m³
Lower layer Vp (α2): 2450.0 m/s
Lower layer Vs (β2): 1010.0 m/s
☑ Exact Solution (thick line) ☐ Aki-Richards (thin line)
☐ Bortfeld (points)
Angle limits (integers, 0 to 90): 0 70
Magnitude limits: -0.4 0
Phase limits (integers): -300 300
☑ Display magnitude ☑ Display phase
Units: ● m/s and kg/m³ ○ ft/s and g/cm³

Figure 4.17 Calculated Zoeppritz PP reflectivity for upper coal contact using model parameters (www.crewes.org). PP reflection coefficient shows virtually no variation until incident angles of greater than about 40 degrees are reached.

4.3.2 Red Deer PP reflectivity

Application of this reflection coefficient calculation technique to the Red Deer data set allows reflectivity of the Ardley coal to be evaluated. Vertical component amplitudes were used in conjunction with incident angles extracted from ray-tracing to calculate the total wavefield amplitudes, and thus, coal reflectivity. Downgoing peak amplitudes were found using the Schlumberger separated “P-down” dataset, and upgoing amplitudes were extracted from the separated “P-up” dataset. All amplitudes were extracted from the receiver located at 279 m depth, that is, the receiver immediately above the top of the coal zone. Calculated Ardley coal zone reflectivities are summarized in Table 4.4.

Amplitude values are digital values from processing, and are relatively scaled, not given in units.

Offset (m)	V- down amplitude	θ (degrees)	V- up amplitude	ϕ (degrees)	PP Reflectivity
100	-43.44	21.61	27.33	19.22	-0.62
150	-30.21	31.13	22.38	27.92	-0.72
191	-22.71	37.67	16.78	34.03	-0.71
244	-18.45	44.67	12.59	40.74	-0.64

Table 4.4 Summary of PP reflectivity calculated using Red Deer walkaway VSP data.

It is immediately evident that the calculated reflectivity values from the Red Deer data set do not match those predicted by the GX2 ray-tracing or Zoeppritz equations. This is due to the fact that the predicted reflection coefficients are based strictly on the top of coal reflection, and do not include wavelet interference from any other reflectors. To more accurately predict the coal reflectivity, a detailed model of the coal was built. Blocking the well logs using a median algorithm allowed calculation of new layer parameters. Log blocks were chosen based on sharp contrasts in traveltime or density values. Original logs are shown in Figure 4.18, whereas blocked logs are shown in Figure 4.19. Detailed coal model parameters are outlined in Table 4.5.

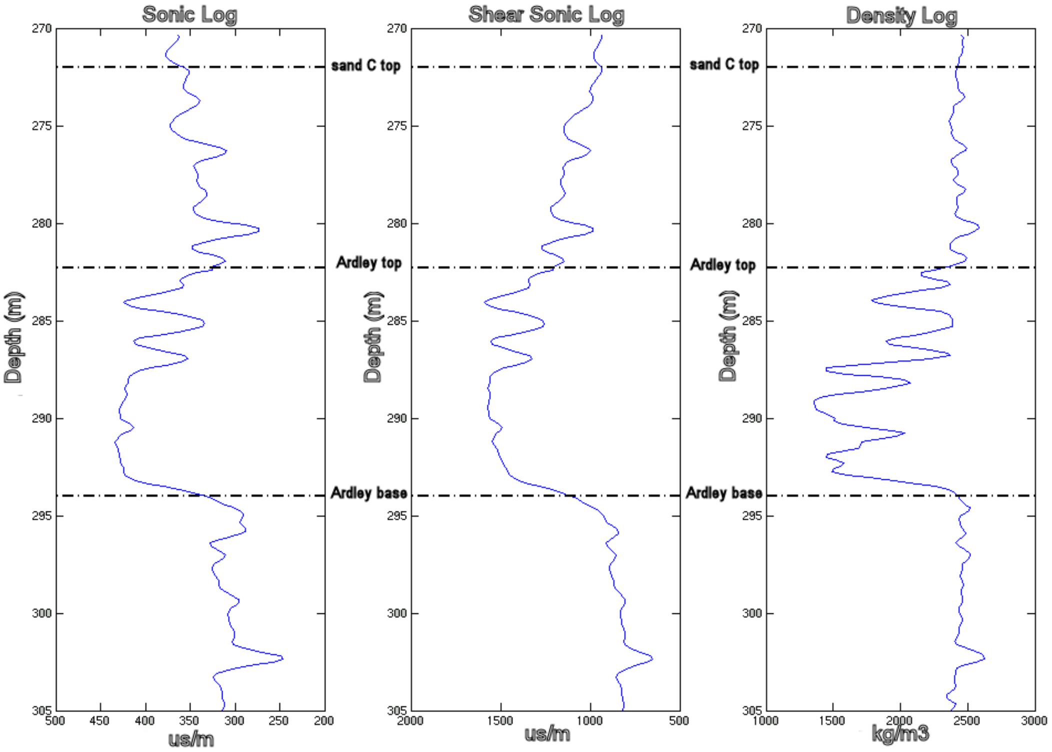

Figure 4.18 Detailed well logs of the coal zone and surrounding strata, prior to blocking.

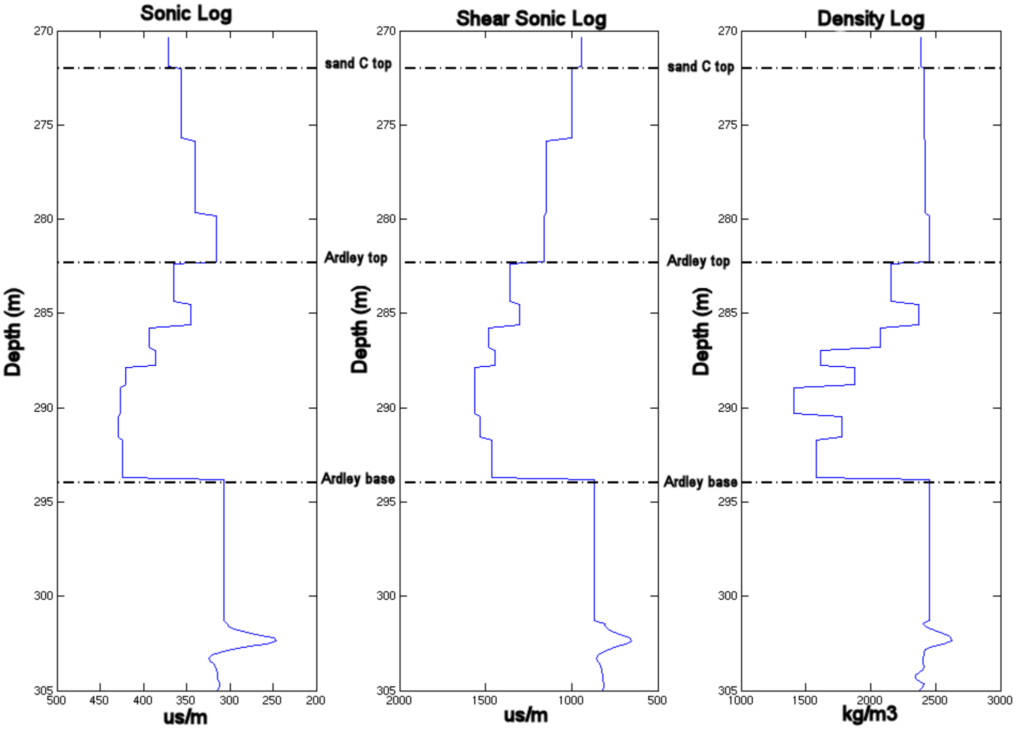

Figure 4.19 Detailed well logs of coal zone and surrounding strata, after median blocking.

Layer name	Depth to top (m)	Depth to base (m)	Vp (m/s)	Vs (m/s)	Density (kg/m3)
Overburden	0	272	2740	1300	2361
Sand C 1	272	276	2809	1000	2410
Sand C 2	276	280	2941	870	2422
Sand C 3	280	282	3180	864	2450
Ardley 1	282	284.5	2717	726	2160
Ardley 2	284.5	285.5	2899	769	2379
Ardley 3	285.5	286.5	2481	660	2010
Ardley 4	286.5	287.5	2740	730	2080
Ardley 5	287.5	294	2364	656	1600
Underlying 1	294	296	3390	1093	2462
Underlying 2	296	302	3252	1200	2455
Underlying 3	302	350	2800	1300	2440

Table 4.5 Model parameters extracted from blocked logs for detailed coal ray-tracing model.

Amplitude analysis of results from ray-tracing the detailed model with all horizons turned on as active reflectors results in reflectivity values that are very close to the reflectivity calculated from the Red Deer data (Table 4.6).

Offset (m)	Down amplitude	Up amplitude	GX2 PP Reflectivity	Red Deer PP Reflectivity
100	0.91	-0.57	-0.63	-0.62
150	0.87	-0.50	-0.58	-0.72
191	0.82	-0.56	-0.68	-0.71
244	0.79	-0.57	-0.73	-0.64

Table 4.6 Comparison of detailed GX2 coal model PP reflectivity values with Red Deer PP reflectivity values. Amplitudes were extracted using an omni-phone receiver.

Examination of the reflectivity values from the detailed GX2 model and the Red Deer strata (Figure 4.20) suggests that no measurable AVO gradient will be noted at this study site. Although tuning effects can not be accounted for simply in Zoeppritz equations, evidence from the Red Deer data and detailed ray-tracing suggests that amplitude variations in coal reflections will be the result of lateral changes in thickness and/or coal properties, and not the result of AVO effects, as predicted in the simple single-layer model.

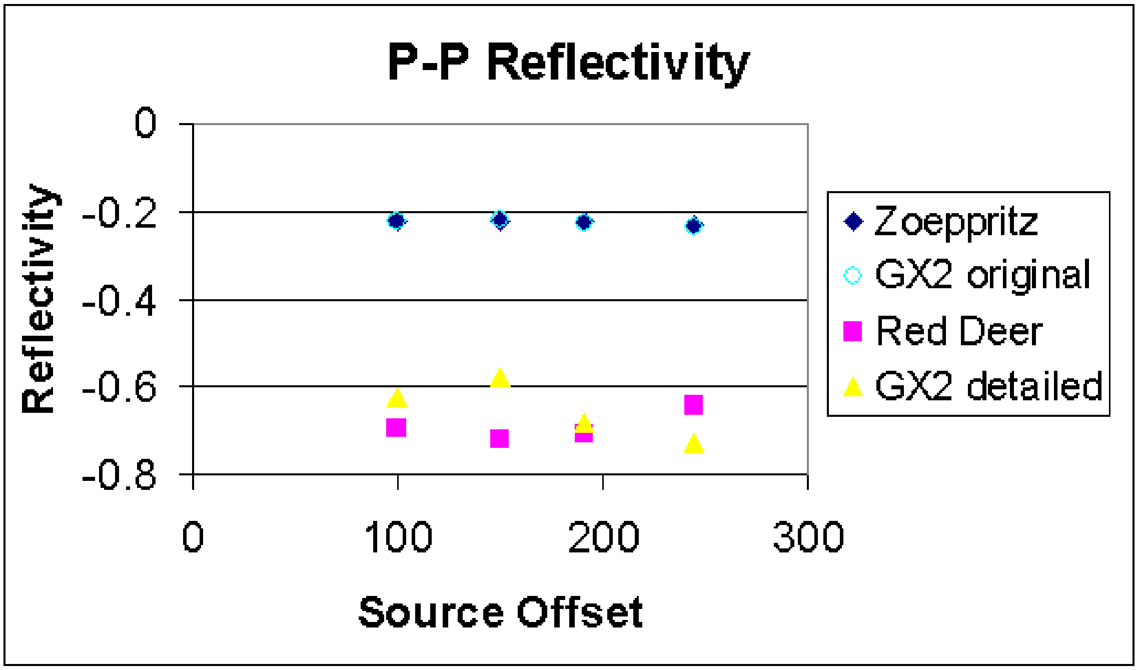

Figure 4.20 Comparison of reflection coefficients derived from single interface numerical modelling, Red Deer field data, and detailed numerical modelling.

4.3.3 Red Deer PS Reflectivity

Zoeppritz equations used to calculate the PS reflectivity of the Red Deer coal strata indicate that a larger AVO gradient will be noted in converted-wave data than in compressional data (Figure 4.21).

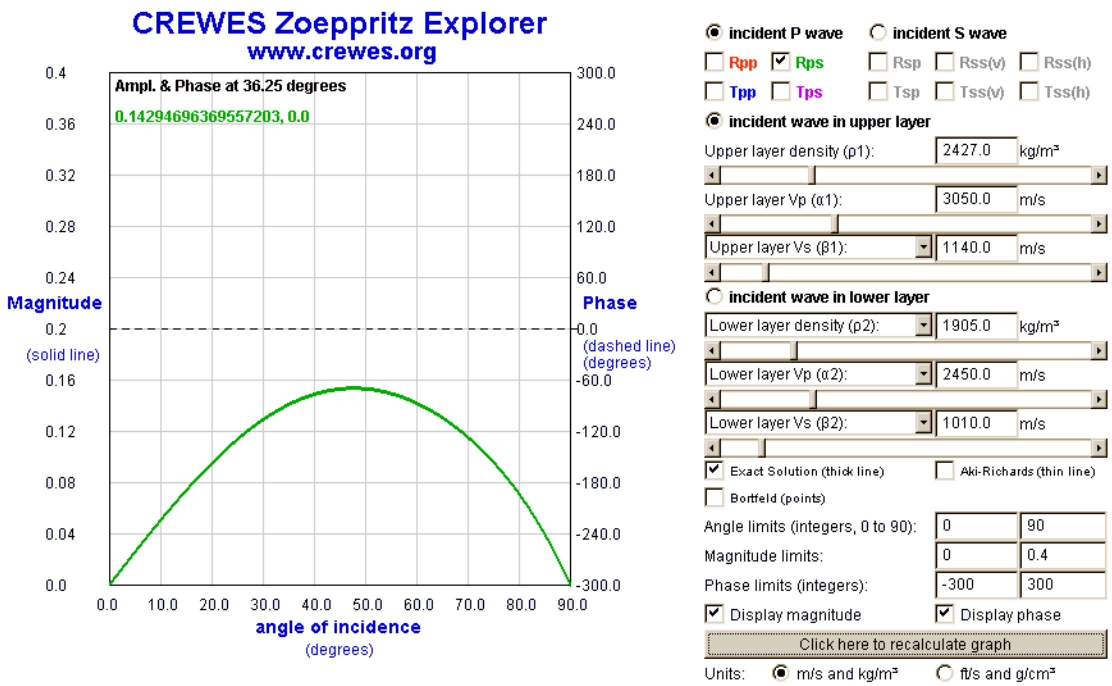

Ampl. & Phase at 36.25 degrees
0.14294696369557203, 0.0

● incident P wave ○ incident S wave
☐ Rpp ☑ Rps ☐ Rsp ☐ Rss(v) ☐ Rss(h)
☐ Tpp ☐ Tps ☐ Tsp ☐ Tss(v) ☐ Tss(h)
● incident wave in upper layer
Upper layer density (ρ1): 2427.0 kg/m³
Upper layer Vp (α1): 3050.0 m/s
Upper layer Vs (β1): 1140.0 m/s
○ incident wave in lower layer
Lower layer density (ρ2): 1905.0 kg/m³
Lower layer Vp (α2): 2450.0 m/s
Lower layer Vs (β2): 1010.0 m/s
☑ Exact Solution (thick line) ☐ Aki-Richards (thin line)
☐ Bortfeld (points)
Angle limits (integers, 0 to 90): 0 90
Magnitude limits: 0 0.4
Phase limits (integers): -300 300
☑ Display magnitude ☑ Display phase
Units: ● m/s and kg/m³ ○ ft/s and g/cm³

Figure 4.21 Calculated Zoeppritz PS reflectivity for upper coal contact using model parameters (www.crewes.org). PS reflectivity shows a slight AVO gradient, with maximum amplitudes at incident angles of approximately 48°.

Using the same methods as those used to calculate PP reflectivity, PS reflectivity values may be calculated from the Red Deer study site. GX2 numerical modelling was performed using an 80 Hz Ricker wavelet, such that the bandwidth of the modelled converted wave matches that of the incident P-wave in the field data. In this case, downgoing P-wave amplitudes are extracted from the Schlumberger “P-down” data, whereas the upgoing S-wave amplitudes are extracted from the “S-up” data. All amplitudes were extracted from the receiver located at 279 m depth, that is, the receiver immediately above the top of the coal zone. Calculated Ardley coal zone reflectivities are summarized in Table 4.7. The upward angle of incidence (ϕ) for S-waves is extracted from GX2 ray-tracing.

Offset (m)	V- down amplitude	θ (degrees)	V- up amplitude	φ (degrees)	PS Reflectivity
100	97.67	15.70	-8.99	11.16	-0.09
150	72.55	29.39	-10.43	15.22	-0.13
191	56.31	35.10	-7.41	18.24	-0.11
244	40.26	44.13	-4.53	21.35	-0.08

Table 4.7 Calculated PS reflectivity values from Red Deer walkaway VSP data.

Calculated Red Deer PS reflectivity values differ from the PS reflectivity values predicted by Zoeppritz calculations (Table 4.8), although to a much lesser degree than the PP values varied. Original single-interface GX2 and Red Deer PP reflectivities differed by over 300%, whereas the maximum PS difference between single-interface modelling and field data is only 67%. Although the converted-wave data are still affected by tuning, it appears that PP reflectivity is far more influenced by tuning effects than PS data (Figure 4.22). The greater interference noted in the PP data results from the longer wavelengths present in the PP data set. In comparison, the lower PS velocities yield shorter wavelengths for the same dominant frequency, and thus, improved resolution relative to the PP data.

Offset (m)	Red Deer PS Reflectivity	Zoeppritz PS Reflectivity
100	-0.09	-0.06
150	-0.13	-0.07
191	-0.11	-0.09
244	-0.08	-0.10

Table 4.8 Comparison of calculated Zoeppritz PS reflectivity for Ardley coal with PS reflectivity extracted from Red Deer walkaway VSP data.

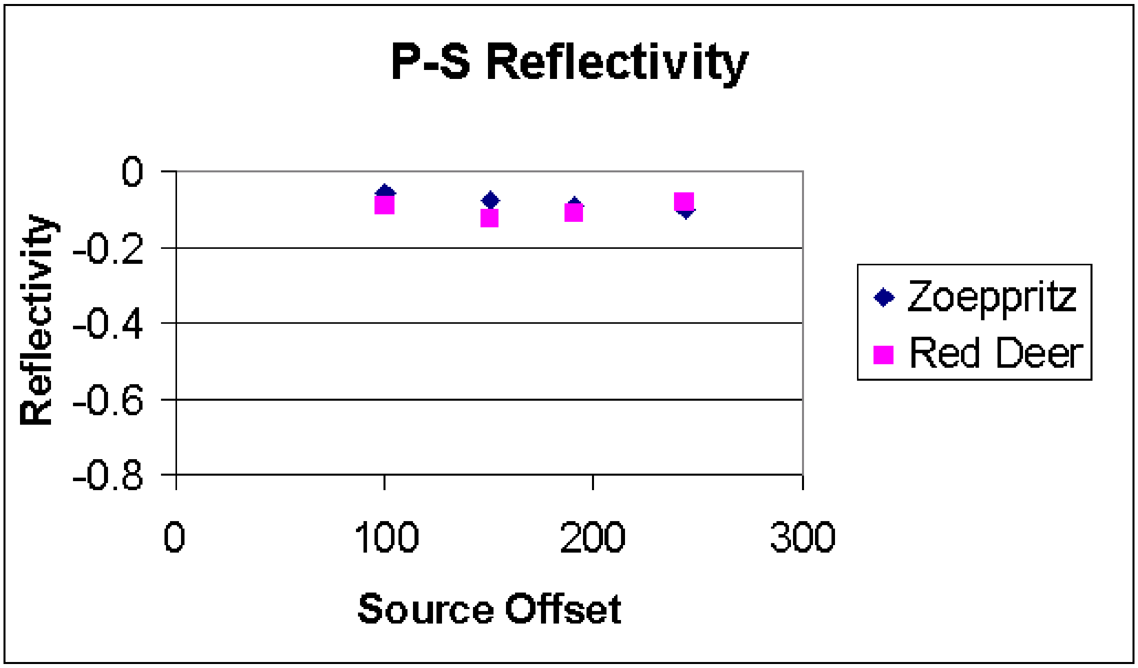

Figure 4.22 Comparison of PS reflectivity derived from single-interface numerical modelling, and Red Deer field data.

As shown above, Zoeppritz calculations of expected PS reflectivity show an AVO gradient. The Red Deer reflectivity data, based on analysis of the field data, varies with offset, but not in a consistent or predictable fashion. Complexities of real data (tuning effects, noise) obscure the AVO effect predicted. It appears that large variations in PS reflectivity will, as in the PP case, most likely be a result of lateral changes in coal properties, and not simply as a function of offset.

4.4 Discussion

Imaging of Ardley coal seams using walkaway vertical seismic profiles is effective. Both the VSP-CDP and VSP-CCP transforms (for PP and PS data, respectively) clearly image the upper and lower coal contacts. At the nearest offset (100 m), the converted-wave data was able to image an intra-coal event, unlike the PP imaging. With increasing offset, the PP data proved to be of better quality than the PS survey, and produced the better image at the farthest offset of 244 m.

Generally, the reflectivities extracted from the Red Deer data set are consistent with those predicted from known elastic properties of coal. Tuning effects are evident in the Red Deer data, resulting in much larger reflection coefficients for the top of coal than those calculated by Zoeppritz equations, particularly in the PP case. The shorter wavelengths present in converted-wave data result in PS reflectivity values far less affected by tuning than PP reflectivity values, with extracted PS reflectivities much nearer those predicted theoretically.

The degree to which the PP reflectivity of the coal zone will be affected by wavelet interference will be largely dependent on both the bandwidth of the data and the number of reflectors within the coal zone. That is, the greater the number of shale partings or tight streaks within the coal zone, the greater the effect on the PP reflectivity. As such, the difference in coal reflectivity from that predicted by Zoeppritz equations may give an indication of the vertical continuity of the coal zone, an essential factor in CBM development.

Predicted amplitude variations with offset are minimal in the PP case, and relatively minor in the PS case, suggesting that any observed amplitude variations in real coal data are the result of lateral variations in coal properties, and not simply a result of increasing incident angle. It is not possible to examine

AVO in the Red Deer VSP-CDP and VSP-CCP transforms, as they display stacked amplitude variations, and are not indicative of true amplitude reflectivity. Separated raw upgoing and downgoing wavefields, however, may be used to calculate the true amplitude reflectivity of the upper coal contact. The predicted minimal AVO is borne out by the Red Deer data set, which demonstrates minor variations in extracted reflectivity, none of which are predictable based simply on offset.

Chapter 5 Modelling of Time-Lapse Seismic Imaging

5.1 Reservoir Monitoring of CO_2 injection

Any geologic CO_2 sequestration project will need monitoring to manage the filling of the reservoir, verify the quantity of CO_2 sequestered, and detect leakage (Myer et al., 2002). Seismic monitoring is attractive as it does not usually require wells to be shut-in, does not disturb reservoir fluids, and does not cause precipitation of chemicals in the reservoir (Wang & Nur, 1989). A study of cost sensitivities (Myer et al., 2002) suggests that seismic monitoring is likely to represent only a small percentage of overall sequestration costs.

Greenhouse gas sequestration is being monitored using time-lapse seismic imaging at the Sleipner field in the North Sea, and at the Weyburn field of Saskatchewan. At Sleipner, a heterogeneous CO_2 saturation pattern within the aquifer has been observed (Figure 5.1) as well as successful containment of the gas (Eiken & Brevik, 2000). Injection of carbon dioxide into the strata has altered its acoustic impedance, resulting in increased reflectivity within the reservoir, amplitude variations, and a velocity push-down effect for all reflections beneath the top of the aquifer. Repeated surveys have given insight into the development of the CO_2 plume over time (Arts et al., 2002).

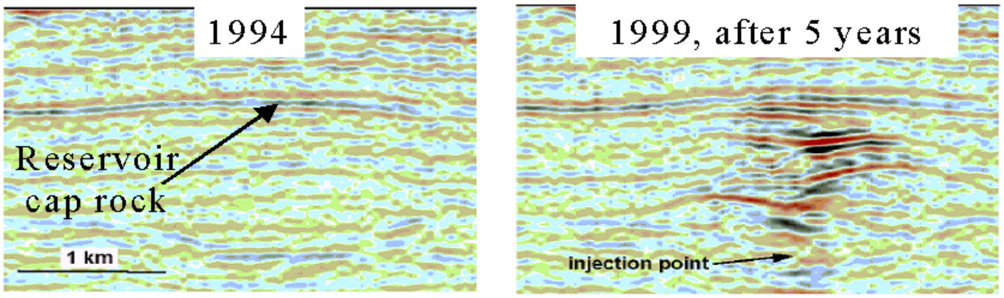

Figure 5.1 Seismic images (vertical slices) from Sleipner field taken before CO_2 injection (left) and five years after the start of injection (right). The CO_2 plume is apparently contained beneath the reservoir cap rock (Eiken and Brevik, 2000).

The Weyburn field of Saskatchewan operates under an enhanced oil recovery scheme, whereby carbon dioxide injection stimulates the flow of low-viscosity oil. At this site, time-lapse imaging has shown numerous anomalies related to the progression of the CO_2 flood in the reservoir (Li, 2003). Time delays and amplitude variations have permitted the flood to be mapped effectively, and shear-wave splitting detects the flood progress over time, particularly well in a heavily fractured zone (Davis et al., 2003).

It is believed similar effects to those noted at Sleipner and Weyburn will be imaged at the Red Deer site, but on a different scale, owing to different rock properties between the Red Deer coal, the sandy aquifer imaged at Sleipner, and the carbonate reservoir of Weyburn.

5.2 Velocity variations resulting from ECBM

Published data of any type exists only for two long-term multi-well ECBM field studies world-wide, both of which are located in the San Juan basin. Both sites are part of the United States government-industry project known as Coal-

Seq. The Allison field, in New Mexico, tests the injection of carbon dioxide, whereas the Tiffany project of Colorado examines nitrogen injection (Reeves, 2002). It has been established that as gas is released from a coal reservoir, the matrix shrinks, causing cleats to open, in turn improving permeability (Fokker & van der Meer, 2002). As another gas (such as CO_2) is adsorbed onto the coal, however, swelling of the coal matrix causes cleats to close, with a resulting loss of permeability (Fokker & van der Meer, 2002). Analysis of permeability data from the Allison unit demonstrates a reduction of permeability from 100-130 mD to the ~1 mD range, a decrease of 99% (Reeves, 2002). Seismic monitoring has not been implemented as part of the Coal-Seq project, but these fields demonstrate the need for monitoring, particularly if permeability will be affected. Techniques such as those used in fractured zones at Weyburn may potentially detect the closure of cleats before permeability is reduced drastically.

Velocity variations within coalbed methane strata have not been published, although a number of studies have examined V_p and V_s changes resulting from CO_2 injection in sandstones and carbonates. In brine-saturated sandstone samples, P-wave velocity reduction caused by CO_2 injection is typically on the order of ~10% (Xue et al., 2002). Studies on hydrocarbon-saturated sandstones demonstrate that CO_2 flooding decreased compressional-wave velocities by 4-11%, with the highest velocity variations noted in the lowest porosity samples (Wang & Nur, 1989). Shear-wave velocities in the same study were found to be insensitive to CO_2 flooding, but affected by increases in pore pressure. This suggests that if a zone shows a large decrease in both P- and S-wave velocities, it is likely to have been swept by CO_2 and experienced pore pressure buildup (Wang & Nur, 1989). Time-lapse surveys of a CO_2 flood in a carbonate reservoir of the McElroy field of West Texas show a decrease in V_p of about 6%, and a V_s decrease of around 2% (Wang et al., 1998).

Each of these cases, however, involves reservoirs in which a liquid pore fluid (brine, oil) interacts with introduced pore fluids, either liquid or gaseous CO_2. This contrasts to the ECBM case, in which pore space is negligible, and gases are stored adsorbed on the matrix. Additionally, CBM production relies on dewatering prior to CO_2 injection, complicating the velocity distribution.

To estimate velocity and density decreases resulting from the dewatering phase of CBM production, physical tests were conducted on samples of the Ardley coal. Measurements taken of both wet and dry coal samples demonstrate that complete dewatering of coal results in an approximately 20% decrease in compressional velocity and a 15% density decrease (Richardson and Lawton, 2002). Complete dewatering is not possible under reservoir conditions, so P-wave velocity and density decreases of 10% each are used in the following numerical modelling to simulate the effects of dewatering. Shear-wave velocities are assumed to not vary with dewatering. The velocity and density variations that arise from CO_2 injection after dewatering are insufficiently known at this time to be included in this numerical study.

5.3 1.5-D numerical modelling

Using Zoeppritz equations to calculate reflectivity, it becomes apparent that the reflectivities of wet and dry coal exhibit similar behaviours (Figure 5.2). As in the wet coal case, the PP reflectivity of dry coal demonstrates no AVO gradient until large (>50°) incident angles are reached. The magnitude of the PP reflectivity is greater in the dry coal case, as is expected based on the change in rock properties. When performing a time-lapse survey over dewatered coal, amplitude variations should mark the difference between wet and dry coal, and any AVO effects will be second order. As demonstrated in Chapter 4, the P-S data are expected to be less affected by tuning and better resolve the top of coal.

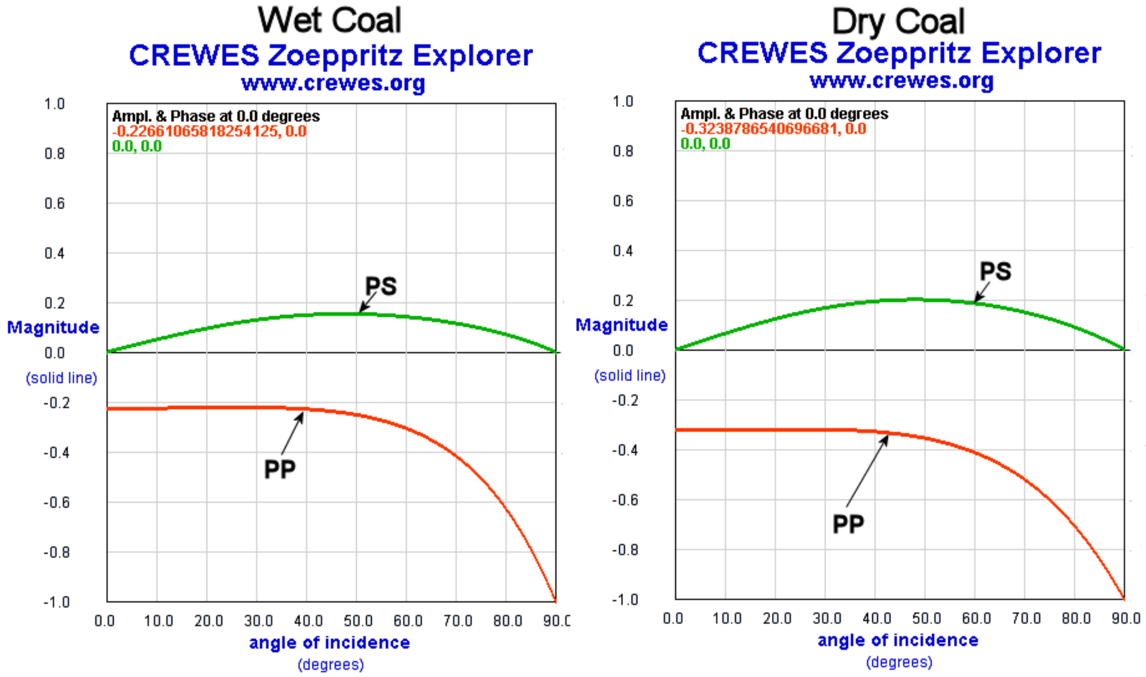

Figure 5.2 Comparison of PP and PS reflectivity for wet and dry coal seams. Dry coal is assumed to have undergone a 10% reduction in both velocity and density (www.crewes.org).

Converted-wave reflectivity demonstrates a similar character in both the wet and dry coal cases, reaching maximum amplitude at approximately 48° incidence. The AVO gradient is slightly more pronounced in the dry coal case than in the wet coal case, although in both cases, the gradient is reasonably large. The variation in actual reflectivity values between wet and dry coal is far less than that noted in the PP case. This suggests that PP reflectivity will be more diagnostic in distinguishing wet and dry coal. If repeated surveys use the same geometry, however, differencing the two surveys will highlight the areas of dewatering.

5.3.1 Synthetic seismograms

One-and-a-half-dimensional modelling examines offset seismic reflections generated using wellbore geology. That is, the geology is assumed to remain constant across the seismic section, so it is one-dimensional, whereas the seismic reflections are generated from 2-D ray-tracing. Digital sonic and density well logs from the 9-34 well were used to generate both compressional- and converted-wave offset synthetic seismograms illustrating the expected "baseline", prior to CBM production. Density and velocity values were altered within the coal zone to mimic the effects of dewatering, after which new seismograms were created. The expected change in the seismic response of the coal zone is illustrated by examining the difference between the seismograms. Although Lawton & Lyatsky (1991) demonstrate that synthetic seismograms generated using density logs alone effectively model coal seams in Alberta, log suites including compressional sonic, shear sonic, and density were used to allow the modification of both P-wave velocity and density values, and to model both the compressional and converted-wave responses of the strata.

Because of the poor quality of the shear sonic log data in the upper portion of the well, a synthetic shear sonic log created using interval Vp/Vs values from the zero-offset VSP surveys was used for modelling. This synthetic shear sonic log also included the base of the coal, which was missed in the cased hole shear sonic log. It has been demonstrated in Chapter 4 that the Red Deer coal response is affected significantly by tuning, so it was deemed essential that the base of coal be included in modelling. The similarity of Vp/Vs values extracted from the well logs and the VSP data suggests that this synthetic log should provide equally accurate numerical modelling results. The full suite of logs used for modelling is illustrated in Figure 5.3.

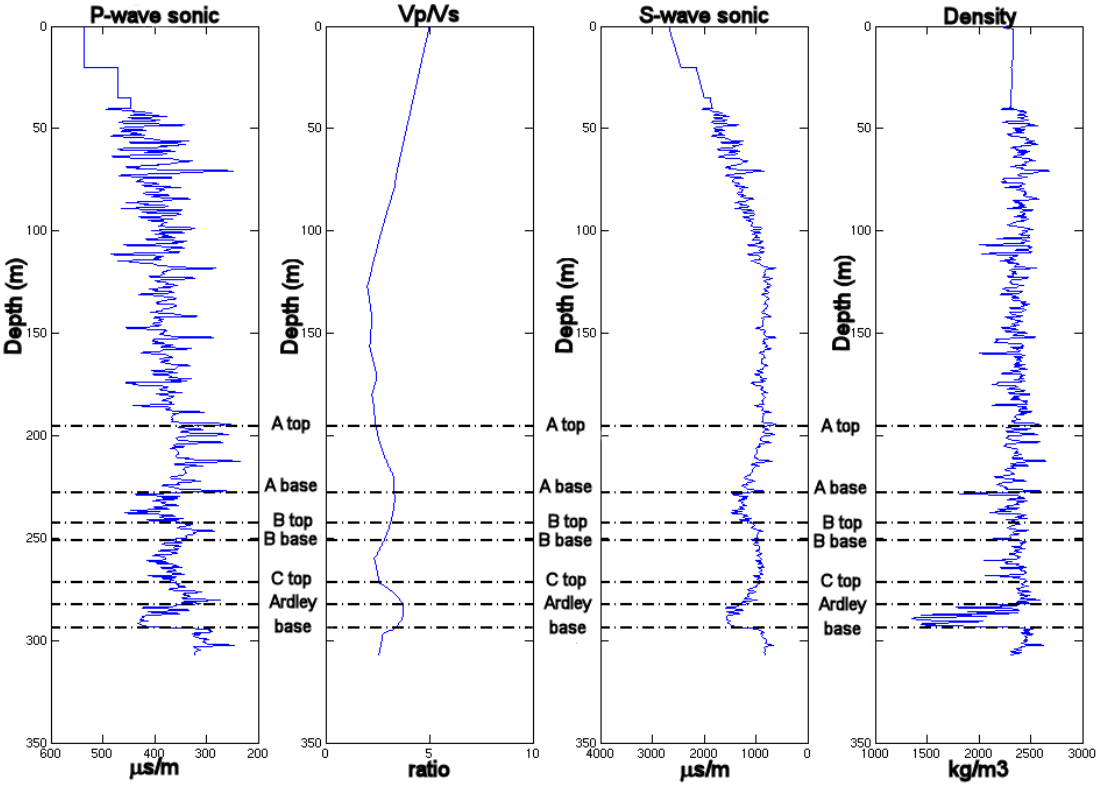

Figure 5.3 Well logs used to create 1.5-D synthetic seismograms. Compressional sonic and density logs were recorded on wireline, whereas the Vp/Vs and S-sonic logs were created using interval velocities derived from first arrivals of zero-offset VSP surveys.

5.3.2 P-P modelling results

Synthetic seismograms (with NMO removed) of the Red Deer strata were created by convolution of the 9-34 integrated well logs with the extracted mini-P vibrator wavelet (Figure 5.4). Baseline P-P seismograms demonstrate a strong coal reflectivity, highlighting both the upper and basal coal contacts with surrounding strata, as well as an intra-coal event, which is consistent with the mini-P field data (Figure 5.5).

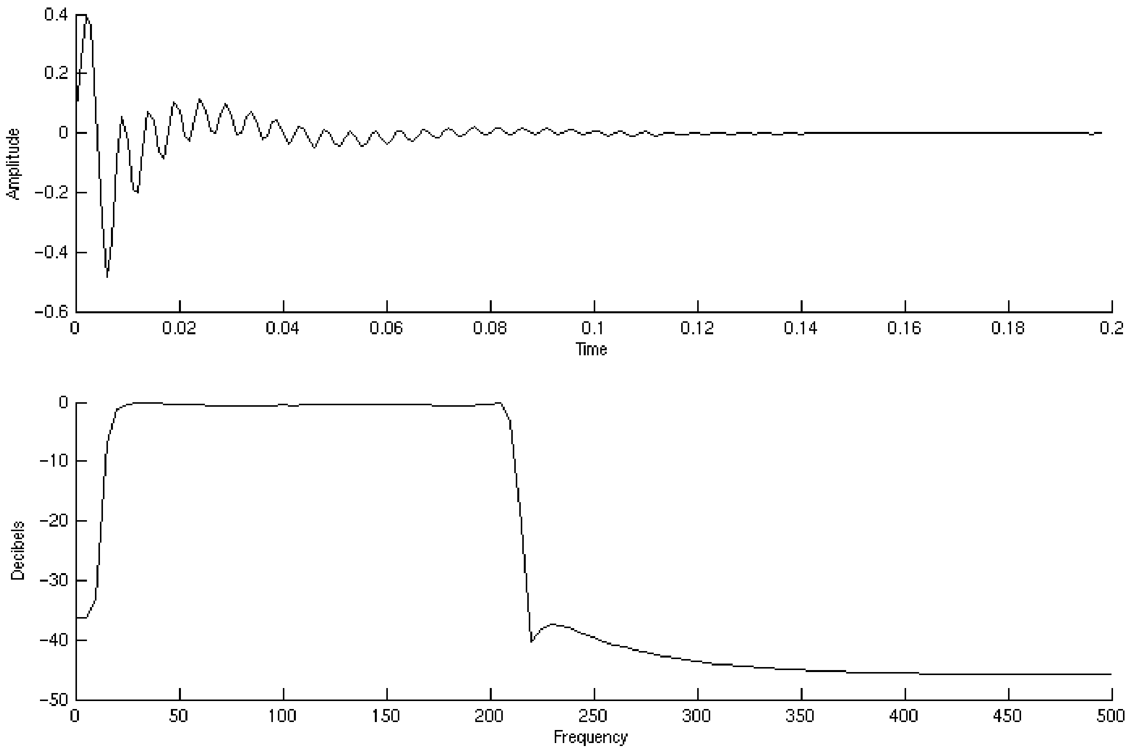

Figure 5.4 Mini-P vibrator wavelet convolved with well logs to produce the P-P synthetic seismograms of Red Deer strata.

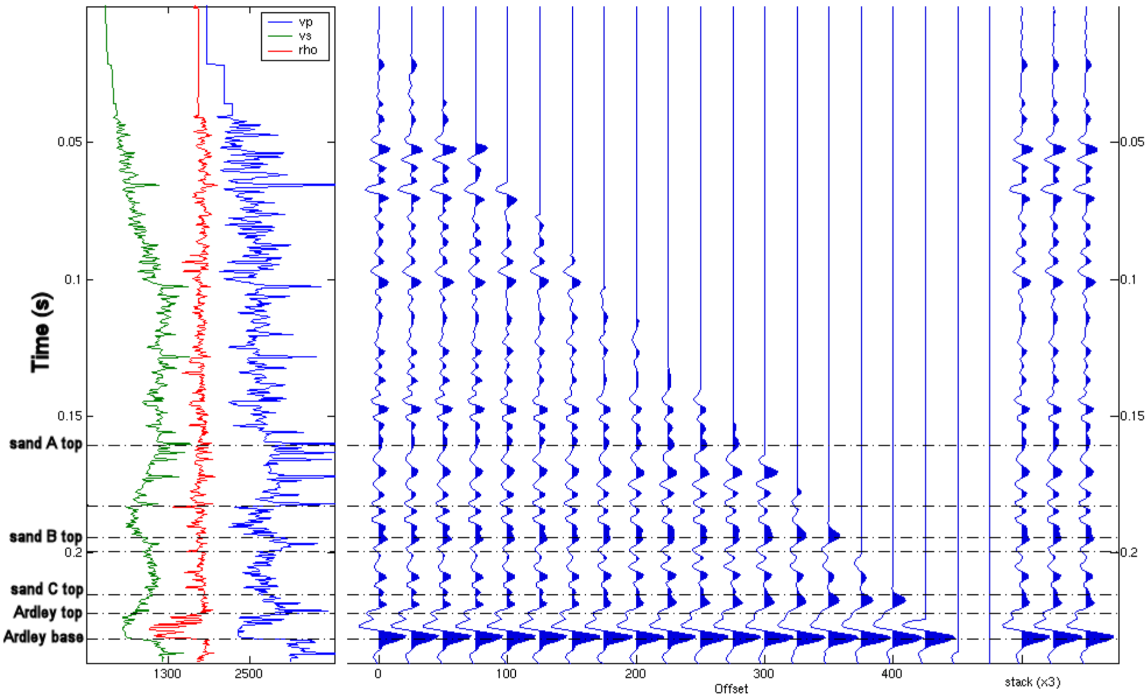

Figure 5.5 Baseline P-P synthetic seismogram of Red Deer strata. Both upper and lower coal contacts are easily distinguished, and an intra-coal event is detectable.

The baseline coal response shows very little amplitude variation with offset. Small AVO effects are noted at an offset-to-depth ratio greater than one. Amplitudes of the upper coal event decrease with increasing offset, whereas amplitudes of the lower coal reflection increase with increasing offset. Changes in the coal reflection character after time-lapse are not immediately visible on the time-lapse seismogram (Figure 5.6), but evident when the difference between the two seismograms is calculated (Figure 5.7). After dewatering, the coal shows increased reflectivity, and all events underlying the upper coal contact have been delayed in time. Amplitudes are scaled relative to the baseline P-P case.

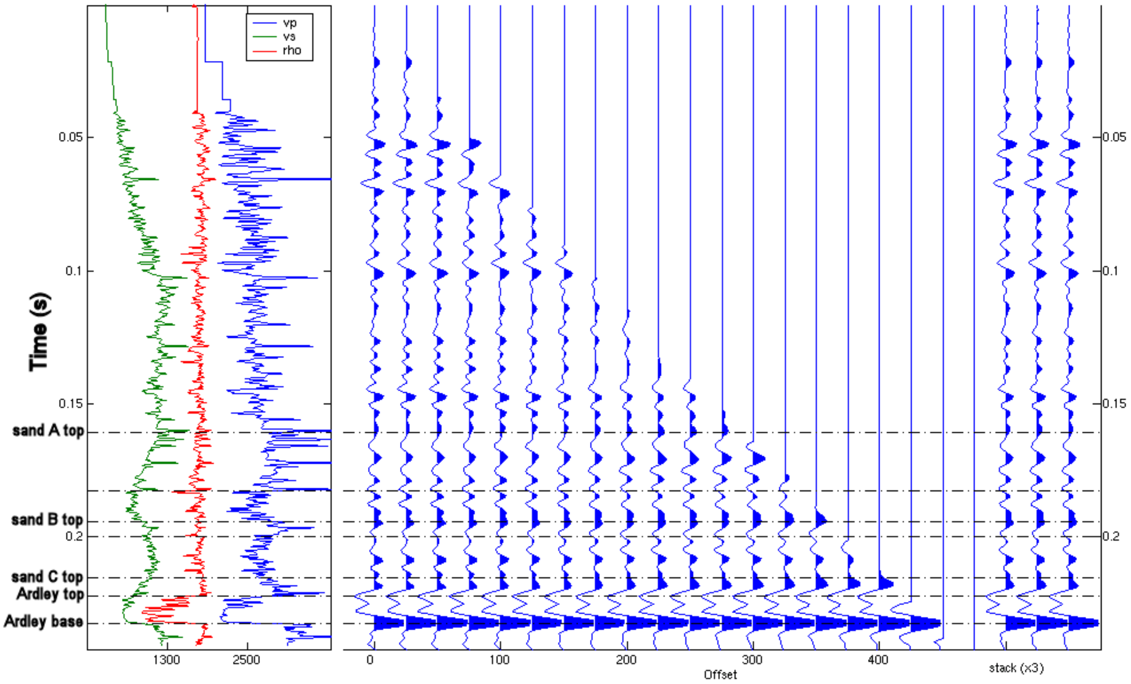

Figure 5.6 Time-lapse P-P synthetic seismogram of Red Deer strata. Coal density and velocity have been reduced by 10%, resulting in slightly increased reflectivity within the coal zone.

The dewatered synthetic seismogram shows reduced AVO effects when compared to the baseline survey. Both upper and lower coal reflections maintain visually constant amplitudes to an offset-to-depth ratio of 1.5. The intra-coal event is evident at all offsets, whereas in the baseline seismogram it is suppressed by tuning at the far offsets.

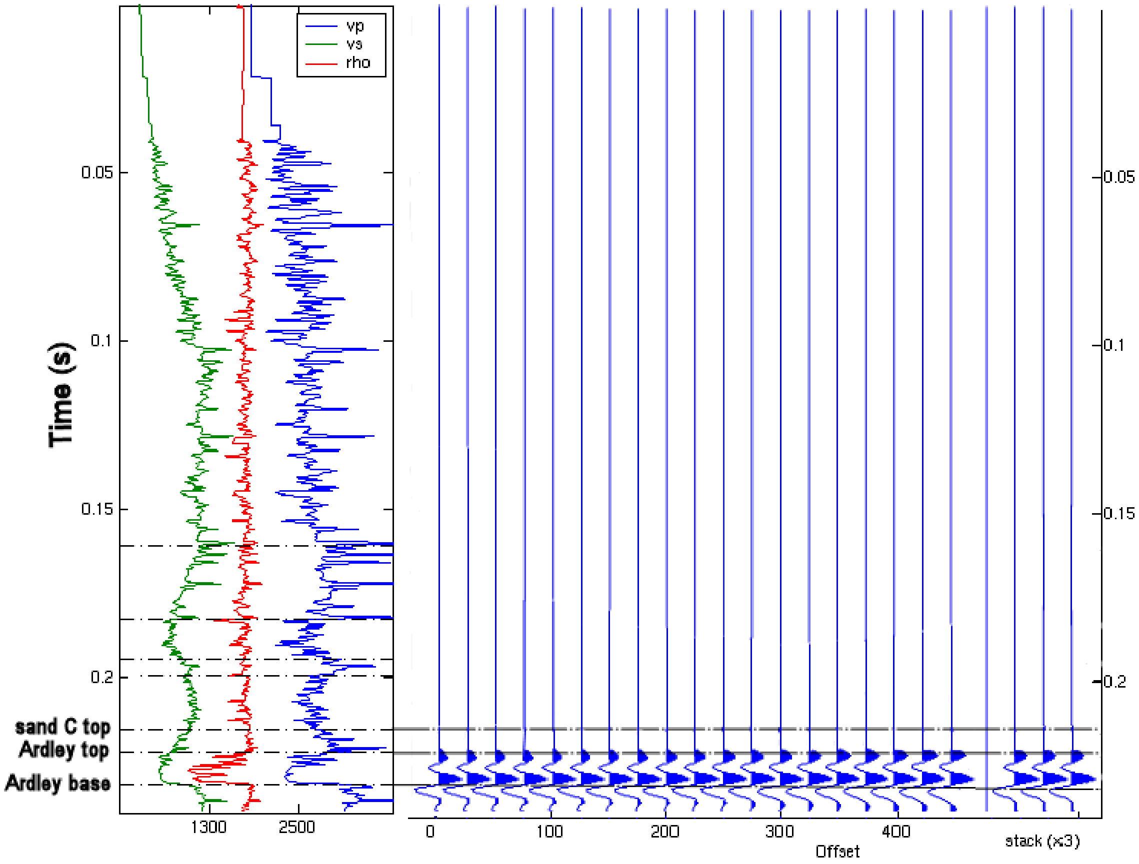

Figure 5.7 Difference between baseline and time-lapse P-P synthetic seismograms of Red Deer strata. Coal reflectivity has changed, and all events underlying the top of the coal are delayed in time.

5.3.3 P-S modelling results

It stands to reason that if variations in velocity and density values result in a time-lapse difference in compressional-wave data, a difference should also be noted in converted-wave data. Although shear wave velocities are assumed not to be affected by coal dewatering, the travel time for a converted wave will be slightly altered, as the downward wavefield (the P-wave) will experience a reduced velocity through the dewatered coals, while the velocity of the upward wavefield (S-wave) will be unaffected by dewatering. Converted wave synthetic seismograms were created by convolution of the well log reflectivity with a lower bandwidth vibrating source wavelet designed to simulate the higher attenuation of shear waves (Figure 5.8), based on the P-S wavelet at the shallow receivers in the offset VSP surveys. The baseline P-S response of the Red Deer strata is illustrated in Figure 5.9.

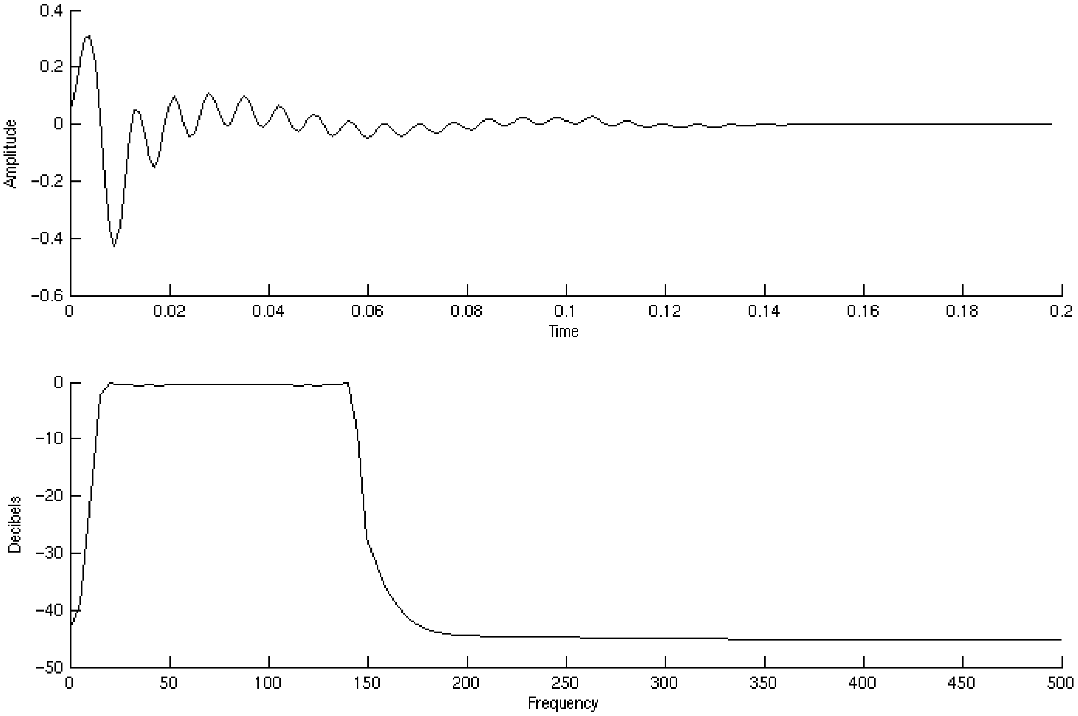

Figure 5.8 Lower bandwidth vibrating source wavelet convolved with well logs to produce the P-S synthetic seismograms of Red Deer strata.

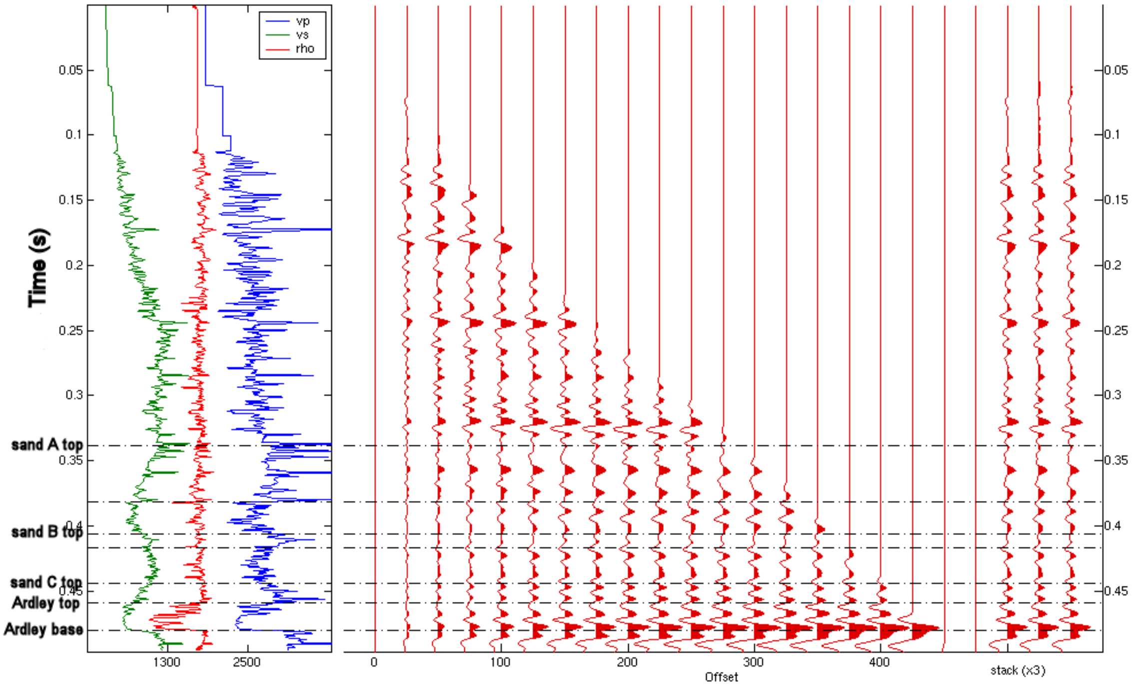

Figure 5.9 Baseline P-S synthetic seismogram of Red Deer strata. Both upper and lower coal contacts are easily distinguished, and an intra-coal event is detectable.

Small amplitude variations with offset are noted in the converted-wave coal P-S event. Although there is little noticeable change in the upper coal response, the amplitude of the lower coal reflection increases with increasing offset.

After dewatering, reflections from interfaces underlying the coal are expected to arrive at slightly later times, but the magnitude of this push-down effect is less than the magnitude of the equivalent P-P change, since the travel time is affected only in one direction. Figure 5.10 illustrates the time-lapse converted-wave modelled response of the Red Deer strata.

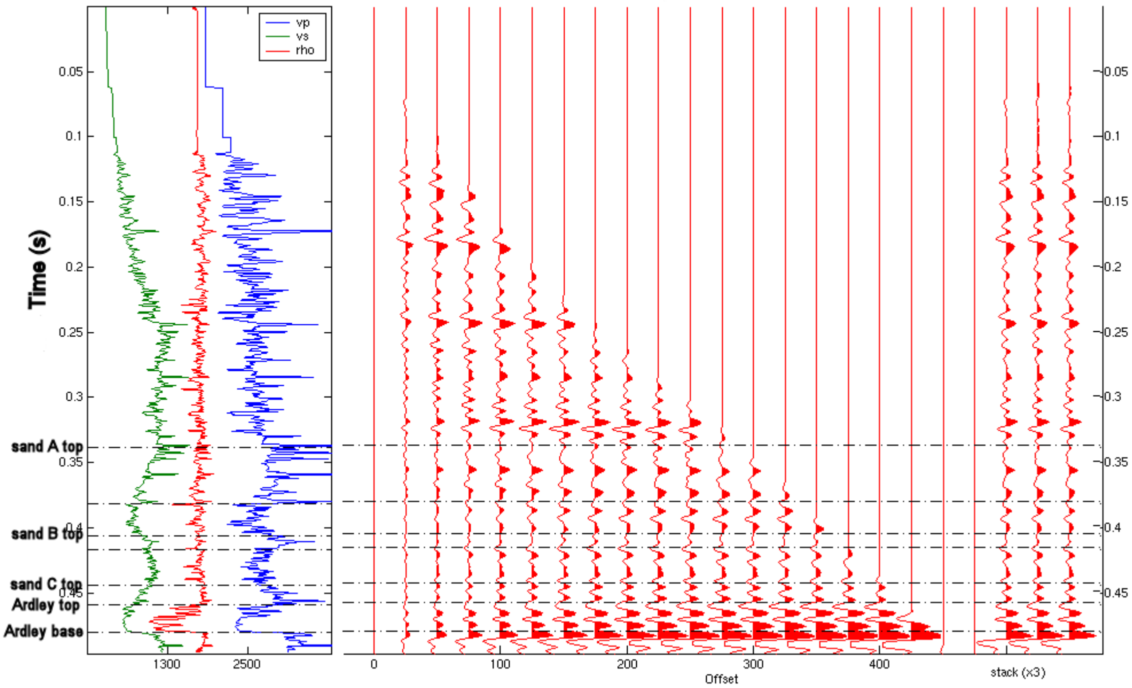

Figure 5.10 Time-lapse P-S synthetic seismogram of Red Deer strata. Coal density and velocity have been reduced by 10%, resulting in slightly increased reflectivity within the coal zone.

The time-lapse converted-wave seismogram shows increased reflectivity within the coal zone, and a velocity push-down effect in all underlying events, as seen in the difference between the baseline and time-lapse seismograms (Figure 5.11). The time-lapse and difference P-S seismograms are scaled relative to the baseline P-S seismogram. Generally, the time-lapse effects are similar to those noted in the compressional-wave response.

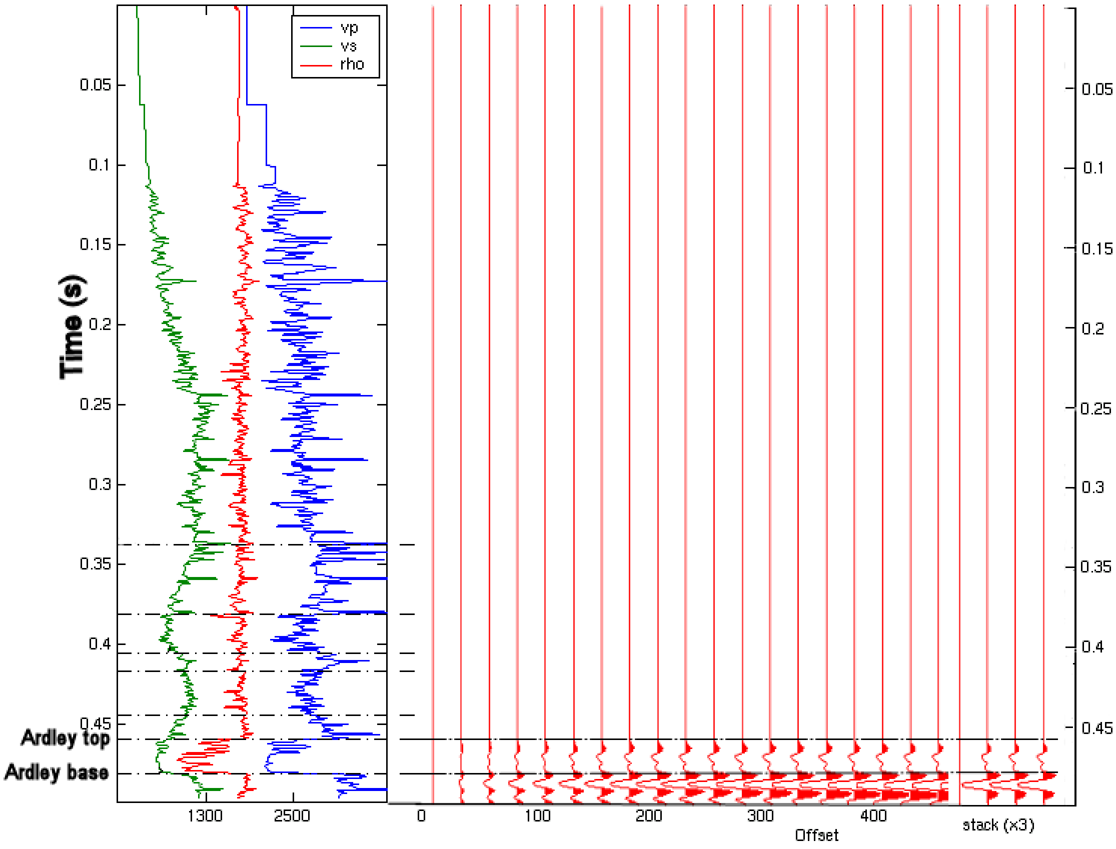

Figure 5.11 Difference between baseline and time-lapse P-S synthetic seismograms of Red Deer strata. Coal reflectivity has changed, and all events underlying the top of the coal are delayed in time.

5.4 Two-dimensional modelling

5.4.1 Ray-tracing

The two-dimensional model of the Cygnet strata built using GX2 modelling software was used for ray-tracing to simulate time-lapse imaging. Coal parameters were altered to simulate the effects of dewatering within 20 m of the wellbore (Figure 5.12), resulting in a P-wave velocity of 2205 m/s and a density of 1714 kg/m^3 in the coal zone. Shear wave velocities were not altered. Ray tracing was undertaken on this modified model, and a second iteration was also run to simulate a dewatered zone with a radius of 75 m from the well (Figure 5.13). Both P-P and P-S ray-tracing was completed for both models. Receivers were placed in the well at 15 m intervals from TD to surface. An illustration of selected P-P ray paths for the model with a 20 m dewatered zone is illustrated in Figure 5.14.

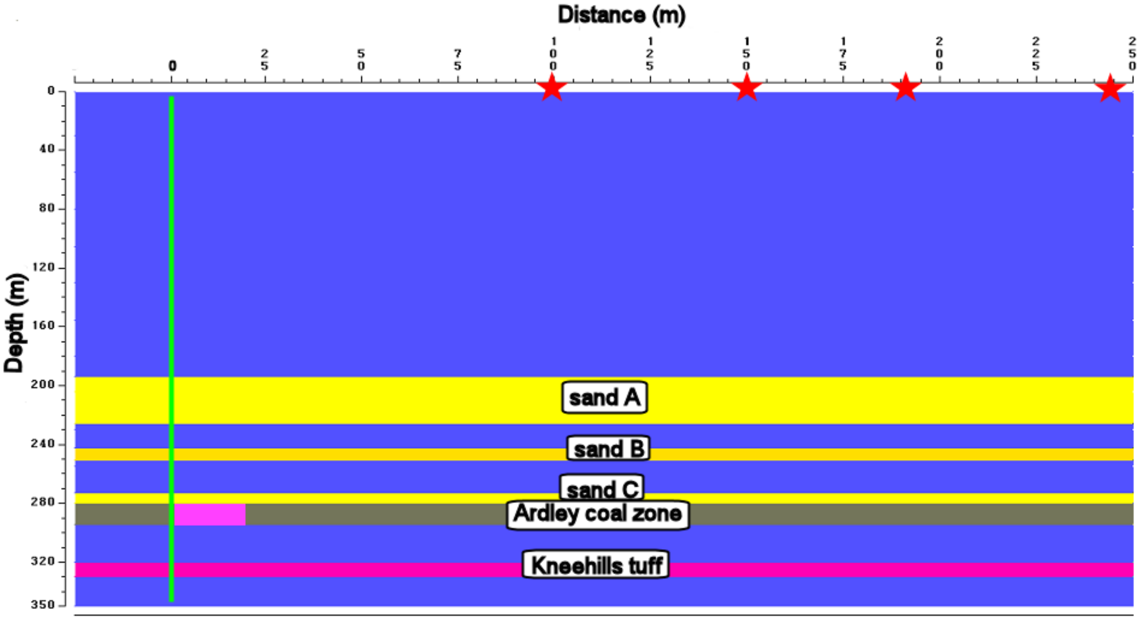

Figure 5.12 Illustration of perturbed GX2 numerical model used to simulate a dewatered Red Deer site. Sand layers are yellow, Ardley coal strata are grey, and the Kneehills tuff is pink; the purple area within the coal represents the dewatered zone. The 9-34 wellbore is indicated in green.

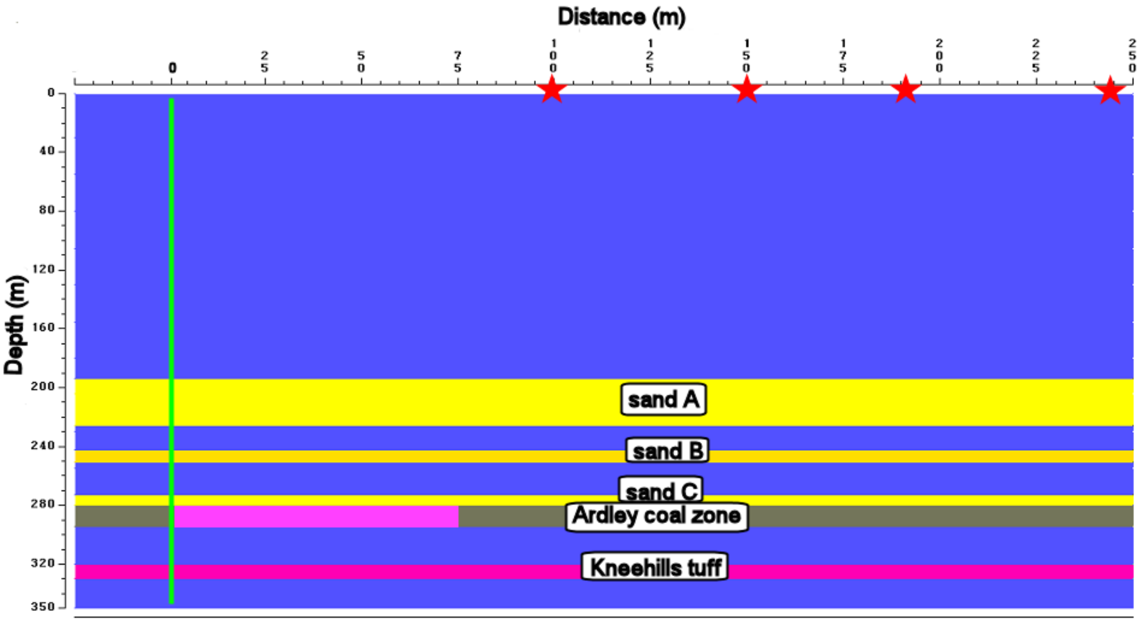

Figure 5.13 Illustration of perturbed GX2 numerical model used to simulate dewatering of a 75 m radius from the Red Deer borehole. The colour scheme is identical to that in Figure 5.12.

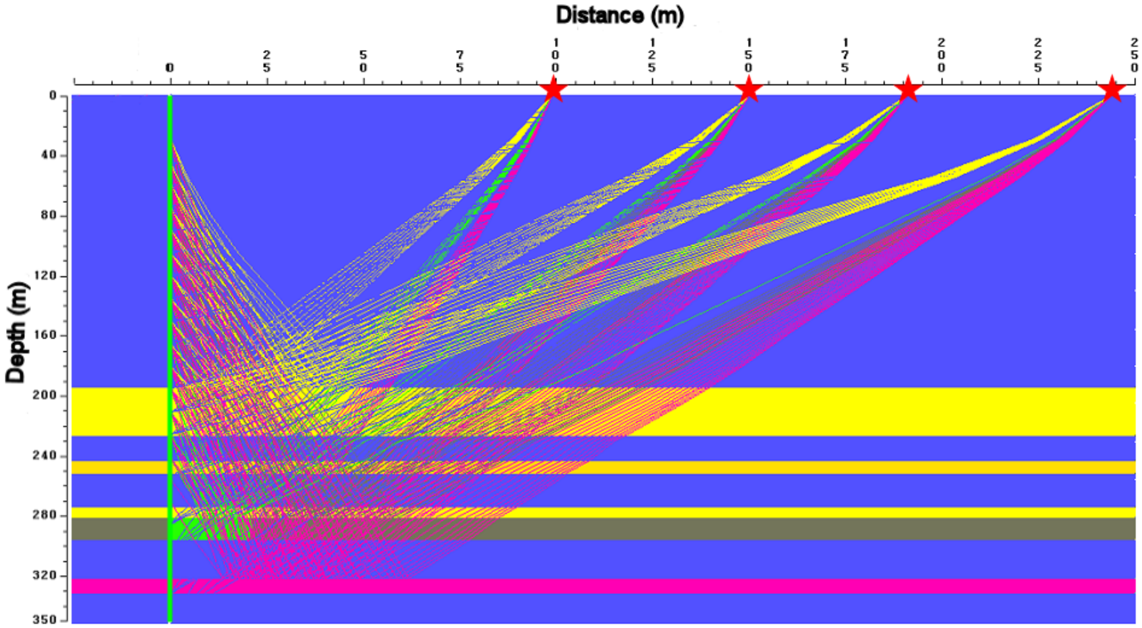

Figure 5.14 Ray paths resulting from P-P ray-tracing of GX2 numerical model with 20 m dewatered coal zone. Survey geometry is the same as that used for the Red Deer walkaway VSP surveys, with four offset shots and receivers spaced at 15 m throughout the wellbore. Ray paths illustrated here represent reflections from top of sand A, top of Ardley coal, and top of Kneehills tuff.

5.4.2 P-P modelling results

GX2 allows for individual model horizons to be turned on or off as reflectors when ray-tracing, and certain events to be selected for seismic trace generation. To simplify this modelling, four horizons were selected as active reflectors: the upper contact of sand A, the upper and lower contacts of the coal zone, and the upper contact of the Kneehills Tuff, which underlies the coal zone. A vertical impulse source was used for trace generation, and omni-phones were used for receivers, such that the total wavefield was modelled. Only the upgoing wavefield from each reflection was included in seismic trace generation, to avoid difficulties with wavefield separation. All traces (both P-P and P-S) were generated using convolution with an 80 Hz Ricker wavelet.

In the baseline P-P case, bothsSand A and the tuff yield resolvable reflections at each offset shot, as illustrated in Figure 5.15. The top of each horizon has negative reflectivity, resulting in a trough for both events. The responses of the upper and lower coal contacts interfere with each other to produce a strong amplitude trough-peak wavelet. This interference is similar to that seen in the detailed coal model of Chapter 4.

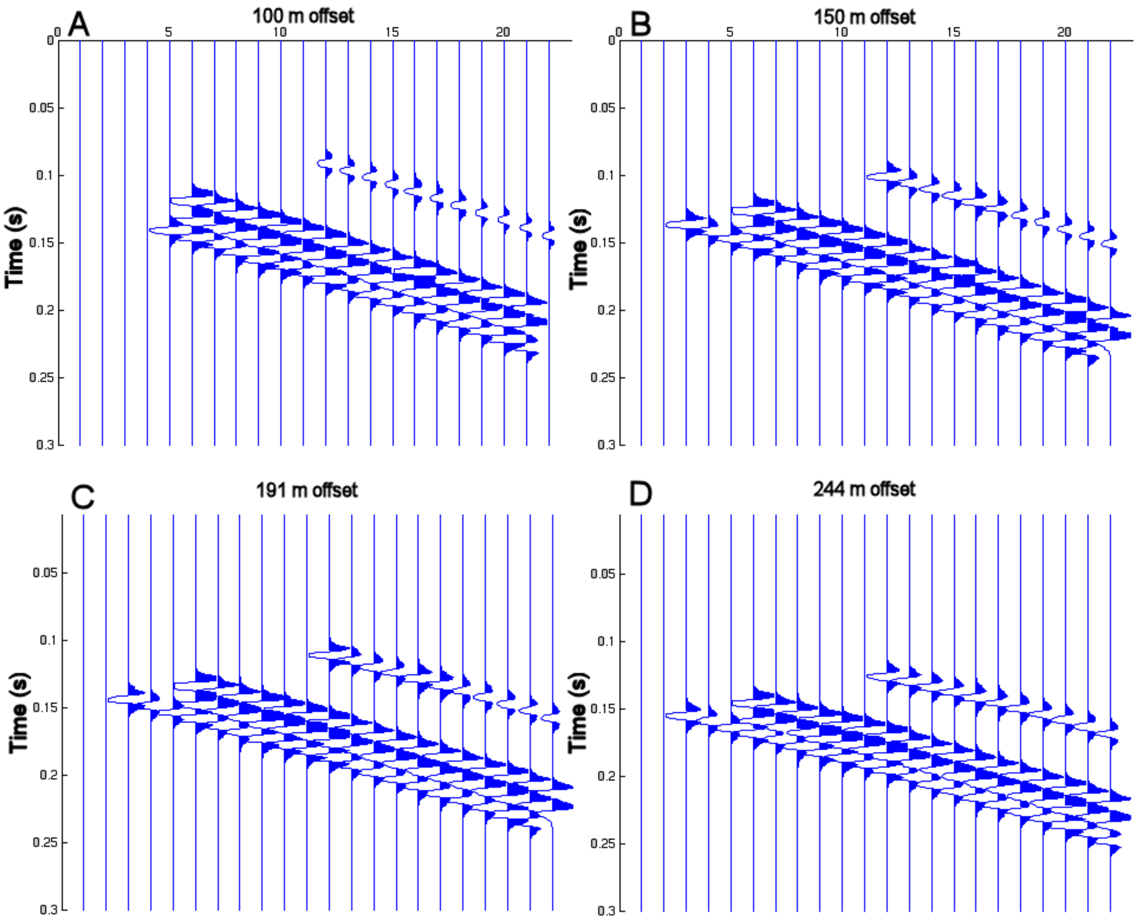

Figure 5.15 Upgoing PP wavefield shot records from each of 4 offsets in simulated GX2 walkaway VSP. Offsets are A) 100 m, B) 150 m, C) 191 m, D) 244 m. This layout of shots is used in all subsequent figures. Recorded events (from earliest to latest) represent top of sand A, Ardley coal top and base (wavelet interference is present), and top of Kneehills tuff. Receivers are spaced at 15 m intervals throughout the borehole, and ordered deepest to shallowest, left to right.

Ray-tracing of the model with the 20 m dewatered zone produces very similar shot records, showing events from each of the horizons. The ray-tracing algorithm occasionally has difficulty with the edge of the dry coal zone, resulting in a missed event, such as the tuff reflections on trace A-5, A-10 and A-11, as seen in Figure 5.16.

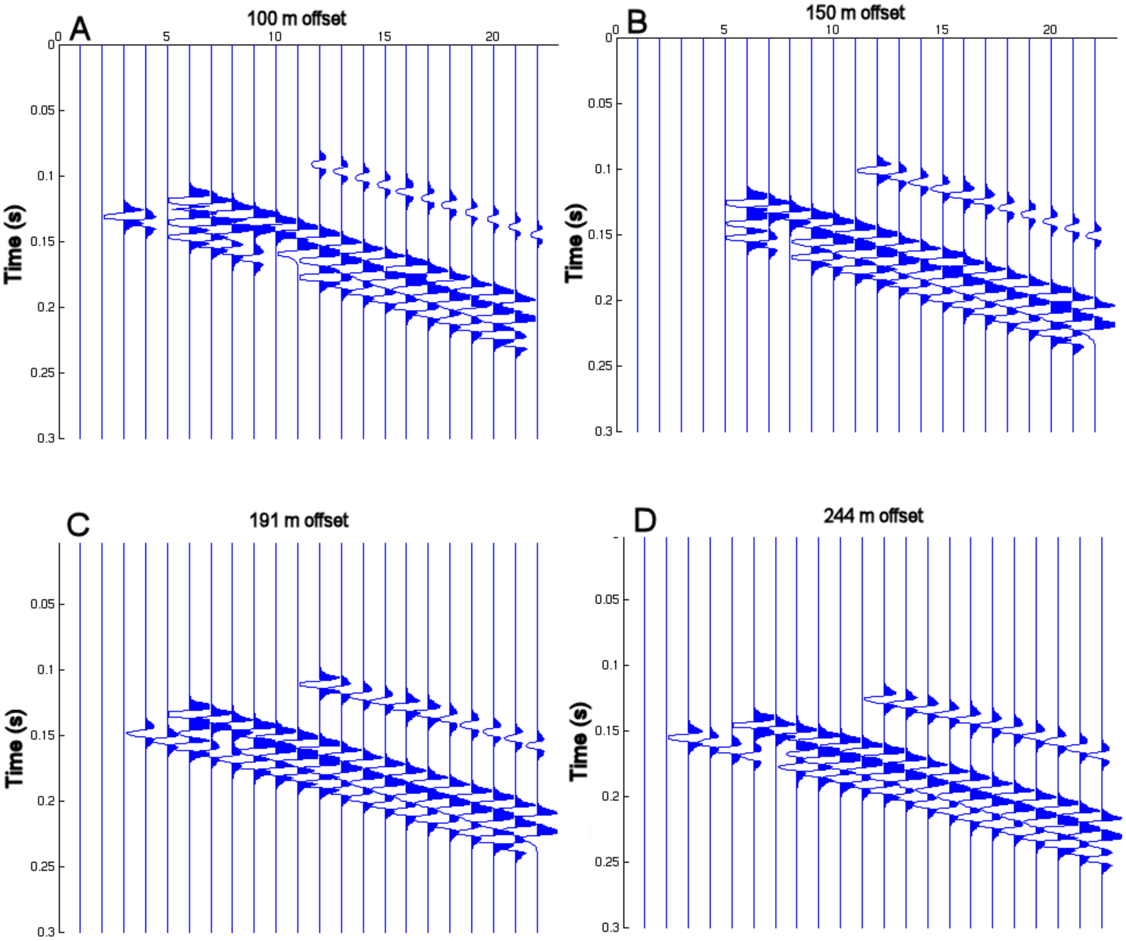

Figure 5.16 Upgoing PP wavefield shot records from each of 4 offsets in simulated GX2 walkaway VSP with 20 m dry coal zone. Amplitudes in this, and all subsequent figures, are scaled relative to the baseline PP amplitudes illustrated in Figure 5.15. In this case, each of the reflectors is captured, although occasionally an event is missed (such as A, trace 10, or D, trace 7) because of the interaction of the ray-tracer with the edge of the dry coal zone.

When calculating the difference between the baseline and dry responses, these missing events create a very large difference, so they were muted from the resultant difference data set, as they are artifacts, and not a representation of the true response of the strata.

After muting, the difference between the two surveys clearly shows residuals within the 20 m dewatered zone, and a velocity push-down effect in the tuff event below the affected area (Figure 5.17). The difference is most observable on the nearest offset shot, which is reasonable given that the dewatered zone has a radius of only 20 m.

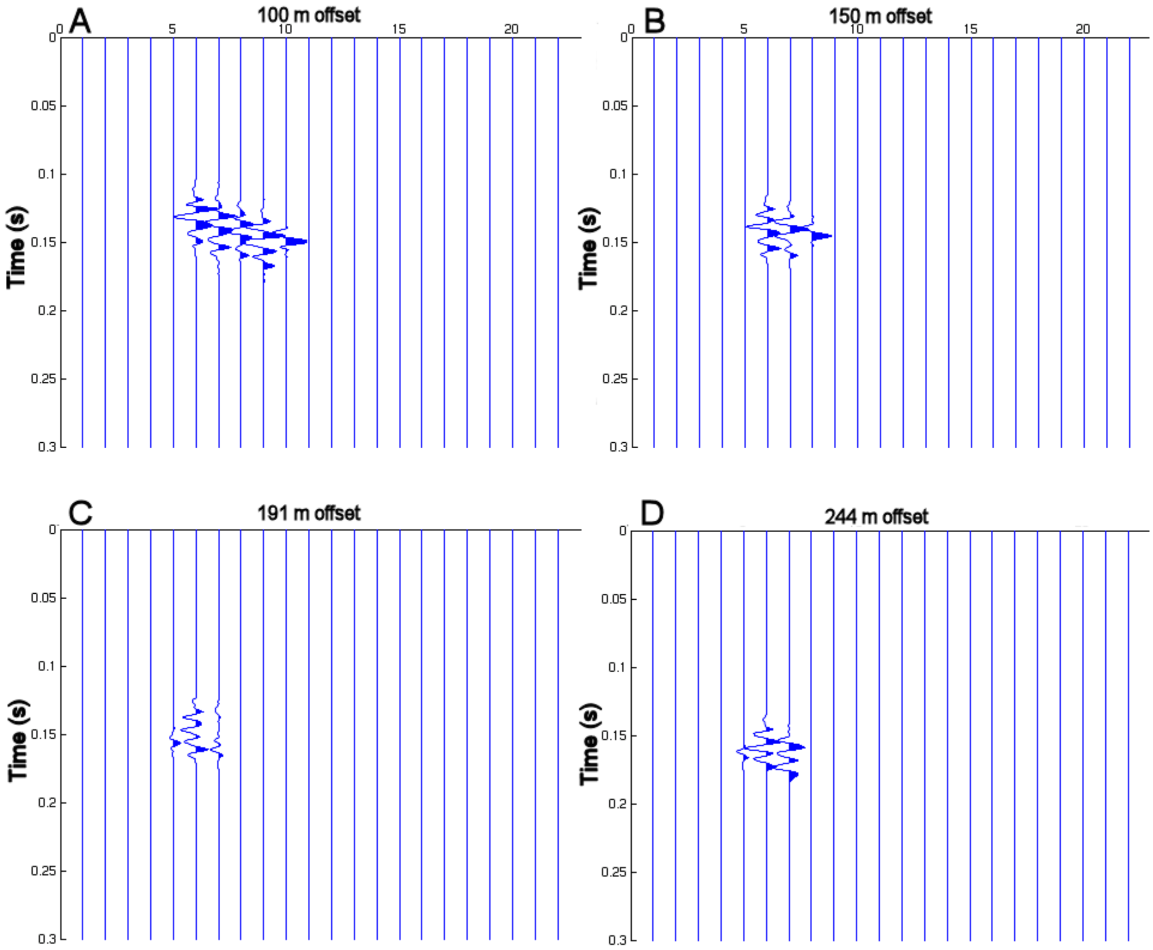

Figure 5.17 Difference between the seismic response of the baseline and 20 m dry models. Variations are noted in the reflectivity of the dewatered coal zone, and in the response of the tuff underlying this altered zone.

Ray-tracing of the numerical model with a 75 m dewatered zone again produced the occasional missed event, such as the tuff response in B-19 and B-20 (Figure 5.18). As in the baseline case, all reflectors have a clear response, and variations from the baseline survey are not immediately evident by inspection of the raw data.

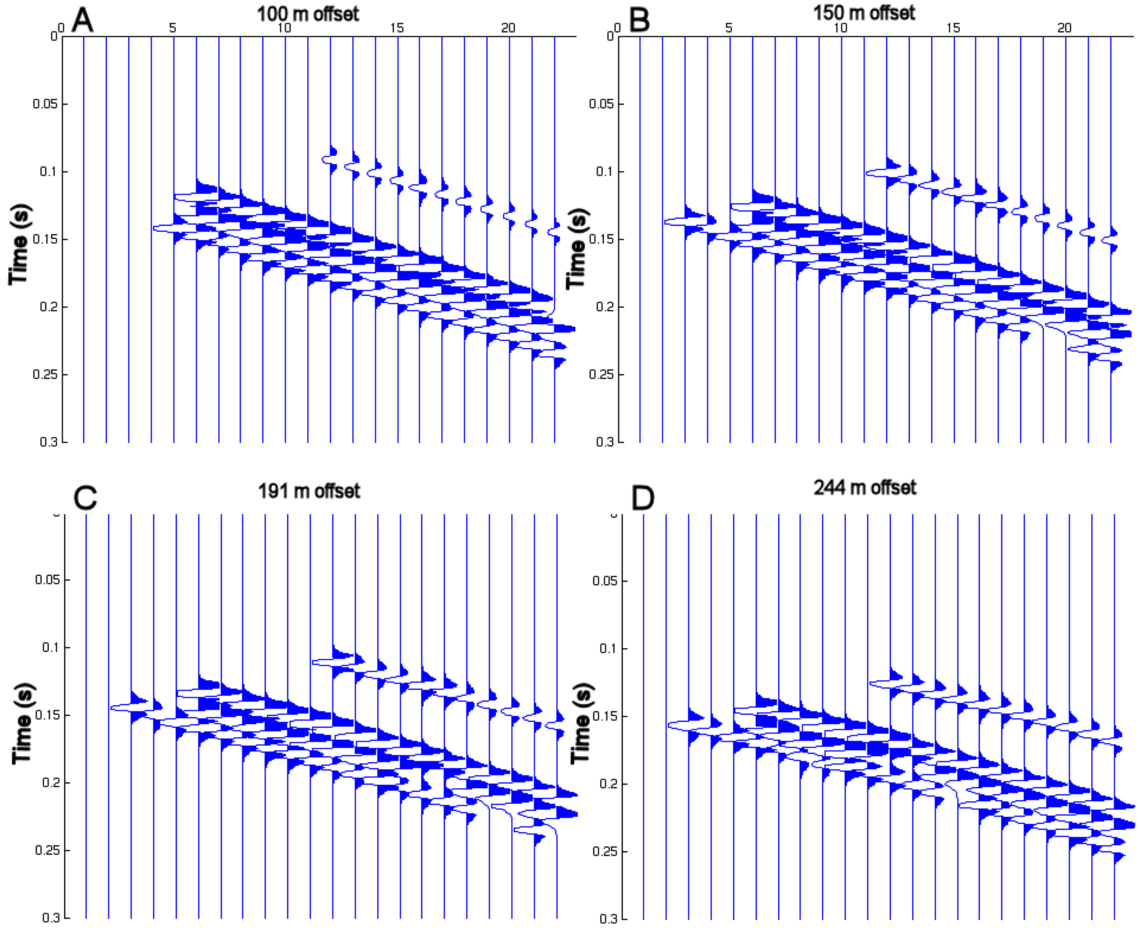

Figure 5.18 Upgoing PP wavefield response of GX2 model with 75 m dewatered coal zone. Events are occasionally missed because of problems with the edge of the dry coal, as in the 20 m dewatered case. Variations from the baseline survey are not discernable by inspection.

Time-lapse variations quickly become evident when the difference between the two sets of traces is taken (Figure 5.19). Reflectivity has changed within the dewatered coal zone, and velocity push-down effects are once again noted in the later events. Differences are noted over a greater depth range in the well because of the larger diameter of dewatered coals.

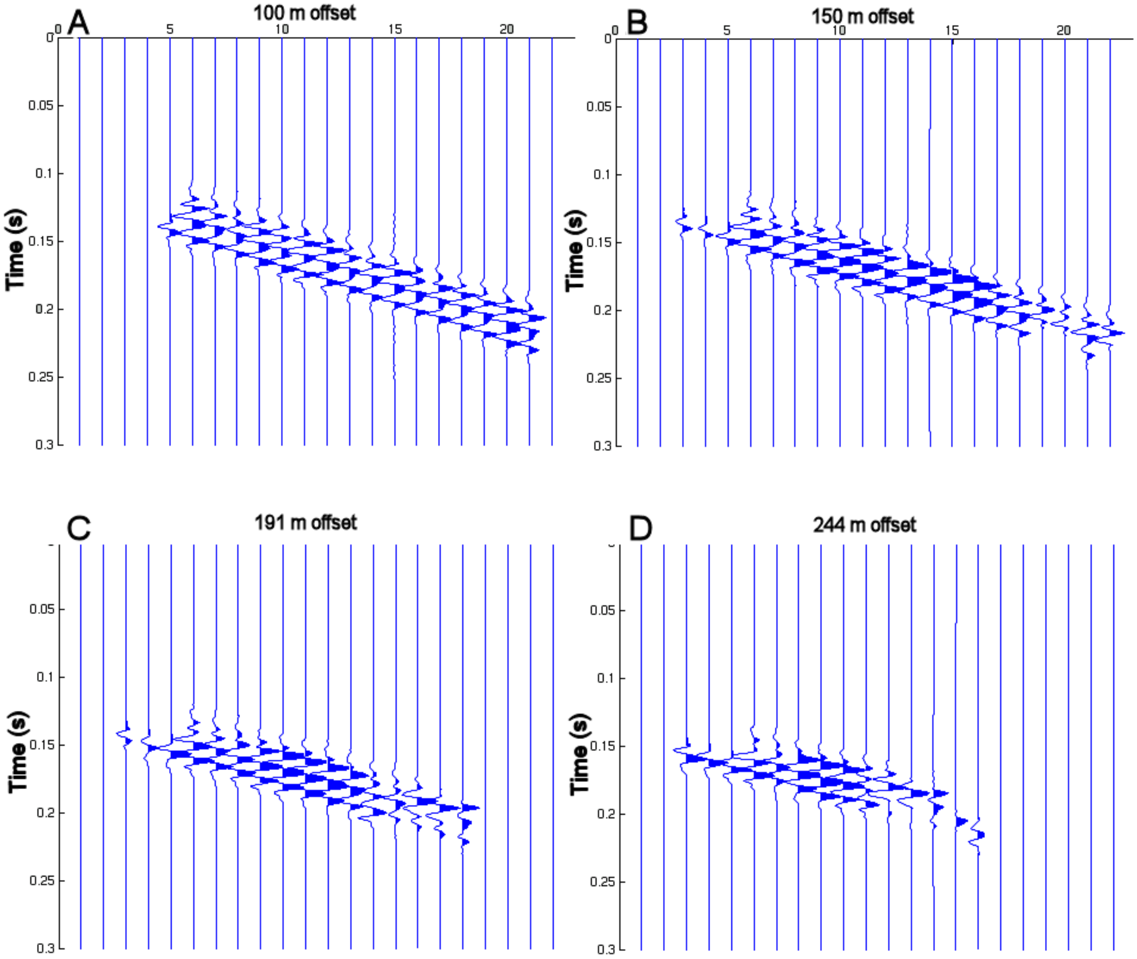

Figure 5.19 Difference between baseline PP seismic traces and time-lapse 75 m dewatered model. Reflectivity variations are noted throughout the dewatered coal zone, and time delays are evident in all events underlying the upper coal contact.

5.4.3 P-S modelling results

P-S synthetic seismograms of the Red Deer strata show a similar time-lapse effect to the P-P results. The baseline converted-wave 2-D survey is illustrated in Figure 5.20, showing resolvable events from each of the reflectors. An interesting feature is that the top of sand A shows a positive (peak) on converted-wave data, which is opposite polarity to its P-P response.

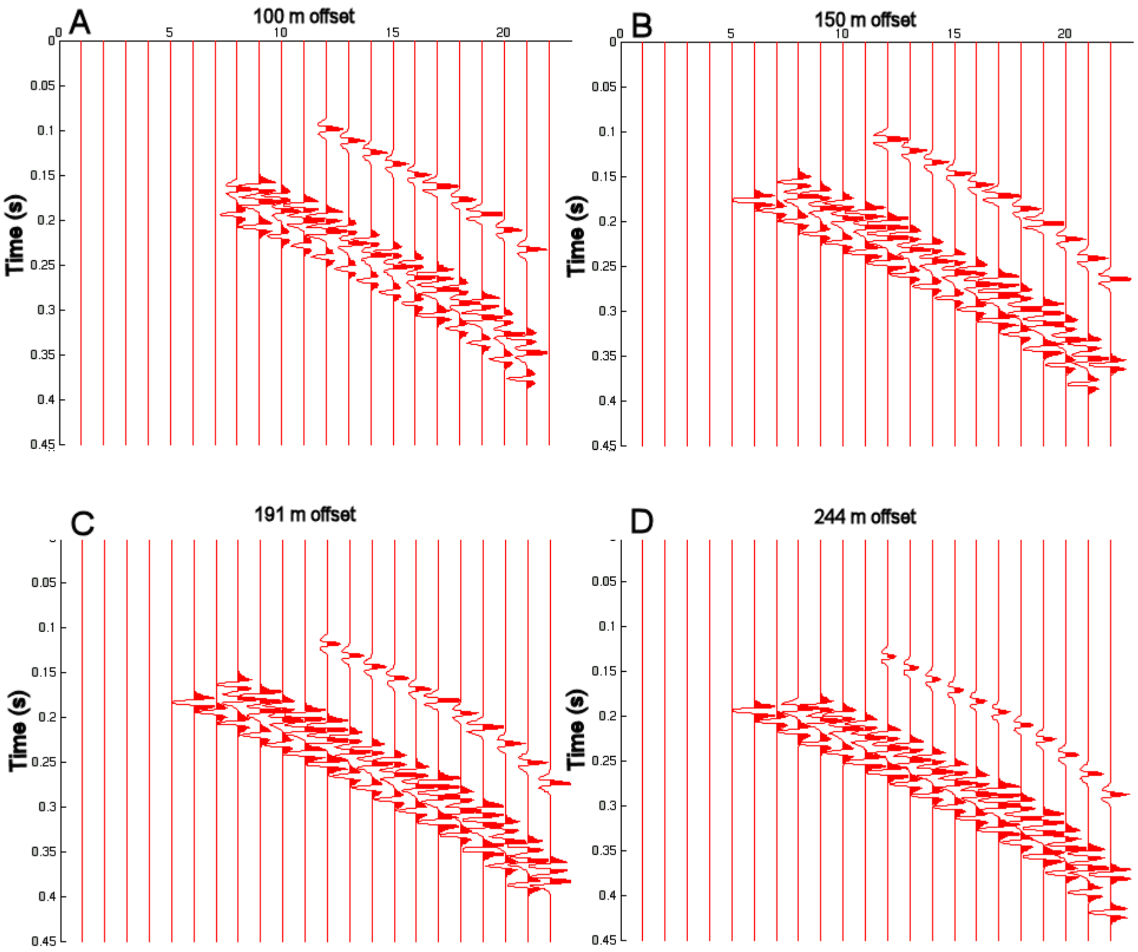

Figure 5.20 Upgoing P-S wavefield response of the baseline GX2 model. All reflectors have a clear response, although the polarity of the sand A response is opposite that of its P-P response.

This polarity reversal is an example that is consistent with the findings of Vant & Brown (2002), who noted that polarity reversals may be associated with geological situations where not all rock parameters change in the same direction, and where the changes in elastic parameters are relatively small. In this model, the top of sand A marks a small velocity increase in V_p, a relatively large increase in V_s (V_p=2825 m/s above, V_p=2872 m/s below; V_s=1200 m/s above, V_s=1500 m/s below), and a small density decrease (2395 kg/m^3 above, 2355 kg/m^3 below).

As in the compressional-wave case, the P-S ray tracer occasionally misses an event near the edge of the dewatered zone (Figure 5.21). Similarly to the P-P case, it is difficult to distinguish any variation in the coal response directly from the baseline to the time-lapse image.

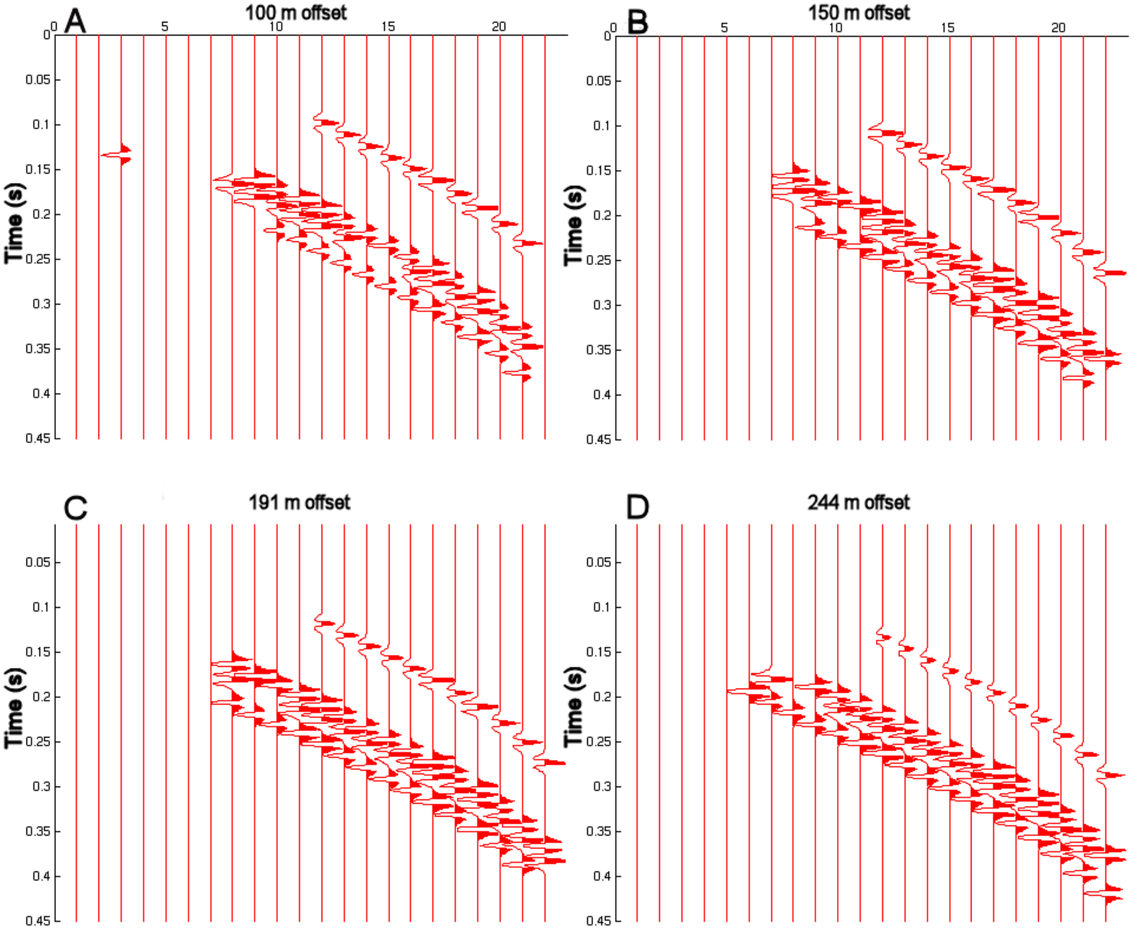

Figure 5.21 Upgoing P-S wavefield of the GX2 model with 20 m dry coal. Occasional events are missing as a result of ray-tracing difficulties with the edge of the dry coal, as seen in the P-P case.

When the difference is taken between the two sets of seismograms, the dry coal residuals are identifiable, and a velocity push-down effect is noted in the later events (Figure 5.22). The magnitude of the difference in the P-S case is less than the magnitude of the P-P difference, as seen by lower amplitudes in Figure 5.22 as compared to those in Figure 5.17.

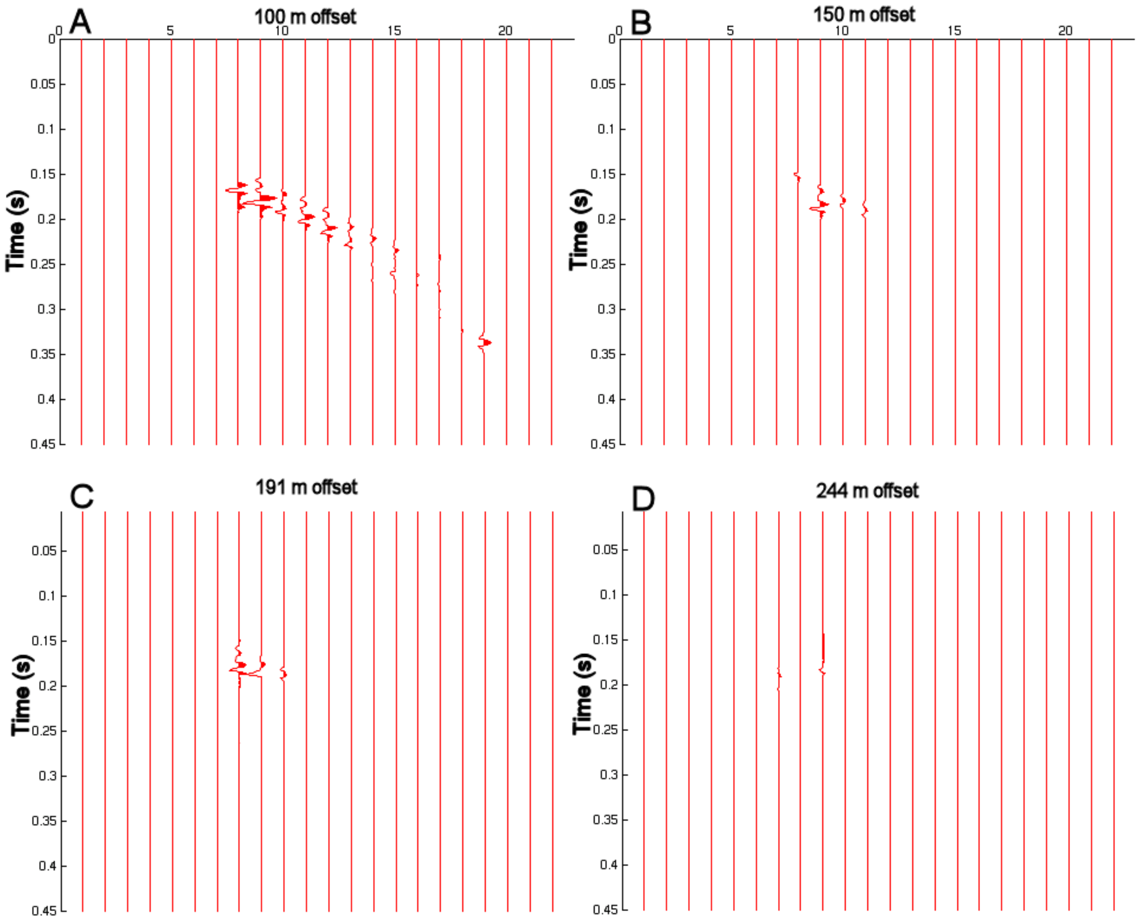

Figure 5.22 Difference between P-S seismic response of baseline model and 20 m dry coal model. The time-lapse effects in the P-S case are smaller than those noted in the P-P case.

Modelling of the 75 m radius dewatered zone shows similar effects to all previous models (Figure 5.23). Variations between the baseline and time-lapse seismograms are not immediately visible, however, the differences between the baseline and time-lapse models are more evident in this case than with the 20 m radius dewatered zone (Figure 5.24). This is because the P-S reflection points are close to the well due to the asymmetry of the P-S ray paths. Hence, differences are detected at all receivers within the well.

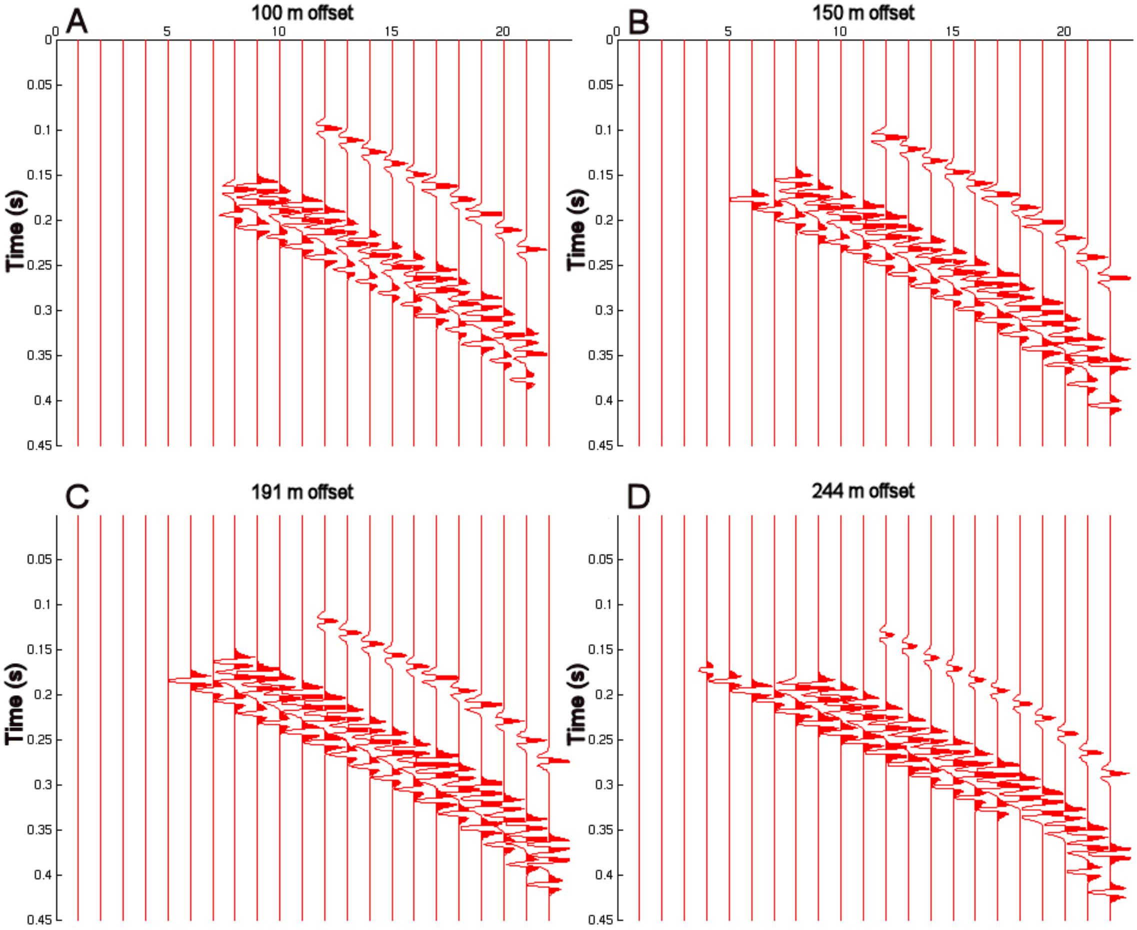

Figure 5.23 Upgoing P-S wavefield of the GX2 model with 75 m dry coal. Occasional reflections are missing as a result of ray-tracing difficulties with the edge of the dry coal, as seen in the P-P case.

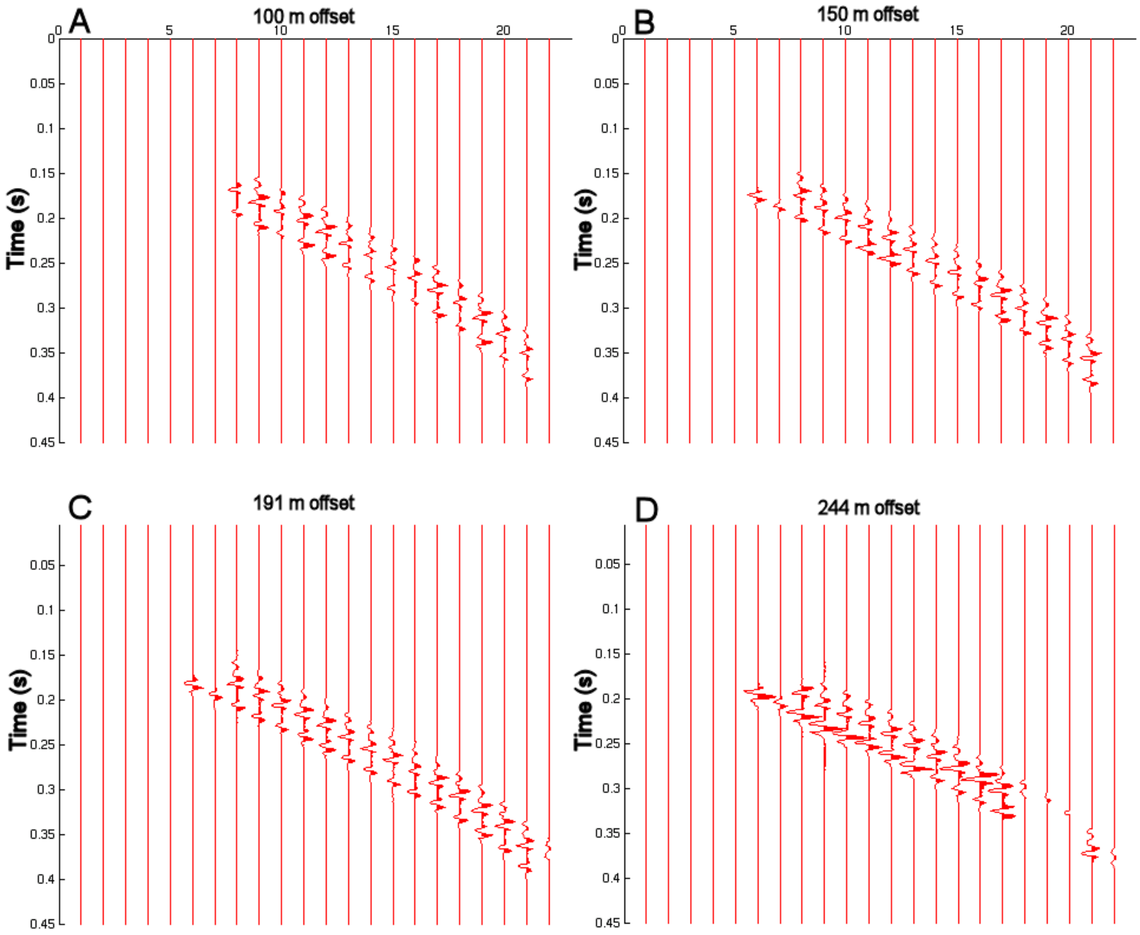

Figure 5.24 Difference between P-S seismic response of baseline model and 75 m dry coal model.

5.4 Discussion

This numerical modelling study has demonstrated that differences in coal reservoir properties resulting from dewatering may be imaged effectively using time-lapse seismic imaging. Both the 1.5-D synthetic seismograms and the multi-offset walkaway VSP ray-tracing have shown clear variations from baseline to time-lapse, thus predicting that the dewatered zone should be able to be distinguished from surrounding water-saturated coal. Time-lapse differencing is effective in imaging changes in reflectivity resulting from changes in density and velocity within the dewatered coal. Decreased velocity within the coal zone also results in a velocity push-down effect for deeper reflectors.

Identification of dewatered zones will enable CBM producers to optimally position development wells. That is, subsequent dewatering wells will not be placed within a swept zone, and subsequent injectors (in the case of ECBM) may be drilled into previously dewatered strata. Time-lapse monitoring of the dewatering process will lead to insight regarding reservoir permeability, as well. Heavily fractured and thus, more permeable, zones will lead to preferential dewatering along fracture trends. Delineation of these zones will allow efficient field development, and save drilling lower-flow producers in less permeable areas. Imaging of permeability trends will also potentially provide more accurate parameters to be used in reserve calculations.

Although changes in reservoir parameters resulting from carbon dioxide injection (and sequestration) in coal seams are not yet known, this modelling suggests that time-lapse seismic imaging will be an effective monitoring tool. It is likely that CO_2 (or N_2) injection will further affect the velocity and density of dewatered coal, potentially resulting in even greater reflectivity variations from the baseline. Gas injection may lead to coal swelling, and closure of cleats, resulting in changes in rigidity in addition to changes in dewatering trends. Thus the CO_2 front may be observable directly, and its effects on the dewatering process may be imaged, allowing inferences to be made regarding the gas plume. This will allow observers to ensure injected gas remains stored within the confines of the reservoir.

Chapter 6

Conclusions and Recommendations

6.1 Summary & Conclusions

The primary goals of this thesis were to examine the capabilities of multicomponent seismology for imaging coalbed methane strata, and to test the viability of seismic monitoring of coalbed methane production. Zero-offset vertical seismic profiles, walkaway VSPs, and surface seismic data collected at the Red Deer CBM test well were processed and examined to determine coal reflectivity. At this site, Ardley coals (Upper Cretaceous) are at a depth of 282 m below surface. Various sources were compared for their ability to image the Ardley coal zone effectively, resulting in a detailed study of the Vp/Vs character of shallow strata at this site. Seismic and well log data were used in numerical modelling to test the potential of time-lapse seismic imaging of coalbed methane production.

Examination of the seismic data leads to the following observations:

- Upper and lower coal contacts of the Ardley coal zone may be effectively imaged using either a conventional 44,000 lb. vertical vibrating source or a smaller vertical “mini-vibe”. The mini-P source produces the highest bandwidth data as a result of its ability to sweep at high frequencies. At this site, zero-offset mini-P VSP data contained useable frequencies of 8-220 Hz, whereas the big-P data contained bandwidth of 8-150 Hz. Although both images were of excellent resolution, the mini-P source was able to detect an intra-coal event in addition to the upper and lower contacts of the coal zone.

- A shear-wave source, an S-wave "mini-vibe" also produced excellent images of the upper and lower Ardley coal contacts at this site. The bandwidth of the shear-wave zero-offset VSP is 8-50 Hz at the base of the well, indicating relatively high attenuation of the 8-150 Hz sweep.
- Vp/Vs of the Red Deer strata are highest near the surface, generally decreasing with depth. Values nearest the surface are close to 5.0, decreasing to approximately 2.0 at 300 m depth. This profile correlates well with Vp/Vs profiles of shallow strata at other sites in Alberta and the world.
- Good correlations were found between Vp/Vs values calculated using the zero-offset VSP data and those calculated using cased-hole sonic and shear sonic well logs. This suggests that both data sets will be equally appropriate for modelling. Velocity dispersion of approximately 2.3% is noted for P-waves, whereas shear-wave velocity dispersion is approximately 6.8%. Stewart's 1984 equation was used to determine Q_p and Q_s for the strata, which are estimated to be 31.4 and 9.7, respectively.
- Both compressional and converted-wave walkaway VSP surveys are effective in imaging the Ardley coal zone. At near to mid-range offsets, the P-S data produces higher-resolution images, allowing the identification of intra-coal events not visible on the P-P data. At farther offsets, the P-S image quality degrades due to NMO stretch, and the P-P data set produces better images of the coal zone contacts.
- Surface seismic data recorded using the mini-P source produced an identifiable reflection of the coal zone, suggesting that it is an optimal source for surface seismic data as well as vertical seismic profiles. A full-fold 3D survey is expected to successfully map lateral facies and thickness changes of the coal zone across the survey area.

- Determination of Vp and Vs from the VSP data and density values from well logs yields reflectivities, calculated from numerical modelling, that closely match the Red Deer data set.
- Tuning plays a significant role in the P-P reflectivity of Red Deer strata, increasing reflection amplitudes to as much as 300% of the value predicted by Zoeppritz equations for the top of coal event. Wavelet interference is much less evident in the P-S reflectivity of the coal zone, yielding better resolved images in P-S data when compared to P-P data.
- P-P amplitude variations with offset are minimal in reflections from these strata, until angles of incidence exceed 50 degrees. Changes in amplitude observed in stacked coal seismic data will therefore most likely be the result of lateral variations in coal properties.
- Converted-wave AVO effects are greater than those noted in the P-P case. The maximum amplitude P-S reflection occurs at an incidence angle of approximately 48 degrees.
- Numerical modelling study has provided "proof of concept" that differences in coal reservoir properties resulting from dewatering may be effectively imaged using time-lapse seismic imaging. Coal dewatering results in increased reflectivity within the coal zone, and a velocity "push-down" effect in all reflectors underlying the coal top.
- Identification of dewatered zones on time-lapse sections will be easiest using P-P data, as P-S data shows less variation in reflectivity between wet and dry coal. If sections are being differenced, however, dewatered zones will be distinguished by both compressional and converted-wave surveys.

6.2 Recommendations

This study has demonstrated that seismic methods should prove to be of great value in development of coalbed methane resources in Alberta.

The following recommendations are made to CBM producers:

- High-bandwidth seismic data are critical to imaging any intra-coal events within the coal zone. A truck-mounted mini-P vertical vibrating source may be the optimal choice because of its higher sweep capacity, depending on the depth of the coals being imaged.
- Tuning effects will greatly affect the P-P reflectivity of the coal zone, and thus, the reflectivity will give some indication of the lateral continuity and thickness of the coal.
- Time-lapse seismic imaging should prove effective in identifying dewatered coal zones, allowing optimal positioning of development wells. Time-lapse techniques will likely provide some ability to identify injected gas as well, either by direct imaging of the plume or by its effects on the dewatered zone, such as swelling of the matrix.

Because coalbed methane is still in the early stages of development in Alberta, producers can take advantage of seismic techniques early in reservoir life, thus ensuring optimal development of their property, and maximizing the value of their asset. This is of particular value in areas where ECBM will be used as a greenhouse gas mitigation strategy as well, allowing field optimization to be combined with an effective monitoring technique, ensuring proper sequestration of the injected gas without adversely affecting methane production.

References

Alberta Energy and Utilities Board, 2002. Alberta's reserves 2001 and supply/demand outlook 2002-2011: crude bitumen, crude oil, natural gas and liquids, coal, sulphur: Alberta Energy and Utilities Board statistical series 2002-98.

Arts, R., Eiken, O., Chadwick, A., Zweigel, P., van der Meer, L., and Zinszner, B., 2002. Monitoring of CO_2 injected at Sleipner using time lapse seismic data: Proceedings of 6th Annual Greenhouse Gas Technology conference, Japan, April, 2002.

Avery, B., 2001. Project will test methane extraction: Edmonton Journal, August 5, 2001.

Avery, B., 2002. Canadian coal bed methane sold for first time: Edmonton Journal, February 28, 2002.

Bachu, Stefan, 2000. Sequestration of CO_2 in geological media: criteria and approach for site selection in response to climate change: Energy Conservation and Management, **41**, 953-970.

Bates, Robert L., and Jackson, Julia A., eds., 1984. Dictionary of Geological Terms, third edition. American Geological Institute, Anchor Books, 571 pp.

Beaton, A., 2003. Production potential of coalbed methane resources in Alberta: Energy & Utilities Board/Alberta Geological Survey Earth Sciences Report 2003-03, 68 pp.

Canadian Association of Petroleum Producers, 2003. Responsible coalbed methane development in Canada. Internal publication, www.capp.ca, March, 2003.

Chadwick, A., Holloway, S., Riley, N., 2000. Deep CO_2 sequestration offshore provable greenhouse strategy: Offshore, November 2000, 134-135.

Cieslewicz, Dan, 1999. Near-surface seismic characterization using three-component buried geophones. Master's Thesis, University of Calgary, 101 pp.

Davis, Thomas L., Terrell, Martin J., Benson, Robert D., Cardona, Reynaldo, Kendall, Robert R., and Winarsky, Robert, 2003. Multicomponent seismic characterization and monitoring of the CO_2 flood at Weyburn Field, Saskatchewan: The Leading Edge, **22**, 696-697.

Dawson, F.M., Marchioni, D.L., Anderson, T.C., and McDougall, W.J., 2000. An assessment of coalbed methane exploration projects in Canada: GSC Bulletin **549**, 218 pp.

Deffenbaugh, M., Shatilo, A., Schneider, B., and Zhang, M., 2000. Resolution of converted waves in attenuating media: Expanded Abstract, 70th Annual International Meeting, Society of Exploration Geophysicists, 1178-1180.

Eiken, O., Brevik, I., 2000. Seismic monitoring of CO_2 injected into a marine aquifer: Expanded Abstract, 70th Annual International Meeting, Society of Exploration Geophysicists, 1623-1626.

Fay, Albert H., 1920. A Glossary of the Mining and Mineral Industry. U.S. Bureau of Mines Bulletin, **95**, Washington, D.C.: Government Printing Office.

Fokker, P.A., and van der Meer, L.G.H., 2002. The injectivity of coalbed CO_2 injection wells: Proceedings of 6th annual Greenhouse Gas Technology conference, Japan.

Gas Technology Institute, 2001. North American Coalbed Methane Resource Map, Map #GTI 01/0165

Gochioco, L.M., 1991. Tuning effect and interference reflections from thin beds and coal seams: Geophysics, **56**, 1288-1295.

Gochioco, L.M., 1991. Advances in seismic reflection profiling for U.S. coal exploration: The Leading Edge, **10**, 24-29.

Gochioco, L.M, 1992. Modelling studies of interference reflections in thin-layered media bounded by coal seams: Geophysics, **57**, 1209-1216.

Gochioco, L.M., 2000. High-resolution 3-D seismic survey over a coal mine reserve area in the U.S. – A case study: Geophysics, **65**, 712-718.

Gochioco, L.M., and Cotton, S.A., 1989. Locating faults in underground coal mines using high-resolution seismic reflection techniques: Geophysics, **54**, 1521-1527.

Greaves, R.J., 1984. Coal prospect evaluation using high-resolution reflection seismology – a case study: The Leading Edge, **3**, 44-47.

Gunter, W.D., Gentzis, T., Rottenfusser, B.A., Richardson, R.J.H., 1997. Deep coalbed methane in Alberta, Canada: a fuel resource with the potential of zero greenhouse gas emissions: Energy Conversion and Management, **38**, 217-222.

Hamilton, Edwin L., 1976. Shear-wave velocity vs. depth in marine sediments: a review: Geophysics, **41**, 985-996.

Hamilton, Edwin L., 1979. Vp/Vs and Poisson's ratio in marine sediments and rocks: Journal of the Acoustical Society of America, **66** (4), 1093-1101.

Henson, Jr, H., and Sexton, J.L., 1991. Premine study of shallow coal seams using high-resolution seismic reflection methods: Geophysics, **56**, 1494-1503.

Hitchon, B., Gunter, W.D., Gentzis, T., and Bailey, R.T., 1999. Sedimentary basins and greenhouse gases: a serendipitous association: Energy Conversion and Management, **40**, 825-843.

Hoffe, Brian H., and Lines, Laurence R., 1999. Depth imaging by elastic wavefields – where P meets S: The Leading Edge, **18** (3), 370-373.

Hughes, J.D., Dawson, F.M., Duggan, J., Hallas, D.F., Khitrova, G., Marchioni, D.L., Richardson, R., Wynne, D., 1999. Regional analysis of the Ardley coal zone, Alberta, Canada, for coalbed methane production and CO_2 sequestration: GSC Open File **3761**, 116 pp.

Jaramillo Sarasty, Jessica, and Stewart, Robert R., 2002. Well log analysis of elastic properties from the White Rose oilfield, offshore Newfoundland: CREWES Research Report, **14**, 2.1-2.21.

Knapp, R.W., 1990. Vertical resolution of thick beds, thin beds, and thin-bed cyclothems: Geophysics, **55**, 1183-1190.

Langenberg, W., 1990. Coal geology and its application to coal-bed methane reservoirs: lecture notes for short course, Edmonton, August 20-24, 1990.

Lawton, D.C., 1985. Seismic facies analysis of delta-plain coals from Camrose, Alberta, and lacustrine coals from Pictou Coalfield, Nova Scotia: American Association of Petroleum Geologists Bulletin, **69**, 2120-2129.

Lawton, Don C., 1990. A 9-component refraction seismic experiment: Canadian Journal of Exploration Geophysics, **26**, 7-16.

Li, Guoping, 2003. 4D seismic monitoring of CO_2 flood in a thin fractured carbonate reservoir: The Leading Edge, **22**, 690-695.

Lyatsky, H.V., and Lawton, D.C., 1988. Application of the surface reflection seismic method to shallow coal exploration in the plains of Alberta: Canadian Journal of Exploration Geophysics, **24**, 124-140.

Lyons, W.S., 2001. Seismic maps Ferron coalbed sweetspots: American Association of Petroleum Geologists Explorer, December 2001, 32-37.

Metcalfe, R.S., Yee, D., Seidle, J.P., and Puri, R., 1991. Review of research efforts in coalbed methane recovery: SPE Paper 23025, presented at the Asia-Pacific conference, Perth, Australia, November 4-7.

Myer, Larry R., Hoversten, Michael, and Gasperikova, Erika, 2002. Sensitivity and cost of monitoring geologic sequestration using geophysics: Proceedings of 6th annual Greenhouse Gas Technology conference, Japan, April 2002.

Natural Resources Canada, 2002. Canadian Atlas online. http://atlas.gc.ca

Nikols, D., Treasure, S., Stuhek, S., and Goulet, D., 1990. Coalbed methane in Alberta – What's it all about? Alberta Geological Survey, Information series **108**.

Osborne, Carla A., and Stewart, Robert R., 2001. Analysing the Pikes Peak multi-offset VSP data: CREWES Research Report, **13**, 48.1-48.14.

Ramos, A.C.B., and Davis, T.L., 1997. 3-D AVO analysis and modelling applied to fracture detection in coalbed methane reservoirs: Geophysics, **62**, 1683-1695.

Reeves, Scott, 2002. Coal-Seq project update: field studies of ECBM recovery/CO_2 sequestration in coalseams: Proceedings of 6th annual Greenhouse Gas Technology conference, Japan, April 2002.

Rice, D.D., 1993. Composition and origins of coalbed gas. In: Hydrocarbons from Coal: B.E. Law and D.D. Rice (eds.), American Association of Petroleum Geologists Studies in Geology, **38**, 159-184.

Richardson, S.E., Meyer, R., Lawton, D.C., and Langenberg, W., 2001. Seismic modelling of coalbed methane strata, Willow Creek, Alberta: CREWES Research Report, **13**, 11.1-11.29

Richardson, Sarah E., and Lawton, Don C., 2002. Time-lapse seismic imaging of enhanced coalbed methane production: a numerical modeling study: CREWES Research Report, **14**, 17.1-17.13.

Saulsberry, J., Schafer, P., Schraufnagel, R., eds., 1996. <u>A guide to coalbed methane reservoir engineering.</u> Chicago, Gas Research Institute, variously paginated.

Seidle, J.P., Sigdestad, C.A., Raterman, K.T., and Negahban, S., 1997. Characterization of enhanced coalbed methane recovery injection wells: SPE Paper 38861, presented at Annual Technical conference and exhibition, San Antonio, October 5-8.

Sheriff, Robert E., 2002. <u>Encyclopedic dictionary of applied geophysics, fourth edition</u>. Society of Exploration Geophysicists, Geophysical References **13**, 429 pp.

Shuck, E.L., David, T.L., and Benson, R.D., 1996. Multicomponent 3-D characterization of a coalbed methane reservoir: Geophysics, **61**, 315-330.

Smith, D.G., 1994. Uppermost Cretaceous and Tertiary strata. In: Geological Atlas of the Western Canadian Sedimentary Basin, G.D. Mossop and I. Shetsen (eds.), Canadian Society of Petroleum Geologists and Alberta Research Council, 510 pp.

Stewart, Robert R., Huddleston, Phil D., and Kan, Tze Kong, 1984. Seismic versus sonic velocities: a vertical seismic profiling study: Geophysics, **49**, 1153-1168.

Sun, Zandon, 1999. Seismic methods for heavy oil reservoir monitoring and characterization. Master's thesis, University of Calgary, 292 pp.

Thigpen, Ben B., Dalby, A.E., and Landrum, Ralph, 1975. Report on subcommittee on polarity standards: Geophysics **40**, 694-699.

Toksöz, M. Nafi, and Stewart, Robert R., eds., 1984. Vertical seismic profiling, Part B: Advanced concepts. Handbook of Geophysical Exploration, Geophysical Press. 419 pp.

van der Meer, L.G.H., 2002. CO_2 storage in the subsurface: Proceedings from the 6th annual Greenhouse Gas Technology conference, Japan.

Vant, Alexandru, and Brown, R. James, 2002. Effects of density and velocity changes on the correlation of P-P and P-S reflection events: CREWES Research Report, **14**, 4.1-4.19.

Wang, Zhijing, Cates, Michael E., and Langan, Robert T., 1998. Seismic monitoring of a CO_2 flood in a carbonate reservoir: a rock physics study. Geophysics, **63**, 1604-1617.

Wang, Zhijing, and Nur, Amos M., 1989. Effects of CO_2 flooding on wave velocities in rocks with hydrocarbons: SPE Paper 17345, SPE Reservoir Engineering, November 1989, 429-436.

Wawerski, W.R., and Rudnicki, J.W., (eds.), 1998. Terrestrial sequestration of CO_2 – An assessment of research needs: Workshop Proceedings, Office of Basic Energy Sciences, United States Department of Energy, 67 pp.

Widess, M.B., 1973. How thin is a thin bed? Geophysics, **38**, 1176-1180.

Xue, Ziqiu, Ohsumi, Takashi, and Koide, Hitoshi, 2002. Laboratory measurements of seismic wave velocity by CO_2 injection in two porous sandstones: Proceedings of 6th annual Greenhouse Gas Technology conference, Japan, April 2002.

Ziolkowski, Anton, 1982. Seismic vital in coal-mining: The Leading Edge, **1**, 33-35.